UNIVERSITAT DE BARCELONA

Instabilities in Newtonian and non-Newtonian fluids

Mireia Torralba Cuello

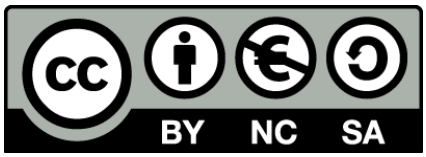

UNIVERSITAT DE BARCELONA

Departament d'Estructura i Constituents de la Matèria

Instabilities in Newtonian and non-Newtonian fluids

Mireia Torralba Cuello

Ph.D. Thesis

Barcelona, February 2007

Universitat de Barcelona
Departament d'Estructura i Constituents de la Matèria
Programa de doctorat Física Avançada
Bienni 2001/03

Instabilities in Newtonian and non-Newtonian fluids

Memòria de la tesi presentada el febrer de 2007 per
Mireia Torralba Cuello
per optar al títol de Doctor en Física
dirigida pel Dr. Jordi Ortín Rull

Al Lluis, i als meus pares

Agraïments

Voldria començar agraïnt la confiança que el meu director de tesi, el Dr. Jordi Ortín va dipositar en mi, així com l'esforç que ha posat en el desenvolupament de la meva tesi. Al llarg d'aquests anys he pogut beneficiar-me dels seus amplis coneixements de Física i de la seva destresa en el camp experimental. Gràcies a ell he aprés els fonaments del treball experimental i, sobretot durant l'escriptura de la tesi, he aprés les bases de la redacció del treball científic.

També m'agradaria agraïr a la Dra. Eugenia Corvera Poiré pel suport donat en el treball dels dits de Saffman–Taylor pertorbats. La seva col·laboració en el desenvolupament dels experiments va començar els primers anys de la tesi i en els darrers anys es va intensificar enormement.

Agraeixo també el suport de la Dra. Aurora Hernàndez–Machado en el desenvolupament dels experiments de Saffman–Taylor.

La col·laboració amb el Dr. Jesús Antonio del Río en els experiments del fluxe oscil·lant d'un fluid viscoelàstic va ser molt profitosa i agradable. En aquests experiments també haig d'agraïr la col·laboració de la Dra. Guadalupe Huelsz.

Les converses amb els Doctors Wim Van Saarlos, Ellaq Somfai i, en especial, Alexander Morozov van ser de molta ajuda en la caracterització i estudi de la inestabilitat en el fluxe viscoelàstic. No puc oblidar que el contacte amb el grup del Dr. Van Saarlos va ser possible gràcies a la participació en la xarxa europea PHYNECS gestionada pel Dr. Jaume Casademunt.

El temps que vaig passar fent experiments al laboratori de fluids i inestabilitats interficials vaig tenir la sort de compartir-lo amb uns grans companys i amics com el Jordi Soriano, que em va brindar un suport inestimable en els primers anys que vaig passar al laboratori. Tampoc puc oblidar les discussions amb l'Enric Álvarez i el Rodrigo Ledesma de les que vaig treure tantes noves idees, vaig aprendre tant i que em van fer plantejar noves preguntes. També haig d'agrair el suport tècnic de l'Albert Comerma durant tot aquest temps. Per acabar també vull agraïr a un altre bon amic, el darrer arribat al laboratori, el Ramon Planet, per haver estat tan bon

company de laboratori. I, encara que durés poc, també guardo un molt bon record de l'época en que el Josep Maria Huguet va treballar al laboratori.

Els experiments que vaig fer a Mèxic vaig tenir la sort de fer-los en companyia de dos excel·lents companys, els germans Alfonso i Rafael Castrejón–Pita. A l'Alfonso en particular li dec molt del que he aprés de PIV.

També guardaré un record molt especial dels dos companys amb qui vaig començar l'etapa del doctorat, el Xavier Illa i la Maria Mañosas, de qui també guardaré un gran record com a companya de pis. No vull oblidar-me del Javi, l'Albert, la Marta que, junt amb d'altres, han fet que l'hora de dinar fos un parèntesi molt agradable al llarg de molt de temps. També vull esmentar el Fèlix, l'Ivan, el Marc o l'Isaac amb qui també he compartit bons moments.

Al Manel Quevedo en especial i a la resta de membres del taller mecànic els vull agraïr el suport tècnic brindat al llarg de tota la tesi.

Encara que estic segura que quan d'aquí un mes rellegeixi els agraïments me n'adonaré que m'he deixat a molta gent molt important per mi, vull fer un agraïment col·lectiu als companys de carrera i amics que van fer que els anys de llicenciatura fossin realment memorables: l'Aleix, la Pilar, la senyora Wilson, la Isa, la Marta Martínez, el Miquel, l'Ariadna, el Pide, l'Ivan, la Judith, el Ferran, el Ruben, el Carles, el Sergi, el Pep, el Busy, l'Ester i tots els que m'estic deixant...

Vull dedicar també un record molt especial per als meus amics de Sabadell, que han estat al meu costat des de fa tants anys que no tinc record de l'època en que no els coneixia.

Els meus pares i la meva germana sempre m'han recolzat en l'elecció de fer un doctorat en Física. Al meu pare en particular haig d'agraïr-li que em contagiés la seva preferència per les assignatures científiques, que de moment m'ha portat fins aquí. I a tots tres els vull agraïr el suport i l'amor que m'han donat i la confiança que han tingut sempre en mi.

I per acabar, vull agraïr profundament el suport incondicional que m'ha donat el meu company Lluis al llarg de tots aquests anys. A ell també he d'agraïr-li tot l'amor que m'ha donat, molts bons moments i, sobretot, que hagi estat sempre fent-me costat.

Barcelona, 14 de febrer de 2007.

Contents

Part I

Resum en català

Capítol 1

Introducció, resum de resultats i conclusions

Aquesta tesi s'emmarca dins de l'estudi de les inestabilitats hidrodinàmiques [Drazin 02; Chandrasekar 81]. Aquesta àrea de recerca té molt d'interès en moltes disciplines (meteorologia, oceanografia, astrofísica, aeronàutica). L'interès en inestabilitats hidrodinàmiques es remunta possiblement al segle XV, quan Leonardo da Vinci descriu i dibuixa el fluxe turbulent de l'aigua. En general la inestabilitat hidrodinàmica és el resultat de la competició de forces estabilitzadores amb forces desestabilitzadores. James Clerk Maxwell va expressar clarament el concepte d'inestabilitat hidrodinàmica [Drazin 02]: un fluxe es considera inestable si una pertorbació infinitament petita de l'estat present del fluxe el porta a un estat diferent en un temps finit. Al segle XIX, gràcies a la feina de Helmholtz, Kelvin, Rayleigh i Reynolds els problemes fonamentals de l'estabilitat hidrodinàmica es van formular.

En aquesta tesi ens ocuparem de l'estudi de l'estabilitat de dos sistemes molt diferents. El primer d'ells és el dit de Saffman–Taylor, sobre el que s'han publicat nombrosos treballs [Pelcé 88]. Nosaltres ens vam centrar en aplicar pertorbacions a l'estat estacionari del dit. Aquest estudi està inclòs en el problema més general de formació d'estructures en interfícies: formació de dendrites en solidificació direccional, fractures...[Pelcé 88].

També ens vam centrar en caracteritzar el fluxe oscil·latori d'un fluid viscoelàstic. La fenomenologia que s'observa en fluids complexos [Bird 87] és molt sovint molt diferent de la que s'observa en fluids Newtonians. L'estabilitat hidrodinàmica pot veure's fortament afectada per la reologia complexa dels fluids no Newtonians, donant lloc a noves inestabilitats que actualment són subjecte d'estudi experimental i teòric [Morozov 05; Groisman 00; Berret 97].

En els nostres experiments vam observar que l'estructura del fluxe en el règim laminar es veia fortament afectada per les propietats viscoelàstiques del material. I que, com a resultat, el fluxe es desestabilitzava fins i tot a valors molt petits del nombre de Reynolds.

Aquesta tesi ha comportat l'estudi experimental d'inestabilitats interficials en fluids Newtonians i d'inestabilitats en fluxes viscoelàstics. Això va requerir l'aprenentatge de tècniques experimentals diverses, cosa que constitueix una formació experimental excel·lent per a treballs futurs.

1.1 Introducció

1.1.1 Dits de Saffman–Taylor

Des que va ser observada per primera vegada per Saffman i Taylor el 1958 [Saffman 58], molts autors han estudiat el fenomen de digitació viscosa (veure [Pelcé 88; Couder 00; Bensimon 86-b] per un estudi bibliogràfic complert) . En un principi, la recuperació de petroli va motivar l'estudi del fenomen però més tard la inestabilitat de Saffman–Taylor va atreure l'atenció de científics interessats en la formació d'estructures. El sistema experimental que es necessita per estudiar la inestabilitat és relativament senzill d'implementar. D'altra banda, encara que la inestabilitat de Saffman–Taylor és un fenomen altament no lineal i no local és encara suficientment simple com per a permetre algun estudi analític.

Una cel·la de Hele–Shaw [Hele–Shaw 1898] és un sistema format per dues plaques de vidre paral·leles separades una distància b molt més petita que qualsevol altra distància característica del sistema. El fluxe promig d'un fluid a la cel·la de Hele–Shaw és potencial i està governat per la llei de Darcy [Darcy 1856]:

$$\langle v_x \rangle = \frac{1}{b}\int_0^b v_x dz = -\frac{b^2}{12\eta}\frac{dp}{dx}. \tag{1.1}$$

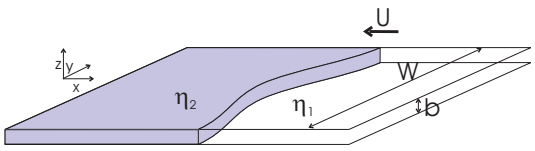

Figura 1.1: Esquema d'una cel·la de Hele Shaw plena de dos fluids amb viscositats η_1 i η_2. La interfície que separa ambdós fluids es fa inestable quan el menys viscós desplaça el més viscós.

on η és la viscositat del fluid i dp/dx el gradient de pressions al qual està sotmès el fluid. La inestabilitat de Saffman–Taylor es dóna a la interfície entre dos fluids que omplen la cel·la (Fig. 1.1) quan el més viscós és desplaçat pel menys viscós. El camp de velocitats a cada fluid està governat per la llei de Darcy i dues condicions de contorn. La primera és una condició cinemàtica i implica la continuïtat de la component normal de la velocitat a través de la interfície: $\mathbf{v_1} \cdot \mathbf{n} = \mathbf{v_2} \cdot \mathbf{n} \equiv \mathbf{U} \cdot \mathbf{n}$. L'altra és una condició dinàmica i relaciona la curvatura de la interfície amb el salt de pressions que hi ha a través de la mateixa (llei de Young–Laplace):

$$\delta p = \sigma\kappa = \sigma\left(\frac{1}{r_\parallel} + \frac{1}{r_\perp}\right), \tag{1.2}$$

on σ és la tensió superficial entre els dos fluids, $1/r_\parallel$ és la curvatura de la interfície en el pla x–y de la cel·la i $1/r_\perp$ és la curvatura de la interfície a la direcció z. Aquesta condició de contorn dinàmica fa que la resolució del problema de digitació viscosa sigui molt complexa.

L'estabilitat lineal de la interfase entre dos fluids[1] en la cel·la de Hele–Shaw s'estudia a partir de la evolució d'una pertorbació a la interfase plana de molt baixa amplitud i nombre d'ona k. La taxa de creixement σ de la pertorbació ve donada per la relació de dispersió lineal [Pelcé 88]:

$$\omega = U|k|\left(1 - \frac{b^2}{12\mathrm{Ca}}k^2\right), \tag{1.3}$$

on apareix el nombre de capil·laritat $\mathrm{Ca} = \eta U/\sigma$, que compara les forces viscoses amb la tensió superficial entre els dos fluids. La longitud d'ona més inestable del sistema ve donada per la longitud capil·lar: $l_c = \pi b/\sqrt{\mathrm{Ca}}$. La interfase entre dos fluids en un canal d'amplada W és inestable per valors del nombre de capil·laritat modificat $1/B$ [Tabeling 86]:

$$\frac{1}{B} = 12\left(\frac{W}{b}\right)^2 \mathrm{Ca} > (2\pi)^2. \tag{1.4}$$

Un cop la interfase es desestabilitza el creixement de la pertorbació és exponencial i ja no podem estudiar la evolució amb un model lineal. En el sistema té lloc un fenomen de competició en el que un dit d'amplada λW sobreviu i viatja pel centre del canal a una velocitat U (Fig. 1.2). Aquest és l'anomenat dit de Saffman–Taylor. L'amplada del dit depèn només de $1/B$ [Tabeling 87].

[1] Considerarem a partir d'ara que un dels dos fluids és aire, amb $\eta_1 \simeq 0$.

Inestabilitats en dits de Saffman–Taylor no pertorbats

Estudis numèrics i teòrics sobre l'estabilitat de dits de Saffman–Taylor amb tensió superficial finita van trobar que els dits eren linealment estables a pertorbacions induïdes per un possible soroll present al sistema [Bensimon 86] per $1/B \to \infty$. Els experiments han trobat sistemàticament que els dits a $1/B$ alts són inestables [Park 85; Lajeunesse 00; Kopf–Sill 88].

Experiments fets en cel·les llargues amb una relació d'aspecte W/b alta van trobar una inestabilitat lateral en els dits de Saffman–Taylor [Moore 02]. En aquests experiments s'observà que l'amplitud de la pertorbació decreixia a mesura que augmentava el nombre capil·lar seguint una llei de potències $\mathrm{Ca}^{-2/3}$. Els autors van descartar les possible inhomogeneitats en l'espaiat de la cel·la com a responsables de la inestabilitat.

Pertorbació de dits de Saffman–Taylor

En aquesta secció parlarem de treballs en els quals els autors van afegir una pertorbació controlada als dits viscosos [McCloud 95]. Alguns dels exemples de pertorbacions són:

- **Gradient en l'espaiament entre plaques.** A la ref. [Zhao 92], es va provocar un gradient uniforme en l'espaiament entre plaques. Quan el gradient era positiu la punta del dit era més plana i més inestable, per gradients negatius es va observar el comportament contrari.

- **Cel·les angulars.** Quan l'ample de la cel·la no és constant, no es poden formar dits estacionaris [Thomé 89]. En aquestes cel·les s'observen dits viatjant pel centre del canal que es fan inestables per valors de $1/B$ menors que per al cas de costats paral·lels [Lajeunesse 00].

- **Fils, ranures i bombolles: Dits de Saffman–Taylor anòmals.**

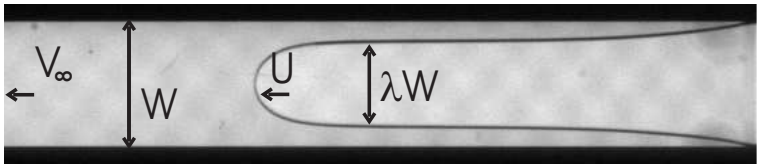

Figura 1.2: Notació usada pels paràmetres importants del problema: velocitat del fluxe lluny de la punta V_∞, velocitat del dit U, amplada de la cel·la W, amplada del dit λW.

Quan la pertorbació que s'aplica està localitzada i és molt propera a la punta, es pot accedir experimentalment a una familia de dits amb una amplada substancialment menor de la meitat del canal que no s'observen mai en absència d'anisotropia. Aquests dits s'han observat experimentalment per dits pertorbats amb bombolles a la punta [Couder 86], també per dits en cel·les amb dues ranures al centre [Rabaud 88]. Els dits pertorbats amb un fil només es veien afectats si el fil intersectava el dit a prop de la punta [Zocchi 87; Rabaud 88]. Es va observar que aquests dits eren estables fins a valors més alts de $1/B$ que els dits no pertorbats.

- **Pertorbacions periòdiques.**

  A la ref. [Gland 03], l'estabilitat d'una interfície oli–aire en una cel·la circular es va incrementar mitjançant un forçament periòdic.

Dits de Saffman–Taylor en fluids complexos

Actualment, una part important dels estudis que es fan sobre digitació viscosa es fan per fluids complexos. La fenomenologia que s'observa és diferent de la que s'observa per a fluids Newtonians. Per exemple, quan el fluid desplaçat presenta una forta plasticitat els dits es fan més estrets [Corvera–Poiré 98; Ben Amar 99; Lindner 00b; Lindner 00c]

Quan entra en joc la elasticitat el que passa és el contrari, els dits es fan més amples i el valor constant $\lambda = 0.5$ que s'assoleix a altes velocitats per als fluids Newtonians és significativament més alt per als fluids elàstics [Lindner 00; Bonn 97], fins i tot quan els fluids elàstics també presenten plasticitat [Bonn 95].

El forçament periòdic de dits de Saffman–Taylor en fluids complexes també prediu que les propietats reològiques complexes del fluid tenen un efecte important en els dits desenvolupats [Folch 01; Corvera–Poiré 04]

1.1.2 Fluids complexos

El terme fluid complex es fa servir per definir diferents classes de materials que es comporten com un fluid (es deformen contínuament quan se'ls aplica un esforç) però no presenten les característiques d'un fluid Newtonià. Per exemple, trobem fluids que tenen una viscositat menor sota velocitats de deformació grans (moltes dissolucions polimèriques presenten aquest comportament; el comportament contrari el presenten només uns pocs materials). També existeixen materials que es comporten com a sòlids quan se'ls sotmet a esforços petits, mentre que flueixen a esforços grans. Altres

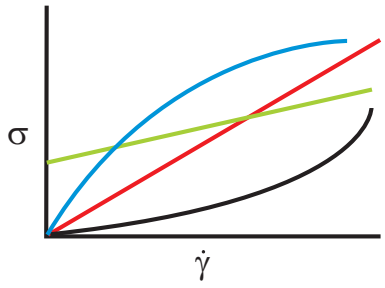

Figura 1.3: Esquema de les diferents respostes a un esforç aplicat: Newtoniana (vermella), pseudoplàstica (blava), dilatant (negra), yield–stress (verda). σ és l'esforç de cisalla aplicat i $\dot{\gamma}$ és la velocitat de cisalla resultant.

materials tenen un comportament a mig camí entre el d'un sòlid de Hooke (elàstic) i el d'un fluid Newtonià (dissipatiu); aquests fluids es coneixen amb el nom de fluids viscoelàstics. Hi ha més tipus de fluids complexos i també hi ha materials que poden presentar més d'una de les propietats descrites aquí a la vegada. Una descripció detallada del tema es pot trobar a les Refs. [Larson 99; Bird 87; Gelbart 96].

Fluids Newtonians, viscoelàstics i Newtonians generalitzats

La propietat principal dels fluids Newtonians és la seva viscositat. Aquesta viscositat és una constant del material que dóna compte de la dissipació d'energia en el fluid deguda a friccions internes [Guyon 94]. El moviment d'un fluid Newtonià está governat per les equacions de Navier–Stokes [Batchelor 90].

Els fluids no Newtonians tenen un comportament molt diferent. Per exemple, els fluids viscoelàstics presenten un comportament que es troba entre el d'un sòlid elàstic i el d'un fluid viscós. Els esforços aplicats al fluid no relaxen instantàniament, com en el cas dels fluids Newtonians sinó que triguen un cert temps en decaure. Hi ha dos paràmetres que mesuren l'elasticitat en els fluids viscoelàstics: el nombre de Deborah De (que compara l'escala de temps característica del fluid amb l'escala de dissipació viscosa característica del fluxe) i el nombre de Weissenberg Wi (que compara l'escala de temps característica del fluid amb l'escala de temps característica de deformació d'un element del fluid).

Un gran diferència entre els fluids Newtonians i els no Newtonians és la presència d'esforços normals en els fluids viscoelàstics [Bird 87] que fa que aparegui una força extra en la direcció normal al fluxe i que és responsable de molts fenomens observats en fluids viscoelàstics.

Els fluids Newtonians generalitzats són fluids no elàstics que tenen una viscosi-

tat depenent dels esforços aplicats al fluid. En general les cisalles provoquen una orientació de les molècules del fluid que fan que el material flueixi més fàcilment a esforços de cisalla alts; aquesta propietat s'anomena plasticitat.

Fluids de Maxwell

Un tipus particular de fluid viscoelàstic són les dissolucions aquoses de surfactant (mol·lècules anfifíliques que contenen un grup hidròfob i un d'hidròfil) que a determinades concentracions formen micel·les cilíndriques [Rehage 88]. En el rang de concentracions on es formen micel·les, el comportament del fluid ve molt ben descrit per l'equació constitutiva[2]:

$$\tau + t_m \frac{\partial \mathbf{tau}}{\partial t} = -\eta \dot{\gamma}, \tag{1.5}$$

que relaciona l'esforç τ amb la velocitat de deformació $\dot{\gamma}$ per un fluid de Maxwell amb una viscositat constant η i un temps de relaxació t_m.

Inestabilitats elàstiques

L'existència d'esforços normals en els fluids viscoelàstics fa que la fenomenologia observada en fluxes viscoelàstics sigui en molts casos diferent de l'observada en fluxes Newtonians. Un exemple d'aquest diferent comportament són les inestabilitats elàstiques que són causades pels esforços normals en fluxes on la inèrcia és molt petita ($\mathrm{Re} \ll 1$) [Groisman 00; Pakdel 96].

Permeabilitat dinàmica

La teoria lineal presentada a la Ref. [del Río 98] descriu la resposta dinàmica d'un fluid de Maxwell en un tub. Fent servir l'equació de moment linealitzada, la incompressibilitat i l'equació constitutiva del fluid de Maxwell (Eq. (1.5)), aquesta teoria prediu una resposta ressonant del sistema a freqüències determinades per les propietats del fluid i la geometria del sistema. Per contra, la resposta del fluid Newtonià decreix monotònicament amb la freqüència.

A la Figura 1.4 es mostra la resposta adimensional d'un fluid Newtonià (esquerra) i un fluid de Maxwell (dreta) [Castrejón-Pita 03b] per al cas particular d'un forçament periòdic. Es pot veure que la teoria lineal prediu molt bé la posició dels pics.

[2]Equació que relaciona la distribució d'esforços amb el camp de velocitats de deformació.

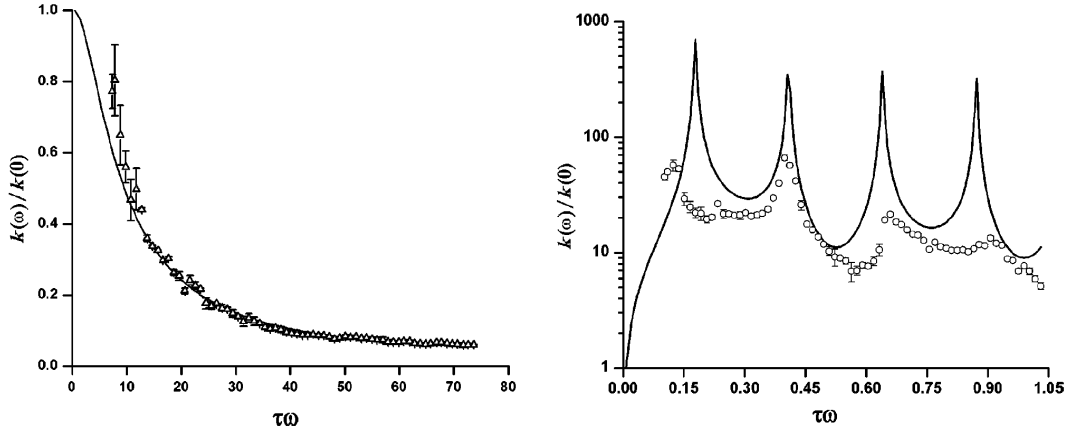

Figura 1.4: Cercles: Mesures a l'eix del tub de la resposta dinàmica d'un fluid sotmès a un forçament periòdic. Línies: predicció teòrica. La permeabilitat s'adimensionalitza dividint-la per $k(0) = -a^2/8$. **Esquerra:** Mesures per un fluid Newtoniá: glicerina. **Dreta:** Mesures per un fluid de Maxwell: CPyCl/NaSal 100/60 mM. Les dues extretes de [Castrejón-Pita 03b].

1.2 Inestabilitats laterals en dits de Saffman–Taylor

Els dits viscosos que s'observen en cel·les amb anisotropia tenen sempre una amplada major que la meitat del canal i fins fa molt poc no s'havia observat cap inestabilitat en els costats plans d'aquests dits. Recentment Moore *et al.* [Moore 02] van estudiar dits en canals molt amples que presentaven una inestabilitat lateral.

Més tard, un estudi numèric de la inestabilitat lateral en dits de Saffman-Taylor [Ledesma-Aguilar 05; Quevedo–Reyes 06] va predir el desenvolupament d'una inestabilitat lateral en dits de Saffman–Taylor sotmesos a petites pertorbacions. Aquest estudi va motivar gran part dels experiments presentats en aquesta tesi.

1.2.1 Muntatge experimental

Els experiments es van realitzar en una cel·la de Hele–Shaw horitzontal (Fig. 1.5) formada per dues plaques de vidre de longitud $L = 1300$ mm separades per un espaiador de llautó. Es van realitzar experiments en un canal d'amplada $W = 24$ mm en el cas del desordre estàtic i d'amplada $W = 25$ mm en el cas de la pertorbació periòdica. L'entrada d'aire i la sortida d'oli consistien en dues obertures situades als extrems de la placa inferior. La sortida d'oli es va connectar a una bomba de xeringa que podia injectar o extreure oli a velocitat constant en el rang $(-1.1, 1.1)$ cm^3/s.

La cel· es va il·luminar des de sota amb una làmpada fluorescent d'alta freqüència. Imatges de la cel·la es capturaven amb una CCD situada sobre la cel·la que podia viatjar al llarg del canal a velocitats en el rang -20 a 20 mm/s i capturar fins a 60

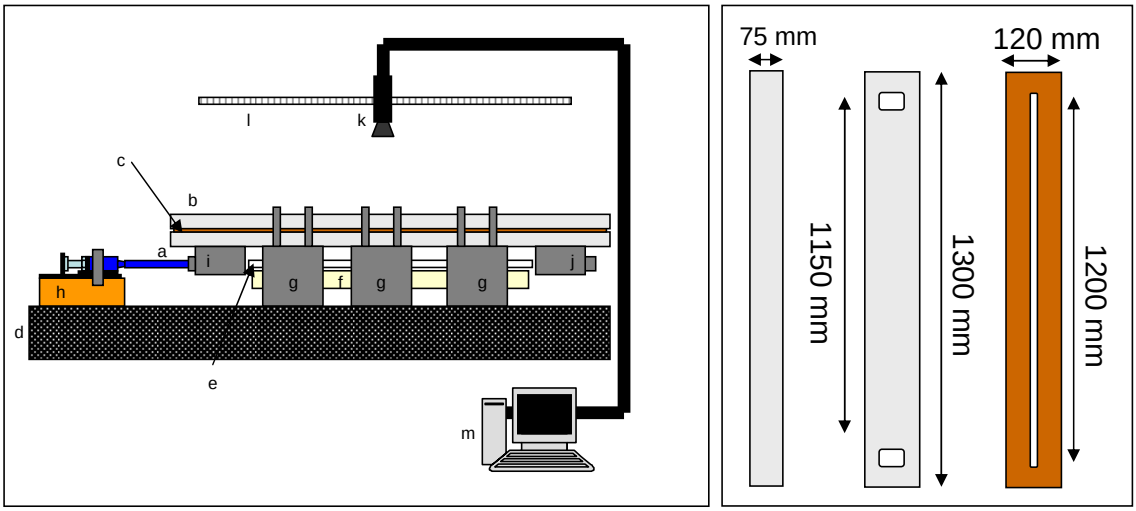

Figura 1.5: Esquerra: Esquema del muntatge experimental utilitzat en els experiments de digitació viscosa. (a) Placa inferior, (b) placa superior, (c) espaiador de llautó, (d) taula antivibració, (e) difusor, (f) fluorescent d'alta freqüència, (g) suports, (h) bomba, (i) sortida d'oli, (j) entrada d'aire, (k) càmera CCD, (l) rail, (m) PC. **Dreta:** Esquema de les plaques i l'espaiador de metall de la cel·la de Hele–Shaw

imatges de 640×480 píxels cada segon.

En tots els experiments es van generar dits d'aire penetrant en oli de silicona (Rhodorsil 47V500) amb una viscositat dinàmica $\eta = 0.518 \pm 0.002$ Pa·s a 20°C, densitat $\rho = 975 \pm 10$ Kg/m^3 i tensió superficial oli–aire $\sigma = 20.7$ mN/m. Per tal d'incrementar el contrast aire–oli, l'oli es va colorejar amb Oil Blue N (Aldrich) sense canvis apreciables en les propietats de l'oli.

Desordre congelat

El desordre congelat es va generar fixant una placa de fibra de vidre a la placa inferior de la cel·la. El desordre consistia en unes illes de coure de dimensions fixes (1.5×1.5 mm i alçada $h = 0.06$ mm) distribuïdes aleatòriament sobre la fibra de vidre [Soriano 03]. Els experiments es van fer amb dos tipus de plaques: plaques amb alta ocupació (35% de l'àrea total ocupada per illes de coure) i plaques amb baixa ocupació (10% de l'àrea total ocupada per illes de coure). Es van fer experiments amb un espaiament efectiu entre plaques (mesurat com la distància entre la fibra de vidre i la placa superior) de 0.8 i 1.3 mm.

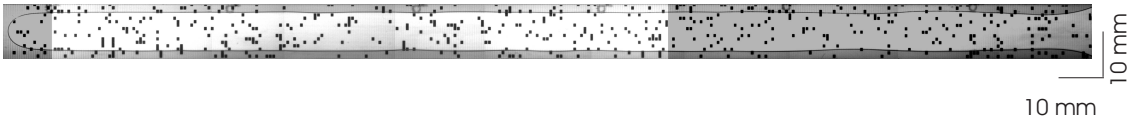

Figura 1.6: Exemple d'un dit generat en els experiments amb desordre estàtic amb $b = 0.8$ mm, 10% de l'àrea total ocupada per illes de coure. La velocitat promig del dit era $U = 2$ mm/s. La regió brillant del dit és la zona on es va estudiar la inestabilitat.

Pertorbació periòdica

En els experiments amb un dit sotmès a un forçament periòdic l'espaiat entre plaques era $b = 1$ mm. El forçament periòdic es va fer mitjançant una bomba que es va connectar a l'entrada d'aire. La bomba admetia aire quan el volum d'aire dins la bomba era màxim, per tal de permetre que el dit avancés. La bomba funcionava a freqüències fins a 1.5 Hz.

Mètodes experimentals

Per començar introduirem dues escales de temps presents al sistema en absència de pertorbacions que tenen molta importància en el sistema. La primera escala temporal ens dóna una freqüència del dit característica:

$$\nu_{finger} = \frac{V_\infty}{\lambda^2 W}, \tag{1.6}$$

on W és l'amplada del canal, V_∞ la velocitat d'extracció de l'oli i λ l'amplada adimensional promig del dit. L'altra freqüència característica és:

$$\nu_\infty = \frac{V_\infty}{W}, \tag{1.7}$$

Es va mesurar la longitud d'ona Λ de la inestabilitat com la distància entre dos màxims adjacents; a cada longitud d'ona se li va associar una freqüència:

$$\nu_{out} = \frac{V_\infty}{\lambda\Lambda} \tag{1.8}$$

En el cas dels dits en cel·les amb desordre congelat, es va identificar una regió on la inestabilitat era estacionària i es van reconstruir imatges de dits llargs mitjançant fotografies preses amb la càmera viatjant al llarg del canal. A la figura 1.6 es mostra una imatge d'un d'aquests dits.

Per als dits sotmesos a una pertorbació periòdica es va estudiar com evolucionava la inestabilitat lateral en una regió fixa de la cel·la. En el sistema de referència del dit això correspondria a estudiar l'evolució de la inestabilitat a mesura que s'allunyava

Figura 1.7: Exemple d'un dit generat en els experiments amb un forçament periòdic. La freqüència de forçat era 0.22 Hz i $V_\infty = 1.42$ mm/s. La regió brillant correspon a la zona que es va analitzar.

de la punta. Els resultats que presentem aquí corresponen a estats estacionaris que assolia la inestabilitat lateral. Vam fer cinc repeticions de cada experiment per tal de millorar la nostra estadística. A la figura 1.7 es mostra un exemple dels dits observats al laboratori.

A banda de la freqüència de la inestabilitat lateral també es van mesurar les fluctuacions en l'amplada del dit. Es va digitalitzar la regió d'anàlisi i es va mesurar l'amplada local del dit $\lambda(x_i)$. D'aquesta amplada local es va mesurar l'amplada promig $\lambda = 1/N \sum_i \lambda(x_i)$ i es van calcular les fluctuacions a través de la desviació estàndard de $\lambda(x_i)$:

$$\delta_\lambda = \sqrt{\frac{1}{N-1} \sum_i (\lambda - \lambda(x_i))^2}. \tag{1.9}$$

1.2.2 Principals resultats

La inestabilitat lateral que es va mesurar en els dits sotmesos als dos tipus de pertorbació periòdica tenia una longitud d'ona llarga i una amplitud baixa.

Desordre estàtic

Es va estudiar l'efecte de les propietats del desordre en la inestabilitat variant la intensitat del desordre (o l'espaiat entre plaques) i el cobriment (tant per cent d'àrea total de la cel·la ocupat per illes de coure). Es va observar que com més intens era el desordre més gran era l'amplitud de la inestabilitat, mentre que la intensitat del desordre no afectava a la distribució de freqüències de la inestabilitat lateral. L'amplitud de la inestabilitat també creix amb el cobriment.

També es va estudiar la relació entre la inestabilitat i el nombre de capil·laritat modificat $1/B$ per a un espaiat $b = 1.3$ mm i una ocupació del 10%. Es va comparar l'amplada mitja del dit amb l'amplada de dits sense pertorbacions (Fig. 1.8) i es va veure que els resultats tenien un bon acord amb els resultats del cas estacionari [Tabeling 86].

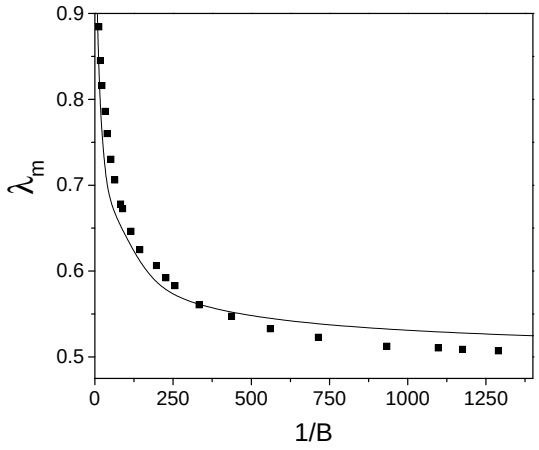

Figura 1.8: Amplada mitja del dit en funció de $1/B$. La línia correspon als valors teòrics de McLean i Saffman [McLean 81]. Els quadrats són els valors experimentals resultat de promitjar sobre quatre configuracions de desordre diferents.

Es va estudiar la relació entre l'amplitud de la inestabilitat lateral i el nombre de capil·laritat modificat. Com es pot veure a la Figura 1.9, la relació entre Ca i l'amplitud de les fluctuacions és clarament no monotònica mentre que a valors moderats de $1/B$ (per sota de 250) l'amplitud de les fluctuacions escala amb $1/B$: $\delta_\lambda = (0.034 \pm 0.008)(1/B)^{(-0.30\pm0.13)}$. A valors de $1/B$ més alts l'amplitud de la inestabilitat creix.

També es va mesurar la distribució de freqüències de la inestabilitat en funció de

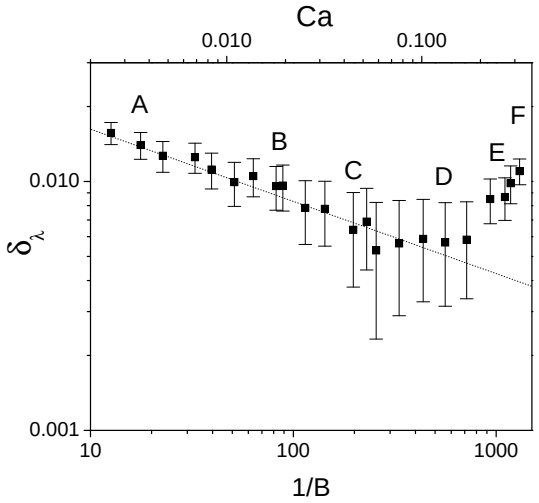

Figura 1.9: Fluctuacions a l'amplada del dit vs $1/B$. Els quadrats són els resultats experimentals resultat de promitjar sobre quatre realitzacions diferents del desordre. La línia de punts és el millor ajust al comportament a la zona de velocitats baixes ($1/B$ des de 0 a 250).

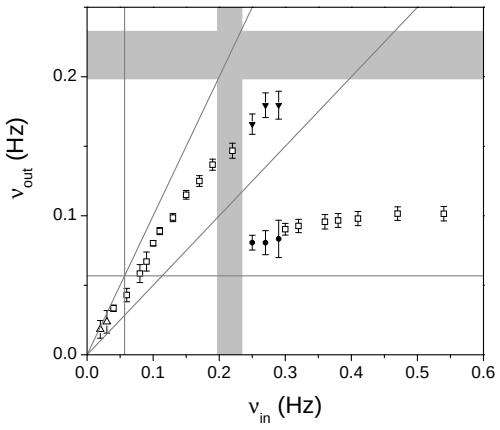

Figura 1.10: Freqüència de la inestabilitat lateral en funció de ν_{in} per a una velocitat d'extracció de l'oli $V_\infty = 1.42$ mm/s. □: Estats estacionaris. △: Transformada de Fourier de dits llargs. • i ▼: Estats no estacionaris. Les línies grises marquen la posició de ν_∞. Les bandes grises horitzontal i vertical marquen el rang on estan compreses les freqüències característiques del dit ($\nu_{fing-min}$, $\nu_{fing-max}$). També es pinten $y = x$ i $y = x/2$ com a guies per l'ull.

$1/B$. Es va veure que tant el valor mig com l'amplada de la distribució de freqüències de la inestabilitat creixien linealment amb el nombre de capil·laritat modificat.

Finalment, l'estudi de la distribució de longituds d'ona de la inestabilitat ens va mostrar que per a totes les velocitats la longitud d'ona preferida pel sistema era molt propera a l'amplada de la cel·la.

Pertorbació periòdica

Es va observar una inestabilitat simètrica i periòdica per a totes les freqüències de forçat. Es van fer experiments a dos velocitats diferents ($V_\infty = 1.42$ i 2.83 mm/s).

Es va observar que l'amplitud de la pertorbació no tenia una relació monotònica amb la freqüència del forçat. Per a les dues velocitats d'extracció es va observar que l'amplitud de la pertorbació era molt petita a freqüències de forçat altes. També es va veure que l'amplada del dit no era uniforme, de manera que es va definir una banda de freqüències característiques al sistema:

$$\nu_{fing-min} = \frac{V_\infty}{\langle\lambda\rangle^2_{max} W}, \tag{1.10}$$

$$\nu_{fing-max} = \frac{V_\infty}{\langle\lambda\rangle^2_{min} W}, \tag{1.11}$$

Les primeres etapes de la inestabilitat eren molt similars a tots els experiments: la inestabilitat apareix a prop de la punta del dit, poc després de que la bomba d'aire

fos encesa. L'efecte de la bomba és un canvi instantani en la velocitat de la punta del dit que avança a una velocitat més alta o més baixa. Com a resultat, l'amplada del dit es modula al voltant d'un valor mig amb una freqüència en el rang ($0.4\nu_{in}$, ν_{in}).

Lluny de la punta observem tres tipus de comportament a diferents freqüències de forçat (Fig. 1.10):

- **Règim depenent de la freqüència del forçat ($\nu < \nu_{fing_{min}}$):** En aquesta regió la freqüència resposta ν_{out} és completament periòdica i l'estat estacionari s'assoleix molt a prop de la punta. La freqüència resposta depèn fortament de la freqüència de forçat: evoluciona suaument des de $\nu_{out} \simeq \nu_{in}$ a molt baixes freqüències fins a $\nu_{out} \simeq \nu_{in}/2$ a freqüències de l'ordre de $\nu_{fing-min}$.

- **Règim de resposta no saturada:** Per a una petita banda de freqüències la freqüència observada molt a prop de la punta es desestabilitzava però no arribava a un estat estacionari. En alguns dels casos la inestabilitat lateral evolucionava cap a un estat amb una longitud d'ona molt més gran que la de l'estat inicial.

- **Règim de selecció:** A freqüències per sobre de $\nu_{fing-max}$, el perfil observat molt a prop de la punta evolucionava cap a un perfil estacionari amb una longitud d'ona molt més gran que la de prop de la punta. Aquesta longitud d'ona era de l'ordre de l'amplada del canal.

1.3 Fluxe oscil·latori d'un fluid de Maxwell en un tub

L'acoblament entre el fluxe i les propietats del fluid fa que la resposta dinàmica dels fluids no Newtonians (complexos) sigui molt més rica que la dels fluids Newtonians (simples) [Larson 99]. En particular, i depenent de l'escala temporal rellevant del sistema, els fluids viscoelàstics presenten un comportament dissipatiu propi dels fluids viscosos ordinaris i un comportament elàstic característic dels sòlids. El comportament elàstic fa que siguin uns candidats potencials a presentar fenòmeNs ressonants en diferents condicions de fluxe.

La resposta d'un fluid viscoelàstic a un gradient de pressió oscil·lant ha estat analitzaDA teòricament (veure Sec. 1.1.2 per detalls). La resposta, mesurada com la velocitat a una amplitud del gradient de pressió donada, excedeix la d'un fluid ordinari en varis ordres de magnitud a diverses freqüències. Aquesta amplificació de

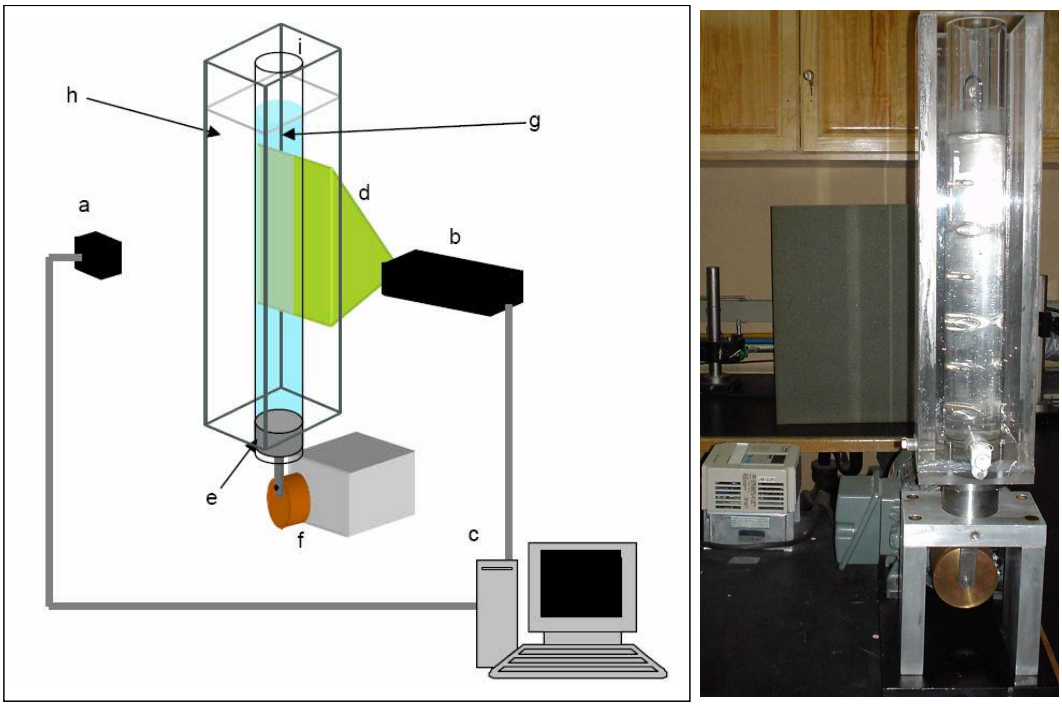

Figura 1.11: Esquerra: Esquema del sistema de PIV: (a) Càmera de PIV, (b) Làser PIV, (c) Processador del PIV, (d) full de llum, (e) pistó de tefló, (f) motor, (g) fluid estudiat, (h) glicerina, (i) cilindre acrílic. **Dreta:** Imatge del sistema experimental.

la resposta s'atribueix a un efecte ressonant degut a les propietats elàstiques del fluid i a la geometria del contenidor [López de Haro 96; del Río 98; Tsiklauri 01].

Aquest efecte ressonant va ser comprovat experimentalment [Castrejón-Pita 03b] però el model conté encara moltes prediccions interessants que no s'havien comprovat experimentalment (l'estructuració del fluxe en regions de velocitat alternant, la dependència dels pics de ressonància amb els paràmetres experimentals) que nosaltres vam desenvolupar en els nostres experiments. A més, també vam caracteritzar una inestabilitat del fluxe viscoelàstic a amplituds de forçament per les quals el fluxe Newtonià era completament laminar.

1.3.1 Muntatge experimental

En la caracterització del fluxe oscil·lant d'un fluid de Maxwell en un tub es van fer servir quatre tècniques experimentals diferents: anemometria de làser Doppler (LDA), deflectometria Òptica (OD) [Fermigier 92], velocimetria d'imatge de partícules (PIV) [Adrian 91] i birrefringència[Lerouge 00].

El sistema experimental (Fig. 1.11) consistia en un cilindre vertical fet amb un

material acrílic transparent, de radi interior $a = 25$ mm i alçada 500 mm, ple del fluid a estudiar. Per tal d'evitar aberracions òptiques, el cilindre es va col·locar dintre d'un segon recipient acrílic de secció quadrada, ple de glicerol (que té un índex de refracció molt similar al del material acrílic). Un pistó de tefló a la part inferior del cilindre, mogut per un motor de freqüència variable, produïa oscil·lacions harmòniques del gradient de pressions a la columna de fluid. L'amplitud de l'oscil·lació podia ser modificada canviant l'eccentricitat de la roda que movia el pistó. Es van estudiar amplituds d'oscil·lació $z_0 = 0.8, 1.2, 1.6, 2.0$ i 2.5 (± 0.05) mm.

Els camps de velocitat en un pla vertical que tallava l'eix de simetria del tub es van mesurar per PIV 2–d. El nostre sistema PIV tenia una unitat làser de dos polsos Nd-Yag, que incloïa un arranjament òptic per produir un full de llum en un pla vertical del cilindre (Fig. 1.11). Una CCD (Kodak E1.0, resolució 1008 $\times$ 1016 píxels), perpendicular al full de llum, es va fer servir per capturar imatges digitals. La càmera capturava parelles d'imatges, cadascuna en un dels polsos del làser. La càmera capturava a una velocitat màxima de 1.5 Hz. Un processador *Dantec FlowMap 1100* s'ocupava de la sincronització del làser i la CCD. El processat de les imatges es va fer amb el programa comercial *Dantec FlowMap v5.1* software. Com a partícules traçadores es van fer servir esferes de poliamida de 20–μm *Dantec*.

Els fluids Newtonians usats en els experiments (oli de silicona de densitat $\rho = 973$ Kg/m^3 i viscositat $\eta = 56$ Pa·s i glicerina de densitat $\rho = 1250$ Kg/m^3 i viscositat $\eta = 1$ Pa·s) es van fer servir per comparar el seu comportament amb el comportament dels fluids Maxwelians.

Les dissolucions viscoelàstiques es van preparar dissolent Cetylpiridinium Chloride (CPyCl) i Salicilat de Sodi (NaSal) (els dos de Sigma) en aigua destil·lada. La major part dels experiments es van fer amb una dissolució de concentració [100/60] mM (de densitat $\rho = 1050$ Kg/m^3, viscositat $\eta = 60$ Pa·s i temps de Maxwell $t_m = 1.8$ s). En els altres es va fer servir la dissolució CPyCl/NaSal [40/40] mM (de densitat $\rho = 1005$ Kg/m^3, viscositat $\eta = 30$ Pa·s i temps de Maxwell $t_m = 1.25$ s).

1.3.2 Principals resultats

Permeabilitat dinàmica per diferents fluids de Maxwell

Vam fer mesures de LDA al centre del tub amb una amplitud de forçat $z_0 = 0.8$ mm per tal de reproduir la corba presentada a [Castrejón-Pita 03b] amb un fluid de Maxwell diferent, amb l'objectiu de verificar la relació entre la posició dels pics i el nombre de Deborah [del Río 98]. Els resultats (Fig. 1.12) mostren que efectivament

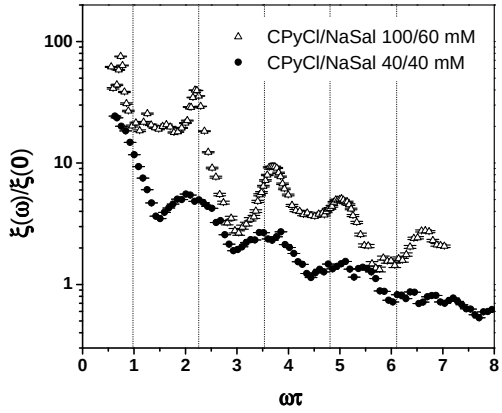

Figura 1.12: Funció de resposta adimensional al centre del cilindre, com a funció de la freqüència adimensionalitzada, per dos concentracions diferents de la dissolució de surfactant. Les línies verticals donen la posició de les freqüències ressonants predites per una teoria lineal

la posició dels pics escala com $\tau \propto t_m De^{-\frac{1}{2}}$.

Perfils de velocitat laminars

Mesures PIV dels perfils de velocitat a diferents distàncies de la interfície (6,10 i 25 cm) i $z_0 = 0.8$ mm ens van permetre veure que la forma dels perfils és independent de la distància a la interfície. D'altra banda, es va veure que l'amplitud dels perfils de velocitat era més baixa més a prop de la interfície. Les mesures es van fer per als tres primers màxims de la resposta dinàmica (2.0, 6.5 i 10.5 Hz) i per als tres primers mínims de la resposta dinàmica (3.5, 8.2 i 11.5 Hz).

La dependència dels perfils de velocitat amb la freqüència del forçat és molt més forta per al cas del fluid Maxwelià. A freqüències baixes (2.0, 3.5 Hz), els perfils de velocitat no tenen estructura, mentre que a freqüències creixents (Fig. 1.13 dreta) el fluxe s'organitza en regions de fluxe alternant separades per punts quiescents. Cada màxim de la resposta dinàmica presenta un parell més de punts quiescent que l'anterior. La posició d'aquests punts quiescents depèn de la geometria del sistema i de les propietats del fluid.

Per al fluid Newtonià, en canvi, els perfils de velocitat són molt similars a totes les freqüències i no s'observa en cap cas l'estructuració del fluxe (Fig. 1.13 esquerra).

Mitjançant mesures OD de la interfície aire/fluid caracteritzat es va veure que la posició d'aquests punts quiescents es mantenia constant a diferents distàncies de la superfície lliure de fluid. D'altra banda, els perfils de velocitat mesurats a la interfície van ser sistemàticament més baixos que els mesurats en el gruix del fluxe.

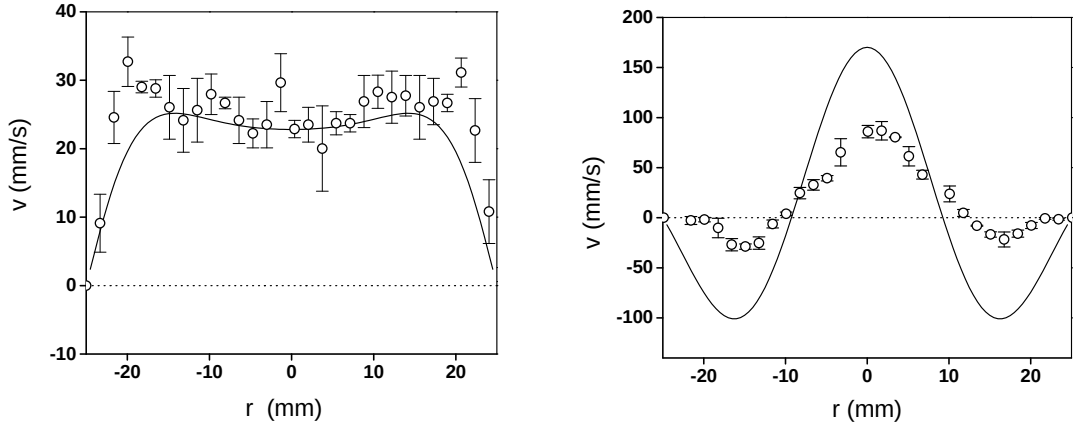

Figura 1.13: Mesures de PIV a $z_0 = 0.8$ mm, $\nu = 6.5$ Hz a 6 cm de la interfície lliure. La predicció teòrica es presenta amb una línia contínua i les mesures experimentals amb punts. **Esquerra:** Glicerina, $t = 0.115$ s. **Dreta:** 100/60 CPyCl/NaSal, $t = 0.038$ s.

Inestabilitat hidrodinàmica

Per a un fluid Newtonià amb viscositat i densitat similars a les del fluid viscoelàstic CPyCl/NaSal 100/60 mM es van mesurar camps de velocitat a freqüències en el rang 2.0 fins a 11.5 Hz. Es va veure que els camps de velocitat eren laminars fins a forçats d'amplitud 10 mm a totes les freqüències.

En el fluid viscoelàstic es va estudiar com afectava un increment de l'amplitud del forçat als camps de velocitat. Es van aplicar amplituds de forçat $z_0 = 0.8, 1.2, 1.6, 2.0$ i 2.5 mm i es van estudiar les freqüències corresponents als tres primers màxims de la resposta dinàmica (2.0, 6.5 i 10.5 Hz) i per als tres primers mínims (3.5, 8.2 i 11.5 Hz).

Per al primer màxim i primer mínim de la resposta dinàmica es va observar que els camps de velocitats eren laminars a totes les amplituds de forçat. Els camps de velocitat de freqüències que presentaven regions quiescents eren inestables a amplituds de forçat creixents. La simetria axial del camp de velocitats encara es preservava en aquest estadi del fluxe i la inestabilitat donava lloc a vòrtex toroïdals estacionaris amb una intensitat que seguia la periodicitat del forçat (Fig. 1.14). Aquests vòrtex toroïdals es van observar a freqüències 6.5, 8.2, 10.5 i 11.5 Hz. A amplituds altes del forçat($z_0 = 2.0$ i 2.5 mm) es perdia la simetria axial dels vòrtex.

Es van mesurar les fluctuacions en la velocitat del sistema tant per al component horitzontal ($\sigma_{v_x} = \sqrt{1/N \sum_i [v_x(x, y_i) - \overline{v_x}(x)]^2}$) com per al component vertical de la velocitat ($\sigma_{v_y} \sqrt{1/N \sum_i [v_y(x, y_i) - \overline{v_y}(x)]^2}$). Tot i que la magnitud de σ_{v_y} era sensiblement major que la de σ_{v_x} la informació que donaven era essencialment la mateixa. Es va calcular el promig espacial i temporal de les fluctuacions per obtenir una mesura

global de l'estabilitat del fluxe. Aquestes fluctuacions es van fer adimensionals amb la velocitat màxima del pistó: $\widetilde{\sigma}_{v_y} = \sigma_{v_y}/(2\pi\nu z_0)$ i es van representar en termes d'un paràmetre adimensional construït a partir del nombre de Weissenberg.

Com ja s'ha dit a la introducció, el nombre de Weissenberg compara l'escala de temps característica del fluid amb la velocitat de deformació característica d'un element de fluid. En el nostre sistema aquesta velocitat de deformació característica es construeix a través de la velocitat màxima del pistó i la posició del punt quiescent del fluxe més proper al centre del tub r_q:

$$\mathrm{Wi} = t_m \dot{\gamma}_{char} = t_m \frac{2\pi\nu z_0}{r_q}. \tag{1.12}$$

Com que la dinàmica observada en el sistema té un comportament periòdic amb un període $T = 1/\nu \ll t_m$ és molt probable que ν sigui una escala de temps molt més rellevant que t_m. Es defineix un nou paràmetre $\chi = \mathrm{Wi}/(\nu t_m)$ i s'observa que les fluctuacions en la velocitat col·lapsen (Fig. 1.15). El pas de mapes de velocitat estables a inestables es dona per un valor de $\chi \simeq 1$.

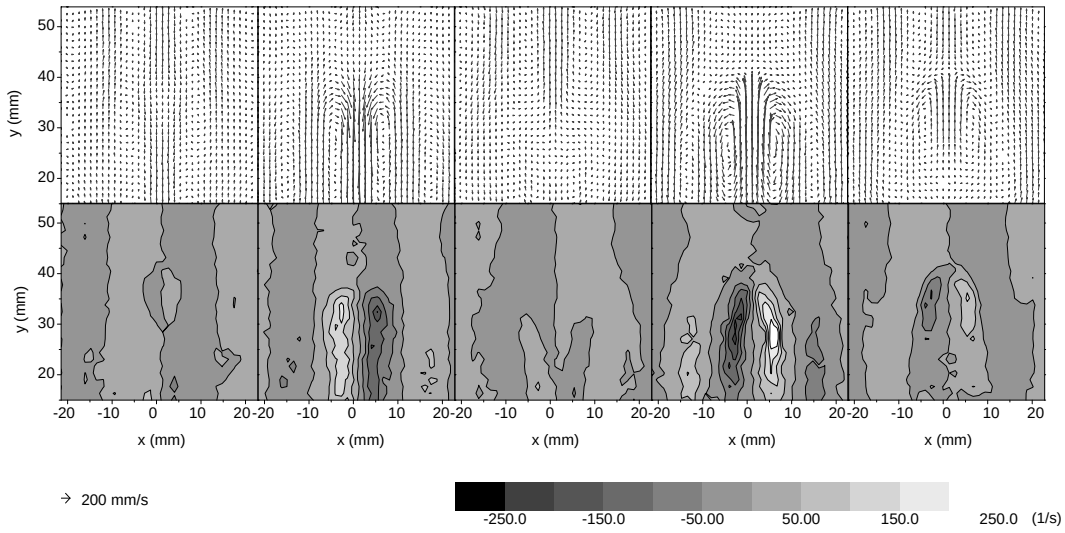

Figura 1.14: Dissolució 100:60 CPyCl/NaSal: resultats PIV per $\nu = 8.2$ Hz i $z_0 = 1.2$ mm. Es mostren imatges a temps t=0, $1/(4\nu)$, $1/(2\nu)$, $3/(4\nu)$ i $1/\nu$. Superior: camp de velocitats. Inferior: component azimutal de la vorticitat. Les escales corresponents es donen al peu de la figura.

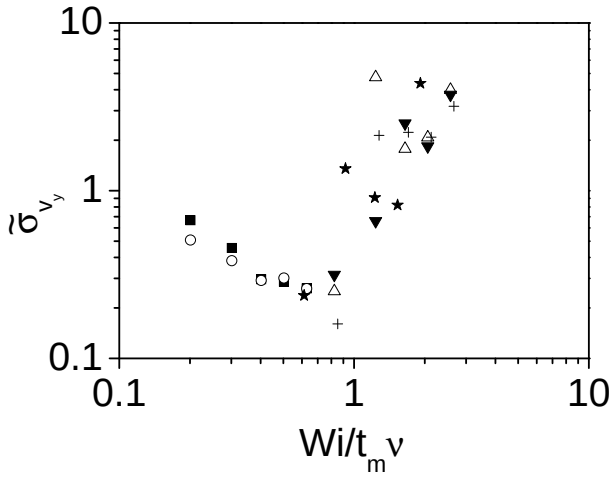

Figura 1.15: Dissolució 100:60 CPyCl/NaSalpromig espacial i temporal de les fluctuacions de la component y de la velocitat, en funció del paràmetre adimensional $\chi \equiv \frac{\mathrm{Wi}}{t_m \nu}$, a les diferents freqüències de forçat (en Hz): 2.0 (■), 3.5 (○), 6.5 (⋆), 8.2 (△), 10.5 (▼), i 11.5 (+).

1.4 Conclusions

1.4.1 Inestabilitats laterals en dits de Saffman–Taylor

Vam estudiar l'estabilitat dels costats plans del dit de Saffman–Taylor. Vam aplicar pertorbacions de dos tipus: desordre espacial estàtic i una pertorbació periòdica de la velocitat de la punta del dit.

Ambdues pertorbacions van produir una pertorbació de gran longitud d'ona i baixa amplitud als dos costats del dit. Als dos casos es va observar un fenomen de selecció que portava a una freqüència aproximadament igual a la meitat de la freqüència característica del dit.

En els experiments amb desordre congelat, la inestabilitat es va caracteritzar en un rang de velocitats molt ampli. Vam observar que l'amplitud de la inestabilitat dequeia amb la velocitat (o el nombre de capil·laritat en el nostre cas) amb un exponent $\delta_\lambda \propto \mathrm{Ca}^{-1/3}$. A velocitats molt altes, l'amplitud de la inestabilitat tornava a créixer.

Modulacions periòdiques de la velocitat del dit es van estudiar per a dues velocitats diferents, en un ampli rang de velocitats de forçament. La inestabilitat resposta que vam observar al dit va ser sempre simètrica i per la major part dels dits arribava a un estat estacionari. A freqüències baixes la forma de la inestabilitat lateral era fortament depenent de l'entrada, mentre que a freqüències altes s'observà un procés de selecció. En aquest procés, l'estat final al que arribava el dit estava caracteritzat per una freqüència molt menor que la freqüència d'entrada.

1.4.2 Fluxe oscil·latori d'un fluid de Maxwell en un tub

Vam usar quatre tècniques òptiques diferents (LDA, PIV, OD i birefringència) per caracteritzar el fluxe oscil·latori d'un fluid de Maxwell (una solució de CPyCl/NaSal en aigua) contingut en un tub vertical. Dos fluids Newtonians (glicerina i oli de silicona) van ser estudiats per a comparar el seu comportament amb el del fluid complex.

Les mesures per al centre del tub mostraren que el model lineal presentat a la Sec. 1.3 prediu acuradament la posició dels pics de ressonància en relació a les propietats reològiques del fluid.

Mesures de PIV del mapa de velocitats al gruix del fluxe mostraren que els perfils per al fluid Newtonià no tenien estructura, contràriament al que s'observà per al fluid complex. Aquest presentava regions de velocitat alternant separades per punts quiescents del fluxe. El nombre d'aquests punts quiescents augmentava a mesura que augmentava la freqüència del forçat i la seva posició era predita molt acuradament pel model lineal. Mesures a diferent distàncies de la interfase lliure (incloent mesures OD a la pròpia interfase) mostraren que la posició radial d'aquests punts quiescents era independent de la distància a la interfase lliure.

També vam realitzar mesures de PIV per al fluxe oscil·latori d'un fluid Newtonià i un Maxwelià amb viscositat i densitat similars a vàries amplituds de forçat. Mentre el fluxe Newtonià va resultar ser estable en tot el rang de paràmetres explorat, el de Maxwell es desestabilitzava quan s'augmentava l'amplitud del forçat, inclús mantenint Re molt petit. La primera inestabilitat observada donava lloc a vòrtex estacionaris toroïdals amb simetria axial. A mesura que augmentava l'amplitud del forçat, aquests vòrtex simples es desestabilitzaren donant pas a estructures més i més complexes. Aquests resultats són potencialment rellevants en la cerca de l'observació experimental d'una inestabilitat subcrítica en fluxes de cisalla amb línies de corrent paral·leles.

1.5 Perspectives futures

1.5.1 Inestabilitats laterals en dits de Saffman–Taylor

La caracterització de la inestabilitat lateral en funció de la velocitat es va fer només per als experiments amb desordre estàtic. En el cas de la pertorbació periòdica una mesura interessant i que ens donaria informació similar seria l'estudi de la longitud d'ona seleccionada a diferents velocitats.

També seria interessant realitzar experiments amb nous amples de cel·la per ambdues pertorbacions. Això permetria generar dits més llargs, determinar l'estat final dels punts propers a la freqüència característica del dit i també veure la dependència dels resultats amb $1/B$.

La combinació dels dos mecanismes de pertorbació és un altre punt interessant que no es va explorar en aquesta tesi. Vam observar que la inestabilitat lateral tenia una freqüència preferida, que coincidia aproximadament amb l'obtinguda en els casos de pertorbació periòdica. Una qüestió que va quedar sense resposta va ser l'efecte del soroll en el fenomen de selecció per un dit sotmès a una pertorbació periòdica. Sembla clar que la freqüència seleccionada seria la mateixa, però el procés dinàmic de selecció es podria veure afectat pel soroll. Per exemple, podria passar que el temps necessari per arribar a l'estat seleccionat final for significativament més curt gràcies a la presència del soroll.

1.5.2 Fluxe oscil·latori d'un fluid de Maxwell en un tub

La caracterització del perfil de velocitats laminar es va fer exhaustivament mitjançant vàries sèries d'experiments. Es va explorar un ample rang de freqüències i també es van canviar les propietats dels fluids. Una mesura interessant que encara quedaria pendent seria veure l'efecte que tindria canviar el radi del tub mantenint constants les propietats del fluid per tal de verificar l'escalament de les freqüències de ressonància predit a la Ref. [del Río 98]. També seria interessant fer mesures a baixes amplituds i freqüències altes per tal de poder determinar el màxim nombre de punts quiescents que podria presentar el mapa de velocitats.

D'altra banda, l'estudi de la inestabilitat encara té algunes preguntes obertes que no es van abordar durant aquesta tesi. Per començar, seria molt important determinar si el comportament pseudoplàstic té algun paper en el desenvolupament de la inestabilitat. Això es podria saber reemplaçant el fluid que es va fer servir en els experiments per un fluid no elàstic que presenti pseudoplasticitat o fent servir un fluid purament elàstic (fluid de Boger [Boger 96]).

El llindar de la inestabilitat no es podia caracteritzar amb el dispositiu experimental descrit en aquesta tesi. Per tal de determinar la mínima amplitud necessària per desestabilitzar el fluxe a una freqüència fixada es va dissenyar un nou dispositiu experimental que es descriu a l'Apèndix B. Aquest dispositiu permet el canvi continu de l'amplitud del forçat a freqüència fixada.

Les nostres mesures estaven dirigides a caracteritzar la primera inestabilitat observada al sistema. L'estudi a forçats de major amplitud i freqüència seria interessant

per tal de caracteritzar bifurcacions secundàries, que ja s'observaven en alguns dels nostres experiments. L'estudi d'aquests estadis més avançats, en els quals vam observar una pèrdua de simetria axial, requeriria noves tècniques de caracterització.

Part II

Thesis

Chapter 1

Framework

This thesis fits in the area of hydrodynamic instabilities [Drazin 02; Chandrasekar 81], This research area has great interest in many disciplines (meteorology, oceanography, aeronautics, astrophysics). The interest in hydrodynamic instability begins possibly as early as the XVth century, when Leonardo da Vinci describes and draws the turbulent flow of water. Generally speaking, hydrodynamic instability arises from the competition between stabilizing forces and destabilizing forces. James Clerk Maxwell expressed clearly the qualitative concept of hydrodynamic instability as follows [Drazin 02]: a flow is said to be unstable when an infinitely small variation of the present state of the flow brings it to a different state in a finite time. In the XIXth century, thanks to the work of Helmholtz, Kelvin, Rayleigh and Reynolds the fundamental problems of hydrodynamic instabilities were formulated.

An important part of this thesis concerns the experimental study of the stability of an stationary Saffman–Taylor finger in a Hele–Shaw cell [Hele–Shaw 1898], subjected to perturbations. This study is included in the more general problem of pattern formation of interfaces: dendrite formation in directional solidification, fracture shape... [Pelcé 88]

We want to explore the effect of disordered media on unstable interfaces, which has not been much explored [Decker 99]. On the contrary, the growth of interfaces in disordered media has been studied extensively in the case of rough, macroscopically stable interfaces both experimentally and theoretically [Alava 04].

Our study is related to side branching in the problem of crystal growth. When an undercooled melt solidifies, the solid front has a parabolic shape and lateral protrusions called side branches. These ones grow in amplitude as they are advected away from the parabolic tip. This phenomenon has been widely investigated in solidification, both experimentally [Dougherty 87] and theoretically [Pieters86], with the

conclusion that side branching results from selective amplification of natural noise.

Also, we want to study the effect of a time–dependent perturbation of the stationary Saffman–Taylor finger. The aim of studying frequency dependent flows of fluids in confined media is that they can be found in a wide variety of fields. Oscillatory flows have been proposed for reducing wetting layers of viscoelastic fluids, and also for the treatment of ground water aquifers contaminated by organic liquids, using elastic waves [Lambert 04]. Oscillatory flows are also present in the circulatory and breathing system of living creatures [Aarts 98], where it has been suggested that the pumping frequency of blood is selected to provide maximum power [Lambert 04]. Many of these systems imply the presence of more than one fluid. In order to have a basic understanding of many phenomena observed in frequency-dependent situations of two-fluid flow in confined media it is necessary to take a simple model system. Due to its relative simplicity, the Saffman-Taylor finger is an archetype of two-phase flow in confined media [Pelcé 88; McCloud 95; Couder 00].

Some of the problems which motivate the study of a frequency–dependent perturbation to a flow deal with complex fluids. The study of complex fluids has a great interest given that complex fluids can be found almost everywhere [Larson 99] and often present a a phenomenology much different than the one observed for Newtonian fluids. Time–dependent viscoelastic flows are expected to present interesting dynamical phenomena resulting from the interaction between the characteristic relaxation time scales of the viscoelastic fluid and the time scale of a parametric forcing. Hydrodynamic stability may be strongly affected by the complex rheology of non–Newtonian fluids, giving rise to new instabilities which are currently being subjected to experimental and theoretical analysis [Morozov 05; Groisman 00; Berret 97].

In the second part of this thesis we present a detailed experimental study of the oscillatory flow of a complex fluid. We show that the structure of the flow in the laminar regime is strongly affected by the viscoelastic properties of the fluid. And that, as a result, the flow becomes unstable even at low Reynolds numbers.

The thesis comprises experimental studies of interfacial instabilities of Newtonian fluids and of bulk instabilities of non–Newtonian fluids. This required the learning of different experimental techniques which will result in an excellent experimental background for future studies.

The thesis is organized as follows:

The first part of the thesis presents an introduction to Saffman–Taylor instability and to the current status of experiments regarding the stability of perturbed and non perturbed Saffman–Taylor fingers (Ch. 2), a description of Newtonian and non–

Newtonian fluids and a brief explanation of the phenomenology observed in complex flows (Ch. 3). Chapters 4, 5, 6, 7, and 8 are dedicated to the description of the experiments performed in the Hele–Shaw cell. The experimental characterization of an oscillating viscoelastic flow is presented in Chapters 9, 10, 11, 12, and 13.

Chapter 2

Saffman–Taylor instability

Since it was first observed by Saffman and Taylor in 1958 [Saffman 58], many authors have studied viscous fingering instability both theoretically and experimentally. For a review see [Pelcé 88; Couder 00; Bensimon 86-b]. The interest on this problem was first motivated by the oil recovery industry, but later the instability attracted the attention of physicists interested in pattern formation. The experimental device required to study the instability is relatively easy to implement. On the other hand, although Saffman–Taylor instability is a highly non–linear, non local problem it is still simple enough to allow some analytical research.

Saffman–Taylor instability is a viscosity driven instability that occurs at the interface between two fluids. When the less viscous fluid displaces the most viscous one, the interface is destabilized giving rise to the formation of viscous fingers ([Pelcé 88; Bensimon 86-b; Couder 00] and references therein).

In this chapter we will introduce the Hele–Shaw cell and characterize the flow in this almost-two dimensional medium. The mechanism which leads to the destabilization of a fluid–air interface in this kind of geometry will also be reviewed, as well as the stationary viscous finger. We will finish by describing some examples of viscous fingering subjected to perturbations.

2.1 Hele–Shaw Cell

A Hele–Shaw cell is a simple system in which the flow of a viscous fluid is potential and it is governed by Darcy's law, as in real porous media. The cell is formed by two glass plates separated by a gap spacing b which is much shorter than any other length scale of the system (Fig. 2.1). For conditions where inertia can be neglected ($\mathrm{Re} \ll 1$) the flow can be considered quasistationary. Due to the small gap spacing, v_z can be

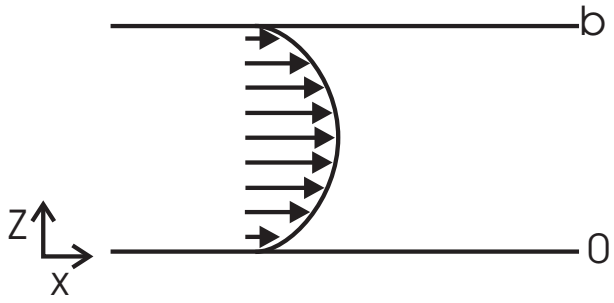

Figure 2.1: Poiseuille velocity profile developed in a Hele–Shaw cell.

safely neglected and the pressure gradient ∇p [1] can be considered independent of z. The no–slip boundary condition at the glass plates ($z = 0, b$) causes that the components of the velocity in the plane of the cell (x–y plane) change smoothly with respect to variations in the vertical direction. Considering a pressure gradient in the longitudinal (x) direction, the equation of motion reads:

$$\eta \frac{\partial^2 v_x}{\partial z^2} = \frac{dp}{dx}, \tag{2.1}$$

where η is the dynamic viscosity of the fluid which fills the cell.

The velocity profile (Fig. 2.1) obtained when this equation is solved with the no slip boundary condition ($v_x(z = 0) = v_x(z = b) = 0$) reads:

$$v_x(z) = \frac{1}{2\eta} \frac{dp}{dx} z\,(z - b)\,. \tag{2.2}$$

The depth–averaged x–component of the velocity is:

$$\langle v_x \rangle = \frac{1}{b} \int_0^b v_x dz = -\frac{b^2}{12\eta} \frac{dp}{dx}. \tag{2.3}$$

This expression of the mean velocity is the expression of Darcy's law (derived phenomenologically by Darcy in 1856 [Darcy 1856]) in the Hele–Shaw geometry. Considering that the flow is nearly two dimensional, this z-averaged velocity can be safely equated to the local velocity at each point of the cell.

Due to the simplicity of the experimental device required and the 2-dimensional nature of the flow developed, the Hele–Shaw geometry is used to study several phenomena. Besides viscous fingering the Hele–Shaw cell is also used to study interface growth in disordered media [Soriano 05], two–dimensional Kelvin–Helmholtz instability [Gondret 97], two–dimensional bubbles [Tanveer 87; Kopf–Sill 88-b], etc.

[1] The effect of gravity is taken into account by considering the pressure field $p' = p + \rho \mathbf{g} \cdot \mathbf{r}$.

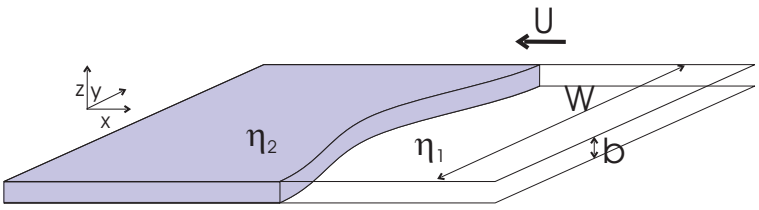

Figure 2.2: Scheme of a linear Hele–Shaw cell filled with two fluids of viscosities η_1 and η_2. The interface between both fluids becomes unstable when the less viscous fluid is pushing the more viscous one.

2.2 Saffman–Taylor instability in a linear horizontal channel

We will consider a linear horizontal channel[2] (Fig. 2.2) filled with fluids 1 and 2 ($\eta_1 < \eta_2$). When the less viscous fluid is displacing the more viscous one, the interface between both fluids is destabilized, giving rise to a viscous fingering instability.

The equation of motion in the channel has been already presented. The velocity of each viscous fluid in the cell is described by Darcy's law (Eq. (2.3)). Assuming that both fluids are incompressible ($\nabla \cdot \mathbf{v} = 0$), we can write down Laplace's equation:

$$\nabla^2 p_i = 0, \tag{2.4}$$

for each fluid ($i = 1, 2$). From now on, we will consider that the less viscous fluid is air ($\eta_1 \simeq 0$).

In order to have a complete description of the system, two boundary conditions are required. The first one is a kinematic condition that, given that the fluids are immiscible, at the interface $\mathbf{v_1} \cdot \mathbf{n} = \mathbf{v_2} \cdot \mathbf{n} \equiv \mathbf{U} \cdot \mathbf{n}$. The other condition is a dynamical condition for the pressure jump across the interface (Young–Laplace's law):

$$\delta p = \sigma\kappa = \sigma \left(\frac{1}{r_\parallel} + \frac{1}{r_\perp} \right), \tag{2.5}$$

where σ is the surface tension between the two fluids, $1/r_\parallel$ is the curvature of the interface in the x–y plane of the cell and $1/r_\perp$ is the curvature of the interface in the z direction.

Although the formulation of the Saffman–Taylor problem seems quite simple, its resolution is very complex due to the boundary conditions at the interface, which are continuously changing with the evolution of the system (moving boundary problem).

[2] In this particular configuration density contrast plays no role in the interface destabilization.

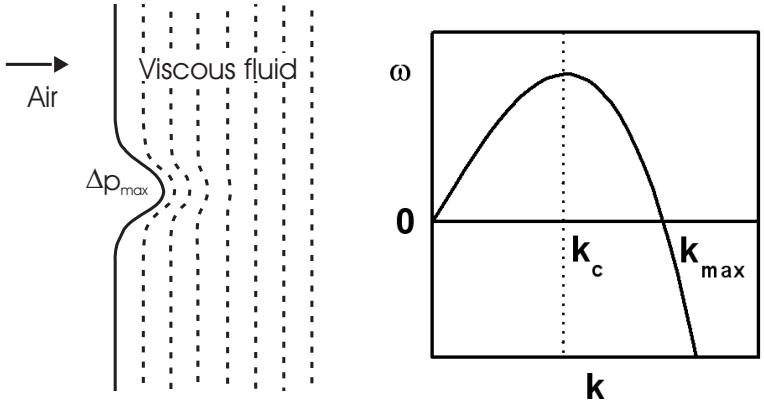

Figure 2.3: Left: Deformation of the isobaric lines due to a perturbation of the air-fluid interface for air pushing a viscous fluid. The pressure field in the viscous fluid is laplacian. The pressure field in air is constant, because $\eta_{air} = 0$. **Right:** Linear dispersion relation, giving the growth rate of an small perturbation to an air–viscous fluid interface as a function of the wavenumber of the perturbation, according to Eq. (2.6).

2.2.1 Linear stability analysis

The earlier stages of this instability can be understood studying the stability of a flat interface ζ between fluids 1 and 2 moving at a constant velocity U. When a perturbation is applied to the flat interface the competition between two mechanisms determines the decay or growth of the perturbation. The stabilizing mechanism is surface tension, which tends to smooth the interface, while the destabilizing mechanism is viscosity contrast.

Fig. 2.3 can help to understand this destabilizing mechanism. Given that the viscosity in the air is considered null, the pressure field in air is constant, while for the viscous fluid depends only on the distance to the free interface. Thus, the isobaric lines are parallel to the interface. When the interface is perturbed, air displaces the viscous fluid and isobaric lines are deformed (Fig. 2.3). As a consequence, the pressure gradient in the perturbed region increases. The increase of the pressure gradient causes an increase of the velocity in the perturbed region (Eq. (2.3)), which causes the local pressure gradient to increase further and further. On the contrary, when the more viscous fluid pushes the less viscous one, the deformation of the isobaric lines causes the pressure gradient to decrease. This slows down the interface and the perturbation decays.

The growth (or decay) rate of a perturbation of the interface can be evaluated for an small perturbation $\delta\zeta$ of the interface ζ, with small amplitude ϵ and wavenumber k. The perturbation of the interface $\delta\zeta = \epsilon e^{iky+\omega t}$ has growth rate ω. By solving

the equations of motion (2.4), considering the boundary conditions of continuity of the normal velocity across the interface and pressure jump, we obtain the following linear dispersion relation (Fig. 2.3):

$$\omega = U|k|\left(1 - \frac{b^2}{12Ca}k^2\right), \tag{2.6}$$

where $\mathrm{Ca} = U\eta/\sigma$ is the capillary number, which compares the relative magnitude of viscous forces to surface tension. At small k (long wavelengths) the destabilizing effect of the interface displacement is dominant, while the stabilizing effect of the surface tension is more important at large k. This stabilizing effect allows only the growth of modes with k in the range $(0, k_{max} = \sqrt{12\mathrm{Ca}/b^2})$, being the most unstable mode $k_c = k_{max}/\sqrt{3}$.

The most unstable wavelength of the system defines a length scale called the capillary length of the system:

$$l_c = \frac{\pi b}{\sqrt{\mathrm{Ca}}}. \tag{2.7}$$

This length scale allows us to determine wether a front will be stable or unstable to small perturbations. For a channel of width W the largest allowed wavelength is $\lambda = W$. As a consequence, if the smallest unstable wavelength is greater than the channel width the interface would be linearly stable. In terms of the capillary number, one obtains that the flat interface is unstable for values of the modified capillary number $1/B$ [Tabeling 87]:

$$\frac{1}{B} = 12\left(\frac{W}{b}\right)^2 \mathrm{Ca} > (2\pi)^2. \tag{2.8}$$

The modified capillary number compares the cell width with the capillary length. This parameter can also be understood as the inverse of a dimensionless surface tension B. At large values of this dimensionless surface tension the interface is linearly stable, while at small B surface tension is not able to suppress the perturbation and the instability develops.

2.2.2 The stationary Saffman–Taylor finger

Once the interface has destabilized, several fingers develop. The linear stability analysis allows us to predict the growth rate of each mode at the earliest stages of the instability but, quickly after the finger has formed, this analysis becomes invalid. When a set of fingers is formed at the earliest stages of the instability (Fig. 2.4)

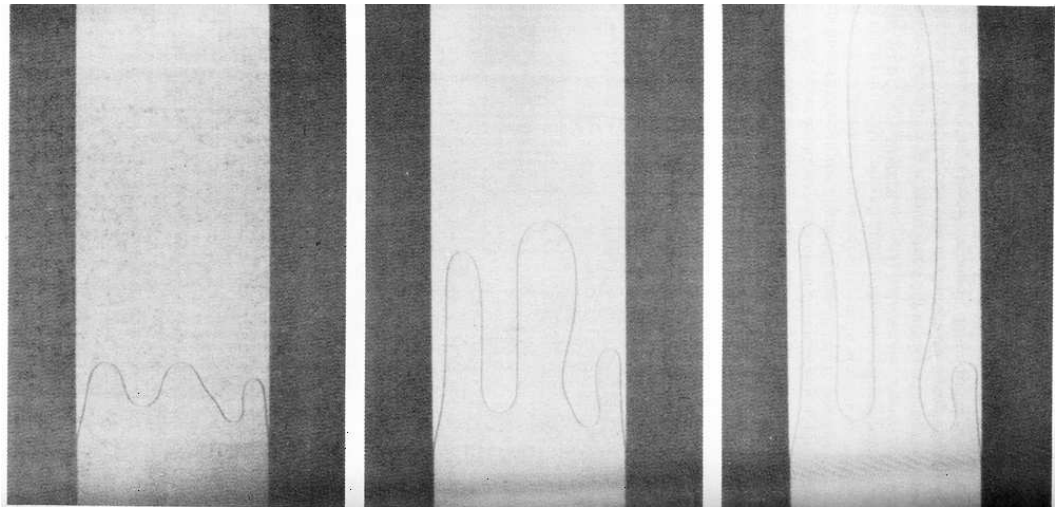

Figure 2.4: Evolution of the interface as a function of time for air penetrating oil. From [Tabeling 87].

they compete with each other until a single finger survives and propagates through the center of the cell. This finger is characterized by its width w, which is usually measured in channel width units: $\lambda = w/W$ (Fig. 2.5). The only parameter that determines this width is $1/B$ [Tabeling 87], as can be seen in Fig. 2.6. At low $1/B$, when surface tension is important, the finger tends to fill most of the channel. As $1/B$ is increased, viscous forces are more important and finger width decreases until it stabilizes at a constant value $\lambda = 0.5$ at high $1/B$.

The relative width of the finger also determines the shape of the finger tip. The shape of Saffman–Taylor fingers was first calculated by Saffman and Taylor [Saffman 58] without surface tension. They found a family of exact uniparametric solutions with a characteristic shape given by (see Fig. 2.7):

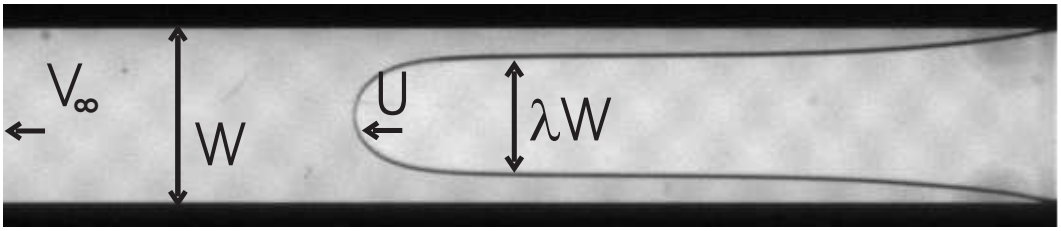

Figure 2.5: Notation used for important parameters: velocity of the flow far from the finger tip V_∞, finger tip velocity U, cell width W, finger width λW.

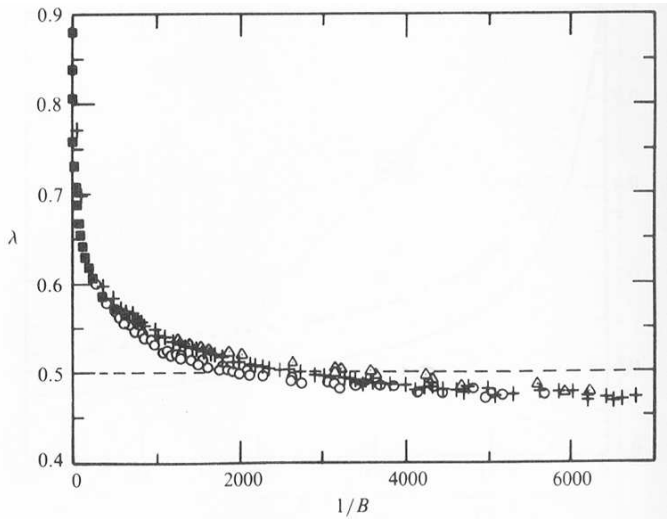

Figure 2.6: Relative finger width as a function of modified capillary number. From [Tabeling 87].

$$x = \frac{(1-\lambda)}{\pi} \ln \frac{1}{2} \left[1 + \cos \frac{\pi y}{\lambda} \right]. \tag{2.9}$$

At high velocities (low surface tension) this equation describes accurately the shape of the stationary fingers, whereas at low velocities there is a large mismatch between predicted and measured finger profiles (Fig. 2.8). These fingers are slightly better fitted by a relation found by Pitts [Pitts 80].

Since the air finger leaves a wetting layer behind [Tabeling 87], it actually fills only a fraction of the total gap spacing. The disagreement between theoretical predictions and experimental results may be explained at low $1/B$ by the presence of this wetting layer [Tabeling 86].

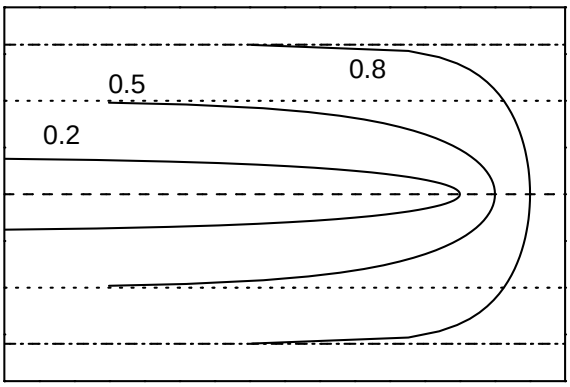

Figure 2.7: Shape of fingers with different widths calculated using Eq. (2.9) [Saffman 58].

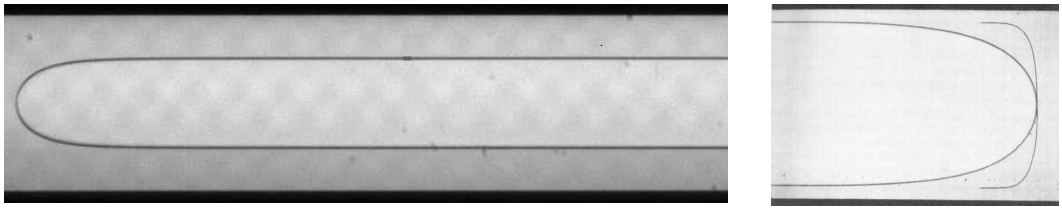

Figure 2.8: Left: Air penetrating silicone oil at high velocity. **Right:** Water penetrating oil at low velocity. From [Saffman 58].

2.3 Instabilities in non–perturbed Saffman–Taylor fingers

Theoretical and numerical studies on the stability of Saffman–Taylor fingers in the presence of surface tension have found the fingers linearly stable to eventual noise present in the system [Bensimon 86] for high $1/B$. The amplitude of the perturbation necessary to destabilize the finger decreases at increasing $1/B$. The experiments find the finger to be unstable in this same limit [Park 85; Lajeunesse 00].

A tip–splitting instability has been observed in Saffman–Taylor fingers in linear channels [Park 85; Kopf–Sill 88]. The experiments were performed in cells with an aspect ratio much higher than the one used by Saffman and Taylor in their original setup [Saffman 58], allowing the authors to achieve large modified capillary numbers at moderate Ca.

Experiments in long cells (Fig. 2.10) performed by Moore *et al.* [Moore 02] showed that long fingers in cells with high aspect ratio W/b presented a lateral instability. They observed that the amplitude of the lateral instability decayed at increasing Ca with a power law $\sim \mathrm{Ca}^{-2/3}$. Inhomogeneities in the gap spacing were measured and resulted to be very small (below 1% in all channels). The authors discarded inhomogeneities in the cell spacing and proposed long time relaxations of the interface in the back of the channel to be responsible for this lateral instability.

2.4 Perturbation of Saffman–Taylor fingers

As the fingers were demonstrated to be nonlinearly unstable to eventual perturbations [Bensimon 86], several authors have added controlled perturbations to the ideal system in order to determine the effect of such perturbations in the dynamics of the system. For a review, see [McCloud 95]. In particular, several studies focused in the addition of anisotropy to the isotropic cell. Li *et al.* predicted the formation of

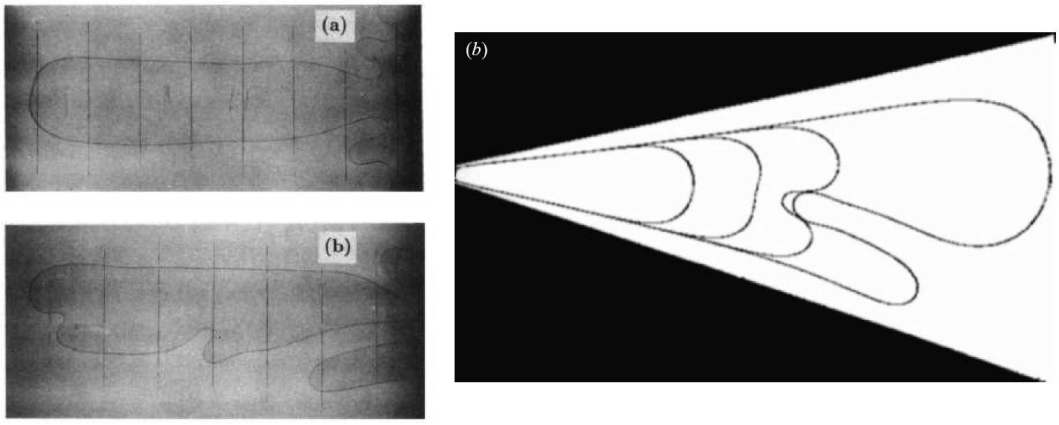

Figure 2.9: Left: Fingers of nitrogen penetrating heavy paraffin oil with a positive gap gradient. The upper photography corresponds to a low velocity and the one at the bottom to a high velocity. From [Zhao 92]. **Right:** Superposition of four fingers of air penetrating into oil in a wedge with angle 30°. From [Lajeunesse 00].

side–branching in perturbed fingers [Li 86]. Some examples of the mechanisms used to create an anisotropy in the cell and the effect observed in the fingers are:

- **Gradient in gap spacing.** When the gap spacing between the plates of the Hele–Shaw cell is not uniform, both the equations of motion and boundary conditions are different from those in the parallel plate system. In Ref. [Zhao 92], an uniform gap gradient is applied to the cell. For positive gap gradients (Fig. 2.9) the finger tip is flatter and more unstable than for the constat gap configuration, whereas for negative gap gradients the tip is sharper and more stable.

- **Sector–shaped cells.** When a variation in the cell width is imposed in the cell, translational invariance is lost and stationary fingers cannot be formed [Thomé 89]. The observed pattern is a single finger travelling trough the center of the channel (Fig. 2.9). These fingers are unstable for lower $1/B$ than in the channel geometry. The minimum value for which the fingers are unstable decreases as the angle of the cell increases [Lajeunesse 00].

- **Wires, wedges and bubbles: Anomalous Saffman–Taylor fingers.**

  The family of solutions obtained by Saffman and Taylor [Saffman 58] without surface tension (Eq. (2.9)) allows values of the finger width $0 < \lambda < 1$, but fingers with $\lambda < 0.5$ are not observed in experiments. Later, calculations of the finger shape taking into account surface tension showed that selection of solutions with $\lambda < 0.5$ with non zero surface tension presented a cusp–like

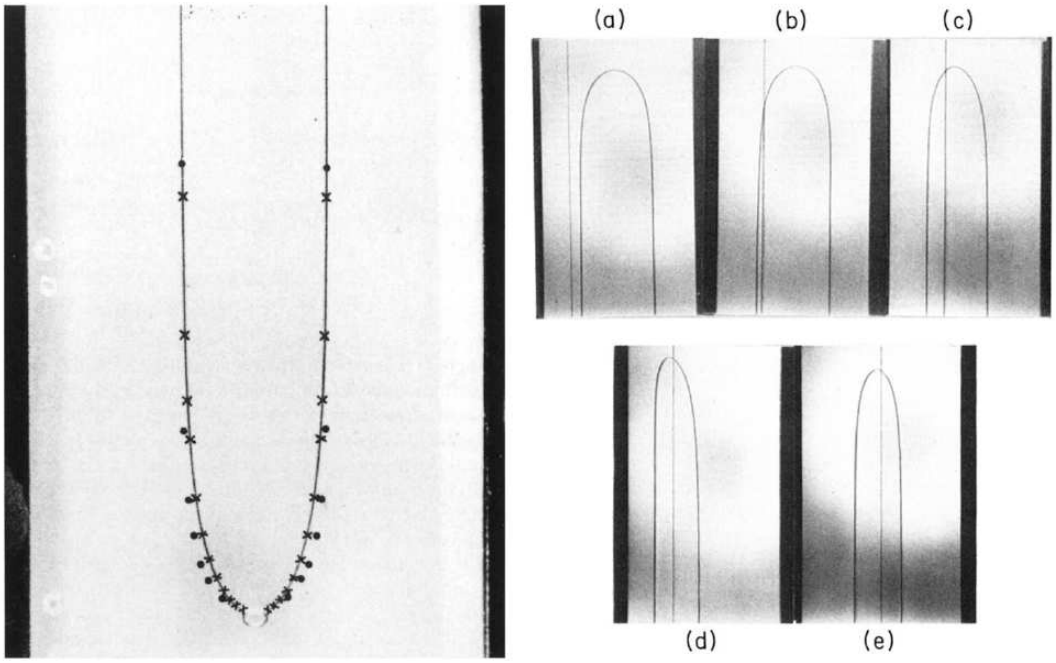

Figure 2.10: Left: Finger of nitrogen penetrating oil, perturbed by a bubble. The crosses are points of the theoretical profile (2.9) from Saffman–Taylor for $\lambda = 1/2$ and the dots are calculated from Pitt's relation [Pitts 80] for $\lambda = 0.32$. From [Couder 86]. **Right:** Steady states of air penetrating oil with a wire inside the channel. From [Zocchi 87].

singularity at the tip. It was also predicted that an anisotropic surface tension in Saffman–Taylor fingers can suppress this singularity to allow narrow fingers [Dorsey 87].

These fingers have been observed experimentally in anisotropic cells [Couder 86; Zocchi 87; Rabaud 88]. Fingers perturbed with bubbles at the tip narrowed [Couder 86] (Fig. 2.10) as well as fingers in cells with two grooves at the center [Rabaud 88]. Fingers perturbed with a thread narrowed only if the thread intersected the interface near the finger tip [Zocchi 87; Rabaud 88] (Fig. 2.10). All the fingers were found to be stable to $1/B$ higher than the unperturbed ones. The destabilization observed at high $1/B$ was characterized by the formation of lateral undulations.

- **Periodic perturbations.**

  In Ref. [Gland 03], the stability of the the fluid–air interface in a circular Hele–Shaw cell was increased by periodic modulations of the pressure–air injection.

2.5 Viscous fingering in complex fluids

Currently an important part of the studies of viscous fingering are centered in complex fluids, as the competition between viscous and capillary forces is affected by fluid rheological properties.

For instance, when the displaced fluid exhibits shear–thinning the fingers are predicted to sharpen with $\lambda \to 0$ as $1/B$ increases [Corvera–Poiré 98; Ben Amar 99]. The sharpening of viscous fingers in shear–thinning fluids has been experimentally verified [Lindner 00b; Lindner 00c] for strong shear thinning fluids, whereas for weak shear–thinning fluids the results collapse in the universal curve for Newtonian fluids. Some air fingers displacing polymeric solutions exhibiting extreme shear–thinning [Vlad 99] develop a velocity–jump instability when driven at high velocities.

The behavior of viscous fingering in elastic fluids is completely different [Lindner 00; Bonn 97]. The finger width plateau reached at high velocities is significantly higher than the classical limit 0.5 even for elastic fluids exhibiting shear–thinning [Bonn 95]. The authors conclude that normal stresses (not present in non elastic fluids) are responsible for the widening of the fingers. Widening of the fingers was also observed in surfactant solutions [Bonn 95]. The widening mechanism proposed is the presence of surfactant molecules in the interface, which induces a dynamic surface tension at the tip of the finger increasing at increasing values of the velocity.

Periodic forcing in complex viscous fingering has been studied theoretically in linear channels [Corvera–Poiré 04], predicting resonant effects at frequencies fixed by cell geometry and fluid properties. Folch *et al.* [Folch 01] showed experimentally and theoretically that the periodic forcing of fingers of a nematic liquid crystal in a radial Hele–Shaw cell induced lateral waves to the fingers, as a result of the acceleration and deceleration of the tip of the fingers.

Chapter 3

Complex fluids

The term complex fluid is used to define different classes of materials which behave as a fluid (continuously deform under an applied stress) but do not present the behavior of a Newtonian fluid. In Fig. 3.1, this idea is made clear: for a Newtonian fluid (water, oil) there is a linear relation between the applied stress and the deformation rate. In the same figure some non–Newtonian responses are displayed. For instance, shear thinning fluids flow easier at high shear stresses. Polymeric solutions of long chains are good examples of shear thinning materials. There are a few materials which present the opposite behavior, and are called shear–thickening materials. Finally, materials presenting yield stress do not flow for applied stresses below a threshold value. There are also materials which have a behavior between that of a Newtonian fluid (dissipative) and that of an elastic solid. These fluids are called viscoelastic. Some materials can also present more than one non–Newtonian property at the same time. A thorough review on the topic can be found in Refs. [Larson 99; Bird 87; Gelbart 96].

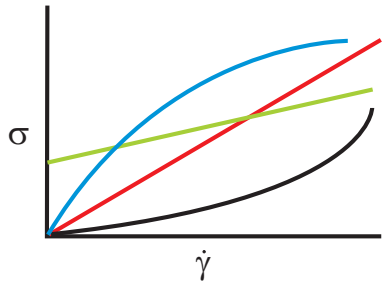

Figure 3.1: Scheme of the different responses to an applied stress: Newtonian (red), pseudo-plastic or shear–thinning (blue), dilatant or shear–thickening (black), yield–stress (green). σ is the applied shear stress and $\dot{\gamma}$ is the resulting shear strain rate.

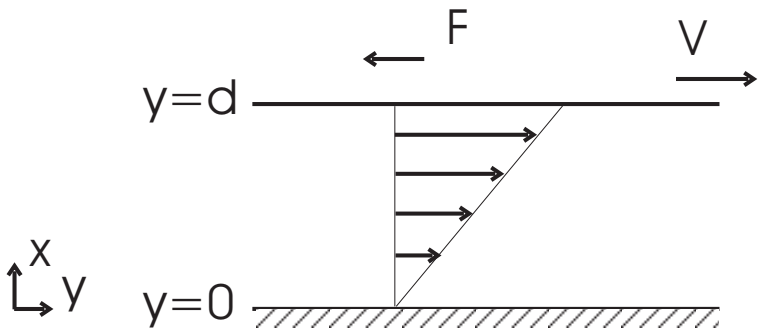

Figure 3.2: Geometry of a simple shear experiment.

In this chapter, the main properties of Newtonian fluids are reviewed and compared to some complex materials. A particular kind of viscoelastic fluid, a surfactant micellar solution, is also described. Finally, several phenomena observed in the flow of complex fluids are enumerated.

3.1 Newtonian fluids

Hydrodynamics of Newtonian fluids have been studied long time ago [Batchelor 90; Guyon 94]. The main property of these simple fluids (water, oil, glycerol) is that they continuously deform (flow) under an arbitrary shear stress. The internal resistance of the fluid to deform is characterized by the viscosity of the fluid, which can be understood by means of a simple shear flow experiment [Guyon 94].

An sketch of the experiment is shown in Fig. 3.2. A fluid is confined by two horizontal parallel plates separated a distance d. The upper plate is displaced at a constant velocity V, while the plate at the bottom remains at rest. At the stationary regime, the observed velocity profile changes linearly from $v_x(y = 0) = 0$ to $v_x(y = d) = V$. The friction force per unit area opposed to the relative motion of two fluid layers is proportional to the variation of velocity between adjacent layers:

$$\frac{F}{S} = -\eta \frac{\partial v_x}{\partial y}. \tag{3.1}$$

η is the viscosity, a constant which is a material property. We have also introduced the stress $F/S \equiv \pi$ which has pressure units and is an expression of the internal motions and interactions of the fluid. Eq. (3.1) is Newton's law for viscosity and has been experimentally verified for many simple fluids.

The stress introduced in Eq. (3.1) is in general a tensor. It measures the internal distribution of forces per unit area acting across a surface. For a given surface, the

stresses can be divided into normal stresses and shear stresses. Shear or tangential stresses measure the friction forces between adjacent fluid layers and are equal to zero for a fluid at rest. Normal stresses in a Newtonian fluid are isotropic and are equal to the hydrostatic pressure. The stress tensor can be separated in two contributions:

$$\pi = p\delta + \tau, \tag{3.2}$$

where τ is associated with the viscosity of the fluid and will be called the stress tensor[1]. An equation which assigns a value to the stress tensor is a constitutive equation. The constitutive equation for a Newtonian incompressible fluid is a generalization of Eq. (3.1):

$$\tau = -\eta\dot{\gamma}, \tag{3.3}$$

where $\dot{\gamma}$ is the rate of strain tensor, defined as $\dot{\gamma}_{ij} = \frac{1}{2}(\partial v_i/\partial x_j + \partial v_j/\partial x_i)$.

For a simple shear experiment defined by:

$$v_x = \dot{\gamma}, \quad v_y = 0 \quad v_z = 0, \tag{3.4}$$

the stress tensor has the following form:

$$\tau = \begin{pmatrix} 0 & -\eta\dot{\gamma} & 0 \\ -\eta\dot{\gamma} & 0 & 0 \\ 0 & 0 & 0 \end{pmatrix} \tag{3.5}$$

and the total stress tensor is expressed by:

$$\pi = p\delta + \tau = \begin{pmatrix} p & -\eta\dot{\gamma} & 0 \\ -\eta\dot{\gamma} & p & 0 \\ 0 & 0 & p \end{pmatrix} \tag{3.6}$$

3.2 Viscoelastic fluids

A fluid is called viscoelastic when it presents both elastic and viscous properties. This behavior is due to the molecular composition of the fluid. In general viscoelastic fluids are formed by very large elastic molecules with long relaxation processes. These relaxation processes affect the macroscopic dynamics of the fluid, leading to a phenomenology which can be dramatically different from the one of a Newtonian fluid.

There are two important dimensionless parameters measuring the importance of elasticity in viscoelastic flows: the Deborah and the Weissenberg number. The

[1]From now on, π will be called the total stress tensor

Deborah number compares the magnitude of elastic forces and viscous forces. It is defined as the ratio of two characteristic times:

$$\mathrm{De} = \frac{t_e}{t_{flow}}, \tag{3.7}$$

where t_e is usually the largest characteristic time of the fluid and t_{flow} is a characteristic flow time. When $\mathrm{De} \to 0$, viscous forces are very important compared to elastic ones and the viscoelastic fluid will behave as a Newtonian one. The limit $\mathrm{De} \to \infty$ implies that the elastic forces are dominant and the fluid will behave as a Hookean solid.

The Weissenberg number is a dimensionless shear rate defined as:

$$\mathrm{Wi} = t_e \dot{\gamma}_c. \tag{3.8}$$

The inverse of the shear rate $\dot{\gamma}_c$ is a characteristic time scale for the local deformation of a fluid element. When Wi becomes large, elastic stresses become important.

For most viscoelastic materials, it is not possible to obtain a single constitutive equation describing an arbitrary flow. In order to obtain an expression of the stresses it is necessary to define simple flows. For instance, the stress tensor for a simple shear flow (Eq. (3.4)) can be generalized for a viscoelastic fluid. Due to the symmetry of the stress tensor, there are only six components of the stress tensor to be determined. The number of independent components can be further reduced if we consider that the stress must be invariant under rotations around the z–axis. Thus, the most general expression for the stress tensor is:

$$\pi = p\delta + \tau = \begin{pmatrix} p + \tau_{xx} & \tau_{yx} & 0 \\ \tau_{xy} & p + \tau_{yy} & 0 \\ 0 & 0 & p + \tau_{zz} \end{pmatrix}. \tag{3.9}$$

For incompressible flows, the quantities experimentally accessible are:
Shear stress: τ_{yx},
First normal stress difference: $\tau_{xx} - \tau_{yy}$,
Second normal stress difference: $\tau_{yy} - \tau_{zz}$.

While in a Newtonian fluid normal stress differences are null, for a non–Newtonian fluid they can be very large. The first normal stress difference is in general negative.This means that the viscoelastic fluid is subjected to an extra volume force perpendicular to the streamlines. This extra volume force is responsible for interesting phenomena observed in viscoelastic flows (elastic instabilities, rod climbing)that

will be briefly discussed in Sec. 3.3. The second normal stress difference is in general much smaller than the first normal stress difference.

The shear stress τ_{yx} is showing the viscous behavior of the fluid. The viscosity of a viscoelastic fluid is defined by analogy with Newton's law, Eq. (3.3):

$$\eta(\dot{\gamma}) \equiv \frac{\tau_{yx}}{\dot{\gamma}}. \tag{3.10}$$

3.2.1 Generalized Newtonian fluids

This term is used to define fluids which are purely viscous but have a non constant viscosity. The constitutive equation for these fluids is the same than for Newtonian ones (Eq. (3.10)), where $\eta = \eta(\dot{\gamma})$, and they do not present normal stress differences. Most generalized Newtonian fluids present shear–thinning response. This means that they flow easier at increasing shear rates. Solutions of rigid polymers are a good example of shear–thinning fluids. The initial isotropic configuration is modified by the shear, which induces the alignment of the molecules with the direction of the shear. This results in a decrease of the effective viscosity.

There are several phenomenological models which try to reproduce the decrease in viscosity at increasing shear rates [Carreau 97; Bird 87]. The most simple of them assigns a power–law relation between effective viscosity and shear rate:

$$\eta = \eta_0 \dot{\gamma}^{-m}. \tag{3.11}$$

3.2.2 Maxwell fluids. Living Polymers

In this section we will study a family of viscoelastic solutions which behave as a Maxwell fluid. The Maxwell linear model is the simplest model that includes both elastic and viscous effects[2]. The fluid is described by the constitutive equation:

$$\tau + t_m \frac{\partial \tau}{\partial t} = -\eta \dot{\gamma}. \tag{3.12}$$

This is the constitutive equation for a Newtonian fluid plus a memory term. t_m is the characteristic Maxwell time and defines a characteristic time scale: for times shorter than t_m elastic behavior is dominant, whereas for times longer than t_m viscous behavior is dominant.

Despite its high level of simplicity, the Maxwell model describes very accurately the behavior of some viscoelastic fluids, in a range of low shear rates. The most

[2]The rheology of a Maxwell fluid is described in Appendix A.

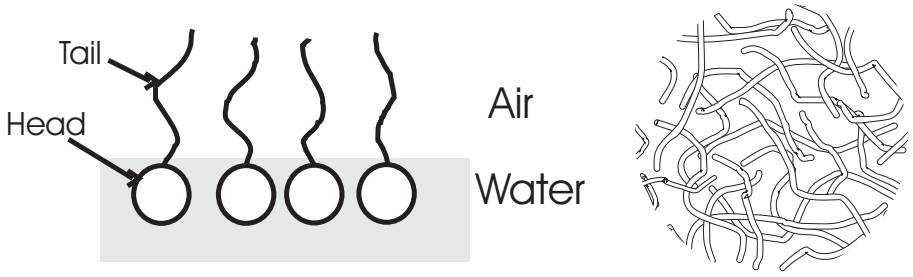

Figure 3.3: Left: Adsorption of surfactant molecules at an air–water interface. **Right:** Scheme of the entangled regime of cylindrical micelles.

common example of materials exhibiting this Maxwellian behavior are some concentrations of surfactant solutions [Rehage 88; Clausen 92; Berret 93; Fischer 97; Ali 97; Méndez-Sánchez 03a].

Surfactants are amphiphilic molecules [Larson 99; de Gennes 04]: they are formed by a hydrophilic (water loving) group bounded to a lyophilic (oil loving) group. The lyophilic group consists on a hydrocarbon chain which is called the "tail" of the molecule, whereas the hydrophilic part is usually shorter and bulky and it is called the "head" of the molecule. Depending on the net charge of the head of the molecule, surfactants can be classified into ionic or non–ionic.

Surfactant molecules are also called tensoactive. This is due to the behavior of the molecules when solved in water: the head will tend to maximize its contact with water while the tail will try to minimize it. As a result surfactant molecules accumulate at the air–water interface (Fig. 3.3) decreasing the surface tension between air and water. At increasing concentrations of surfactant the molecules assemble reversibly into aggregates (spherical or cylindrical micelles, vesicles and bilayers) or, at even higher concentrations, the surfactant can form ordered phases.

Maxwellian behavior is observed in the range of concentrations for which the molecules assemble into semi–flexible cylindrical micelles [Rehage 88], in the entangled regime (Fig. 3.3) where the behavior of the micelles is equivalent to flexible polymers (for length scales below the persistence length) [Cates 90].

Cates [Cates 87] proposed a model which would explain the viscoelastic behavior of micellar surfactant solutions in the entangled regime. The model considers an entangled regime of chains with an average length. These chains break and recombine with a typical breakage time τ_{break} which is inversely proportional to the average length of the chain. Each chain relaxes by reptation [de Gennes 79]: since it cannot cross the other chains, it changes its conformation by sliding back and forth with a characteristic time τ_{rep}. In the limit $\tau_{break} \ll \tau_{rep}$ the chain has broken and recom-

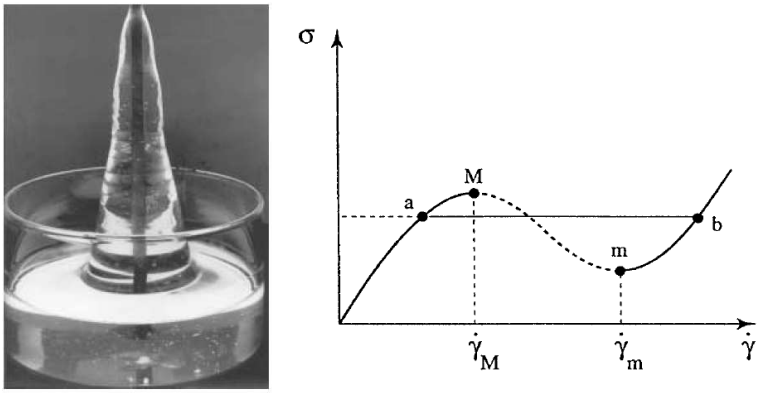

Figure 3.4: Left: Rod–climbing effect in a polymeric viscoelastic solution. From "http://www.mie.utoronto.ca/labs/rheology". **Right:** Schematic representation of a non-monotonic constitutive relation linking the stress and the shear rate. From [Berret 97].

bined many times before it has completed the reptation and the relaxation process is characterized by a single time scale τ defined as:

$$\tau = (\tau_{break}\tau_{rep})^{1/2} . \tag{3.13}$$

This time scale τ coincides with the characteristic Maxwell time t_m of the Maxwell linear model (Eq. (3.12)).

3.3 Phenomena in complex flows

There are many situations in which the flow developed for a complex fluid is completely different from the flow developed for a Newtonian one in the same conditions. This different behavior is rather characteristic of solutions containing macromolecules or large structures (micelles, for instance).

An interesting effect observed in many viscoelastic micellar solutions is shear banding [Berret 97; Britton 99; Lerouge 00; Méndez-Sánchez-03b]. It is observed in the nonlinear regime, at high shear rates. There is a band of shear rates for which the stress is multivalued (Fig. 3.4). An initially homogeneous flow is unstable and separates into two phases: one of them of low viscosity, supporting a high shear rate, and the other one of high viscosity, supporting a low shear rate. This mechanical instability is observed at long times ($t \geq \tau_m$). At short times the response is the one observed in the linear regime.

Other effects are purely due to the elasticity of the fluid. Consider for instance the Weissenberg or rod–climbing effect [Weissenberg 47]. The experiment is very

simple: when a rotating rod is inserted in a recipient containing a Newtonian fluid, the centrifugal force pushes the fluid outwards the rod. On the contrary, when the rotating rod is inserted into a recipient containing a viscoelastic fluid, the fluid moves toward the center and climbs the rod (Fig. 3.4). This phenomenon is due to the first normal stress difference, which creates a volume force in the direction of the curvature contrary to centrifugal and gravitational force .

3.3.1 Elastic instabilities

In this section, we will present a new destabilization mechanism which has been observed in viscoelastic flows in conditions for which Newtonian flows are laminar. We will refer to polymeric solutions, given that most of the studies on elastic instabilities have been performed for this kind of viscoelastic fluids.

The motion of a Newtonian (simple) fluid is governed by Navier–Stokes equations [Batchelor 90]. These equations include a non linear term which is due to inertia. Reynolds number is the dimensionless parameter which compares the importance of inertial forces to viscous dissipation:

$$\mathrm{Re} = \frac{|\mathbf{v} \cdot \nabla \mathbf{V}|}{|\nu \nabla^2 \mathbf{v}|} = \frac{LV}{\nu}, \tag{3.14}$$

where $\nu = \eta/\rho$ is the kinematic viscosity of the fluid (a diffusion coefficient of momentum), L is the characteristic length, and V is the characteristic velocity. This dimensionless number controls inertial instabilities: at high Reynolds number inertial effects are important and the flow may become turbulent. The Poiseuille pipe flow of a Newtonian fluid has been found to be linearly stable for all Re and nonlinearly unstable at $\mathrm{Re} > 10^3$ [Drazin 02].

In viscoelastic flows without inertia ($\mathrm{Re} \ll 1$) elastic stresses have been found able to induce an instability which, in some cases, can lead to a turbulent state [Groisman 00]. The origin of the instability comes from the constitutive equation describing the state of stress in flowing polymeric materials, which includes a nonlinear relation with the rate of deformation tensor $\dot{\gamma} = (\nabla \mathbf{v}) + (\nabla \mathbf{v}^\dagger)$. This complex relation plays a destabilizing role in the momentum equation in the absence of inertial terms. The importance of elastic to viscous forces is measured by the Weissenberg number $\mathrm{Wi} = \lambda \dot{\gamma}_c$ for a fluid characteristic time λ and a flow characteristic shear rate $\dot{\gamma}_c$ which is the inverse of the local deformation time scale.

The mechanism of the destabilization in flows with curved streamlines is well understood. As a matter of fact, the destabilizing mechanism is the same that creates rod–climbing. Normal stresses produced by the stretching of molecules of the

fluid create a pressure gradient in the direction of the curvature (hoop stress) which can destabilize the flow. There are several examples of elastic instabilities in flows with curved streamlines [Pakdel 96; Groisman 97; Groisman 98; Arora 02], whereas elastic turbulence has been thoroughly characterized by Groisman and Steinberg [Groisman 00; Groisman 04].

Although flows with straight streamlines are known to be linearly stable, recently it was shown that a finite amplitude perturbation of the straight streamlines can create a local curvature which would destabilize the flow at moderate values of the Weissenberg number [Meulenbroek 04; Morozov 05].

3.3.2 Dynamic permeability

As shown in this section, the differences in the behavior of a complex and a Newtonian fluid can be dramatic. In particular, a time–dependent viscoelastic flow may exhibit resonant behavior, while a Newtonian one responds monotonically.

A frequency dependent viscoelastic flow in a porous medium can be described by the dynamic permeability of the medium [Avellaneda 91; López de Haro 96] which relates the flow rate through a porous medium with the local pressure drop [del Río 98; Tsiklauri 01; Corvera–Poiré 04].

In this context, we will review the problem of the flow of a linearized Maxwell fluid in a tube [del Río 98; Tsiklauri 01] at vanishingly small Reynolds number. The tube is vertical and is considered to have infinite length (Fig. 3.5). The mean flow rate through the tube for a constant pressure drop (i.e. for $\omega = 0$) is the same for the Newtonian and Maxwell fluids and is given by Darcy's law. For a time–dependent pressure drop, the different constitutive equations of a Newtonian fluid (Eq. (3.3)) and a Maxwell fluid (Eq. (3.12)) play an important role in the flow.

The laminar flow of an incompressible fluid ($\nabla \cdot \mathbf{v} = 0$) is described by the linearized momentum equation:

$$\rho \frac{\partial \mathbf{v}}{\partial t} = -\nabla p - \nabla \cdot \tau, \tag{3.15}$$

when the inertial contribution is negligible ($\mathrm{Re} \ll 1$). For Maxwell and Newtonian fluids, the constitutive equations are known (Eqs. (3.12) and (3.3)) and can be combined with the linearized momentum equation to give a closed relation between velocity, pressure drop and fluid properties (density ρ, viscosity η, and Maxwell relaxation time t_m for the Maxwell fluid). In the range of parameters considered in the problem, the flow is strictly parallel to the axis of the tube and preserves axial symmetry. Thus, we can safely take $\mathbf{v} = v(r)\widehat{\mathbf{a}}_{\mathbf{z}}$. For both fluids the result is a linear differential

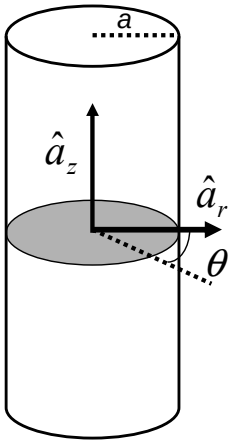

Figure 3.5: Scheme of the geometry defined in the linear model.

equation which can be Fourier transformed in time[3] to give:

$$\rho(\omega^2 t_m + i\omega)V + \eta\nabla^2 V = (1 - i\omega t_m)\nabla P, \tag{3.16}$$

for a Maxwell fluid[4].

This equation can be solved in cylindrical coordinates with no–slip condition at the walls (i.e. $V(a) = 0$, where a is the radius of the tube) [del Río 98]:

$$V = -\frac{(1 - i\omega t_m)}{\eta\beta^2}\left(1 - \frac{J_0(\beta r)}{J_0(\beta a)}\right)\frac{\partial P}{\partial z}, \tag{3.17}$$

$$\beta = \sqrt{\frac{\rho}{\eta t_m}\left((\omega t_m)^2 + i\omega t_m\right)}. \tag{3.18}$$

This rather complicated expression is actually a relation between the velocity of the fluid and the pressure drop. Both magnitudes are related by a function which depends on system geometry, fluid properties and frequency. Assuming that the pressure drop depends neither on the radius nor on the azimuthal position, the expression of the flow rate through a tube section is a generalization of Darcy's law:

$$\langle V\rangle_r = -\frac{K(a, \omega, \eta, \rho, t_m)}{\eta}\frac{\partial P}{\partial z}. \tag{3.19}$$

[3]The definition of Fourier transform used is: $F(r,\omega) = \frac{1}{2\pi}\int_0^\infty f(r,t)e^{i\omega t}dt$

[4]The solution for a Newtonian fluid can be recovered by carefully applying the limit $t_m \to 0$ in the equations for the Maxwell fluid.

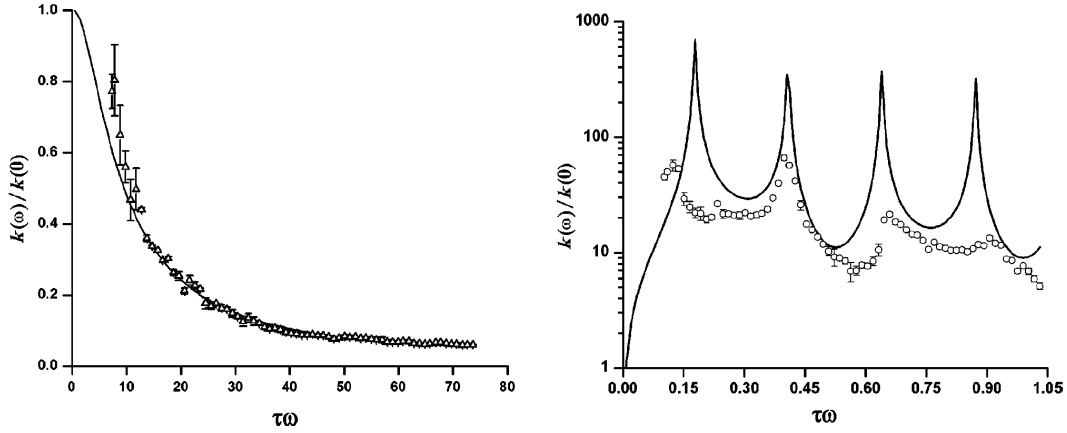

Figure 3.6: Open circles: Measurements at tube axis of the dimensionless dynamic response of a fluid to periodic forcing. Solid lines: theoretical prediction. The permeability is made dimensionless by comparison with $k(0) = -a^2/8$. **Left:** Measurements for a Newtonian fluid: glycerol. **Right:** Measurements for a Maxwellian fluid: CPyCl/NaSal 100/60 mM. Notice the different scales. Both from [Castrejón-Pita 03b].

Oscillatory pressure drop

An experimental measurement of the response function $K(\omega)$ was performed for the particular case of a periodic pressure drop of angular frequency ω and amplitude z_0 [Castrejón-Pita 03a; Castrejón-Pita 03b]. The pressure drop can be written as $\partial p/\partial z = -\rho z_0 \omega^2 e^{i\omega t}$, and relation (3.19) can be transformed to time domain:

$$v(r,t) = -i\omega z_0 \left(1 - \frac{J_0(\beta r)}{J_0(\beta a)}\right) e^{i\omega t}. \tag{3.20}$$

Fig. 3.6 shows an example of the different response functions of a Newtonian and a Maxwellian fluid. For a Newtonian fluid, the dynamic permeability decreases at increasing frequency whereas for the Maxwellian fluid there is a resonant behavior and the dynamic response for some of the frequencies exhibits peaks one order of magnitude higher than for the background.

Chapter 4

Lateral instabilities in Saffman–Taylor fingers: Background

Viscous fingers appear when an inviscid fluid displaces a viscous fluid in a Hele-Shaw cell [Hele–Shaw 1898], a pair of glass plates parallel to each other that form an almost two-dimensional channel in which the flow takes place. After a dynamic process of finger competition, a single-finger steady state is reached. This one is called Saffman-Taylor finger [Saffman 58]. In the absence of anisotropy Saffman-Taylor fingers are always greater than half of the channel width, and are called *normal* in order to differentiate them from narrow fingers obtained in the presence of anisotropy, called *anomalous* [Couder 86; Rabaud 88]. While lateral instabilities in anomalous fingers are known already for two decades, normal Saffman-Taylor fingers were considered for a long time to have stable flat sides. Recently, lateral fluctuations on normal Saffman-Taylor fingers have been reported for wide channels [Moore 02].

Later, a numerical study of the stability of normal Saffman-Taylor fingers subjected to small perturbation [Ledesma-Aguilar 05; Quevedo–Reyes 06] predicted the development of a lateral instability in viscous fingers subjected to small perturbations, comparable to the eventual noise present in experimental systems. These studies motivated our experiments in a long Hele-Shaw cell and are briefly reviewed next.

4.1 Numerical study of lateral instabilities in normal Saffman-Taylor fingers

The numerical studies presented in this section were developed by Ledesma–Aguilar *et al.* [Ledesma-Aguilar 05] and Quevedo–Reyes *et al.* [Quevedo–Reyes 06]. These authors report simulations of normal Saffman–Taylor fingers ($\lambda > 0.5$) in 2–d cells using a Phase-Field model modified in order to introduce one of the following destabilization mechanisms:

- Anisotropy in the cell [Quevedo–Reyes 06]. In a 3–d cell the anisotropy is in general obtained by creating a non constant gap spacing [Couder 86; Kopf–Sill 87; Rabaud 88; Zhao 92]. In a 2–d cell this can be done by the generation of an anisotropic permeability in the cell. Thus, the permeability of the cell was modified by choosing sites where the value of the permeability was different than in other sites of the cell. The changes in the mobility were chosen to be very small, in order to allow normal Saffman–Taylor fingers to develop.

- Dynamic boundary condition [Ledesma-Aguilar 05]. The constant pressure gradient was modified to allow for dynamic pressure drops. These pressure drops were chosen to be very small compared to the constant pressure gradient. The perturbation was applied to a fully developed stationary Saffman–Taylor finger.

The results for both destabilization mechanisms were closely related to two time scales characteristic of the steady problem. The finger characteristic frequency was defined as:

$$\nu_{finger} = \frac{U}{\lambda W}, \tag{4.1}$$

where W is the width of the channel, U the finger velocity, and λ the dimensionless finger width.

The other characteristic frequency was defined for the flow very far from the finger tip:

$$\nu_{\infty} = \frac{V_{\infty}}{W}, \tag{4.2}$$

where V_{∞} is the velocity of the flow very far from the finger tip.

The wavelength of the lateral instability Λ was measured as the distance between two adjacent maxima of the lateral instability. The corresponding frequency of the lateral instability was calculated as:

$$\nu = \frac{U}{\Lambda}, \tag{4.3}$$

4.2 Anisotropy in the cell

The anisotropy of the cell was designed to reproduce persistent anisotropy in the flow direction (a parabolic variation of the gap spacing or a distribution of stripes in the longitudinal direction of the cell) and variations in the gap spacing randomly distributed.

The instability generated by a parabolic profile was qualitatively equivalent to the one produced for a stripe profile in the flow direction (Fig. 4.1). For small variations in the permeability the fingers developed a periodic instability, whereas for high variations the instability was non periodic. The fingers generated where slightly but systematically out of center, as was also observed in Refs. [Couder 86; Rabaud 88].

In the range of parameters for which the developed instability was strictly periodic, small variations in the permeability of the cell produced a symmetric instability, whereas for higher variations the instability was asymmetric. The response frequency of the lateral instability increased monotonically with the magnitude of the variations in the permeability. For all the fingers studied the response frequency was between the characteristic frequencies of the flow, ν_∞ and ν_{fing}.

The instability observed for cells with a permeability randomly varying between two values (Fig. 4.1) was strictly non periodic. The observed instability had a low amplitude and was developed even for cells with extremely low variations in the permeability (as low as 10% of the total area of the cell presenting a permeability different in a 1% from the rest of the cell). The coverage of the cell was defined as the percentage of sites in the cell presenting a permeability different from the rest of the cell.

The disorder in the cell generated a wave close to the tip that destabilized the flat sides of the finger when travelling away from the tip. The instability grew and reached an almost constant amplitude far from the finger tip. Near the finger tip the anisotropy of the cell produced a perturbation of the finger tip with several modes. Far from the finger tip, some of those modes decayed and other grew. The frequency distribution of the lateral instability presented a well defined single peak at a frequency slightly higher than ν_∞.

A study of the dependence of these results with the properties of the disorder was performed by varying the coverage and the intensity of the disorder. The results showed that none of these two parameters had a quantifiable effect on the lateral instability.

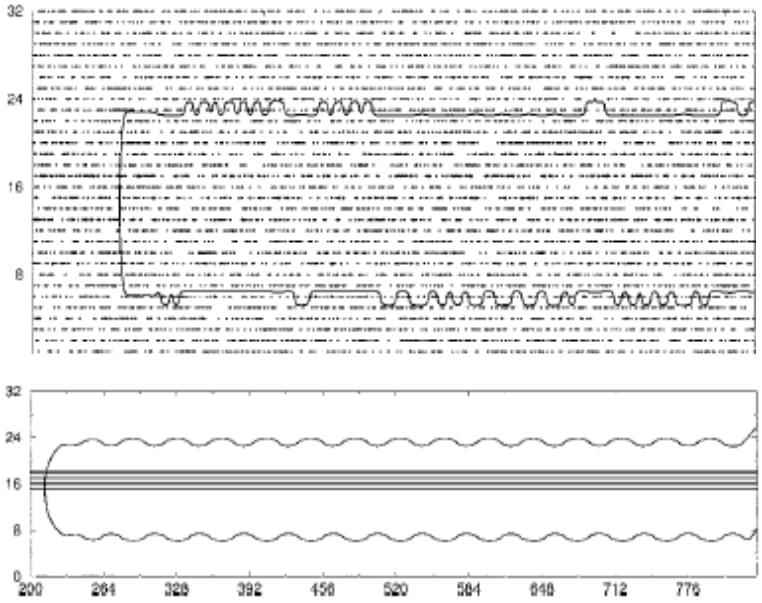

Figure 4.1: Top: Finger propagating in a cell with 10% coverage. Note that the scale has been compressed in the horizontal direction in order to better appreciate the instability. **Bottom:** Finger propagating in a cell with a stripe profile. From [Quevedo–Reyes 06].

4.3 Time dependent boundary condition

In the simulations with a time dependent boundary condition, most of the developed fingers were subjected to an oscillating pressure drop. When subjected to perturbation, the tip of the finger generated a wave which propagated away from the finger tip. Near the finger tip, the frequency of this new generated lateral instability was always the same as the imposed frequency. On the other hand, far from finger tip the relation between forcing frequency and response frequency was not so simple (Fig. 4.2). The amplitude of the lateral instability increased up to a saturation value at a distance d_s from the finger tip which was strongly dependent on forcing frequency.

For frequencies below ν_∞ the frequency of the lateral instability was the same as the forcing frequency (Fig. 4.3) and $d_s \sim \Lambda$. In the range of frequencies (ν_∞, ν_{finger}) the response frequency corresponded to half the incident frequency and $d_s \sim 2\Lambda$ (Fig. 4.3). The surface tension in this region was enough to suppress driving frequency but not its first harmonic. Last, for driving frequencies larger than ν_{finger} there was a mode that grew faster than the others and was selected. These selected mode was independent of driving frequency in a wide range of frequencies. The selected frequency was slightly higher than ν_∞ and the lateral instability reached its saturation amplitude very far from the finger tip: $d_s \sim 5\Lambda$.

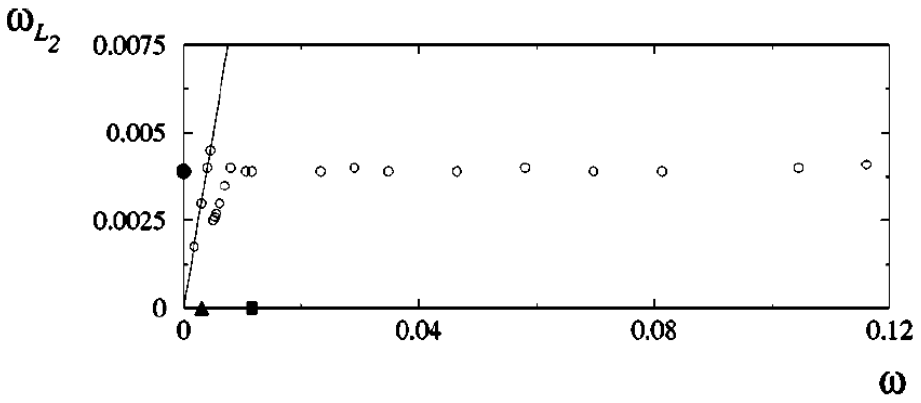

Figure 4.2: Response frequency measured far from the fingertip plotted against incident frequency. For a wide range of frequencies mode selection occurs. The natural frequencies of the flow ω_∞ (▲) and ω_{finger} (■) are indicated in the abscissa axis. From [Ledesma-Aguilar 05].

Simulations with a random signal added to the constant pressure drop were also reported in Ref. [Ledesma-Aguilar 05]. The response was essentially the same as the one described for the static disorder. These authors report fingers with non–periodic response undergoing a selection progress far from finger tip. The selected frequency was slightly below ν_∞.

4.4 Summary

Summarizing, all the destabilization mechanisms produced a lateral instability which presented a preferred frequency. For the persistent anisotropy experiments, this frequency depended on properties of the anisotropy. On the contrary, for the random stationary and dynamic disorder and for the oscillating pressure drop the selected

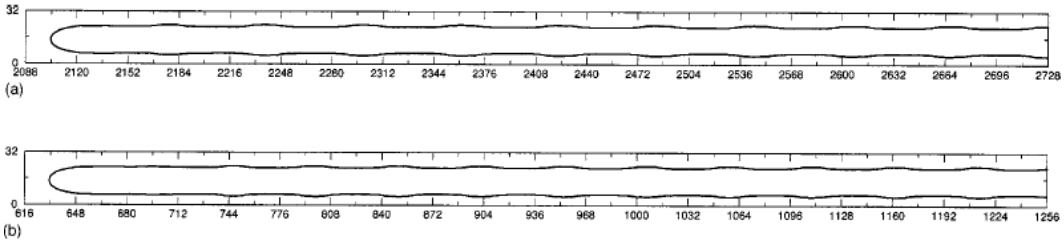

Figure 4.3: The profile at the top corresponds to an driving frequency that falls in the linear region of the ω_{L2} *vs* ω (Fig. 4.2), whereas the profile at the bottom corresponds to a frequency that falls in the transition region of the same curve. The distance d_s at which the amplitude saturates is of the order of $d_s < L$ and $d_s > 2L$, respectively. These are regimes that would be easier to observe experimentally than the selection regime. From [Ledesma-Aguilar 05].

frequency depended only on the characteristic frequencies of the system. For these three last perturbations the selected frequency was roughly equal to ν_∞.

A natural objection to these results is the lack of experiments confirming the predictions. In real systems, at velocities for which an stationary stable finger ($\lambda \geq 0.5$) is formed, no lateral instability has been reported, except for Ref. [Moore 02].

Let us show that there is no contradiction between experimental and simulation results. The selected wavelength was $\Lambda \simeq W/\lambda$. Thus, it was of the order of the channel width. On the other hand, the saturation distance was of the order of the channel width and increased as the amplitude of the external perturbation (the eventual noise of the experimental device) decreased. This would explain why the experimental fingers reported in the literature did not present this lateral instability. Most of them were generated in cells too short to allow for the instability to develop (for instance, in Refs. [Saffman 58; Pitts 80] the length of the cell was roughly $3W$).

Our goal was the development and characterization of the lateral instability, even in the selection regime. Thus, we used the numerical results in order to design an experimental device where the low amplitude lateral instability could be observed and characterized. For instance, the selected wavelength in the simulations with random anisotropy was of the order of the channel width. In addition, the instability was observed when the finger tip had travelled a distance $\simeq W$. It was necessary to design a channel for which $L/W \gg 1$. This was specially important in the experiments with an oscillating pressure drop, as the saturation distance in the selection regime was of the order of $10W$. The designed experimental device, as well as the experimental results and concluding remarks are presented in Chapters 5, 6, 7 and 8.

Chapter 5

Lateral instability in Saffman–Taylor fingers: Experimental methods

The aim of our experiments in a Hele-Shaw cell was the study of a lateral instability of normal Saffman-Taylor fingers. The main objectives of our experiments were the destabilization of the flat sides of the finger by two different physical mechanisms (quenched disorder and periodic pressure oscillations) and the characterization of the instability developed in the finger. These experiments required very long fingers.

A long channel was designed to generate fingers long enough to our experiments. The instability showed typical wavelengths similar to the channel width W. We designed experiments with fingers $20W$ long for quenched disorder experiments and $40W$ long for periodic perturbation experiments.

5.1 The Hele–Shaw cell

We performed our experiments in a horizontal linear Hele-Shaw cell (Fig. 5.1) formed by two glass plates separated by a narrow gap spacing. The glass plates were 1300 mm long and 19 mm thick. Their width was 75 for the top plate mm and 120 mm for the bottom plate. The cell was placed on six stainless steel supporters. The supporters were carefully machined to provide a uniform height and were placed symmetrically along the cell. Doing this, we avoided possible bending effects in the channel direction of the cell.

The air inlet and the oil outlet consisted of two openings in the bottom plate. They were placed at 5.5 mm of each end of the plate, the effective length of the

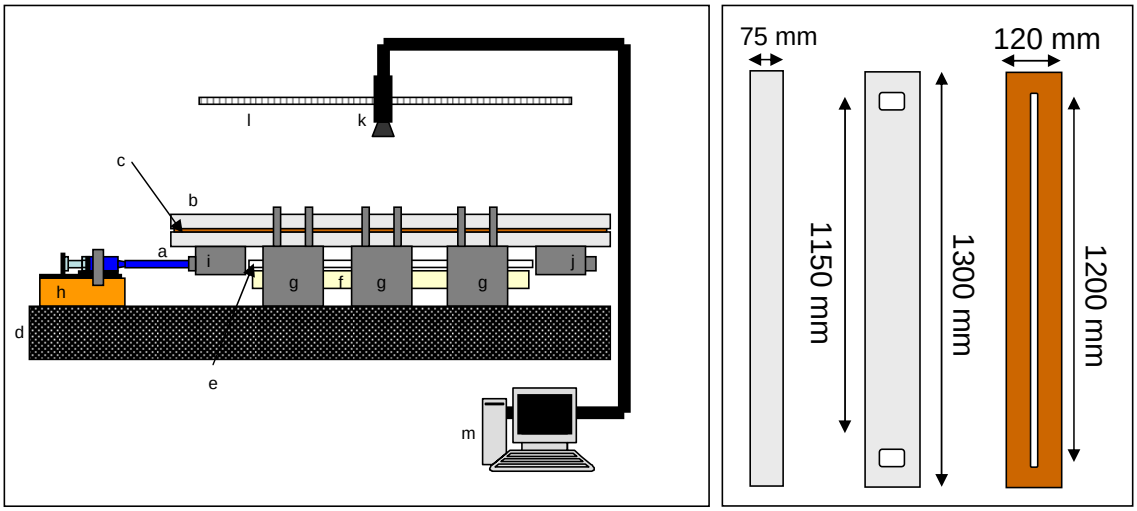

Figure 5.1: Left: Scheme of the experimental device for the study of lateral instabilities in Saffman-Taylor fingers. (a) Bottom plate, (b) top plate, (c) brass spacer, (d) anti-vibration table, (e) light diffuser, (f) high frequency fluorescent lamp, (g) supporters, (h) syringe pump, (i) oil outlet, (j) air inlet, (k) CCD camera, (l) rail, (m) PC. **Right:** Scheme of the glass plates and brass spacer of the Hele shaw cell.

channel between both openings being 1150 mm. The oil outlet was connected to a syringe pump which could inject or withdrawn oil at selectable flow rates. The configuration of the experimental setup allowed flow rates in the range $(-1.1, 1.1)$ cm^3/s.

The cell was illuminated from below with a 35 kHz fluorescent lamp, 1200 mm long, covered with a white plastic to diffuse light. Images of the cell were recorded by a CCD camera placed above the cell (Fig. 5.1). The CCD could travel along the cell at velocities from -20 to 20 mm/s. The maximum acquisition rate of the CCD was 60 frames/s of size 640×480 pixels. The resolution of the frames captured was between 0.077 mm/pixel and 0.16 mm/pixel.

5.1.1 Quenched disorder

The disorder in our experiments was generated by fixing a fiber glass plate (printed circuit board) on top of the bottom glass plate. The disorder consisted on copper islands of fixed dimensions randomly distributed on the fiber glass plate (Fig. 5.2).

The idea of using printed circuits boards as disorder plates in our Hele-Shaw cell was taken from J. Soriano PhD thesis [Soriano 03]. Details on design and generation of the disorder distribution can be found in [Soriano 03].

The dimensions of our fiber glass plates were 24×500 mm, and 1.7 mmm high.

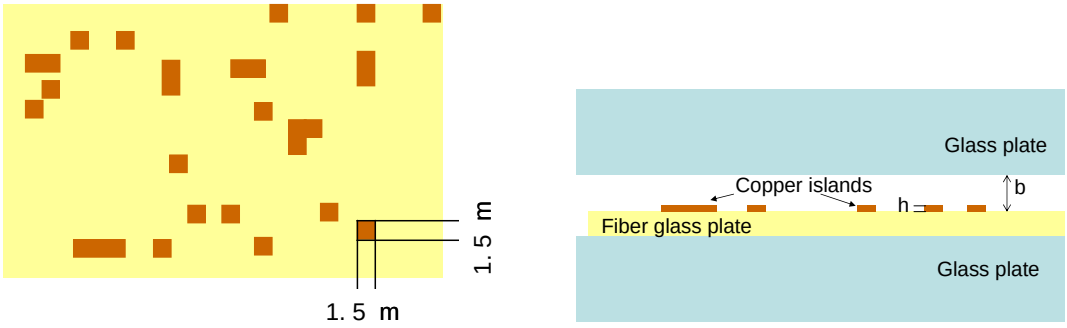

Figure 5.2: Left: Example of a disorder plate with an occupation rate of 10%. **Right:** Lateral view of the Hele-Shaw cell with quenched disorder experiments. The brass frame is not displayed. b: Effective gap spacing. h: Copper islands height.

The copper islands had lateral size of 1.5×1.5 mm and a height $h = 60$ μm. We used two kinds of disorder plates: low occupation ratio (10% of the total area filled by copper islands) and high occupation ratio (35% of the total area filled by copper islands).

The gap spacing was controlled by means of a brass frame 1300 mm long. The frame was designed to provide a channel of width 55 mm. The channel width could be modified by brass strips (1200 mm long, 20 mm width) placed parallel to one of the sides of the frame by means of brass wedges. For quenched disorder experiments the width of the channel was $W = 24$ mm.

We performed experiments with two different gap spacings 2.5 and 3.0 mm. With this purpose we combined two brass frames (and two brass strips) for each gap spacing of thickness: 2.0 and 0.5 mm for the first, 2.0 and 1.0 mm for the second. The frames were carefully aligned and the disorder plate was then fixed to the bottom plate.

The effective gap spacing b in these experiments was measured as the distance between the fiber glass plate (thickness 1.7 mm) and the upper glass plate. Thus, we used effective gap spacings of 0.8 and 1.3 mm. The relative variations in gap spacing due to copper islands were 7.5% and 4.6%, small variations.

5.1.2 Periodic perturbation

For periodic perturbation experiments we connected an air pump to the air inlet (Fig. 5.3). The air pump consisted of a mobile piston placed inside a plastic cylinder. The piston had a cross section of 4400 mm^2 and oscillated at frequencies up to 1.5 Hz. The air pump was designed to admit air in order to allow the air finger advance towards the end of the cell. The air entered freely the pump when the volume of air inside the pump was maximum. The volume of air in the cylinder oscillated between

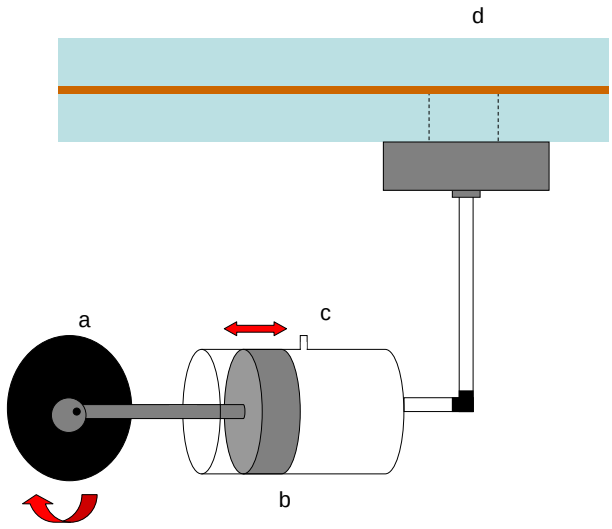

Figure 5.3: Air pump system for performing periodic perturbations in the velocity of the finger tip. (a) Motor, (b) piston, (c) air entrance (d) Hele–Shaw cell.

220 cm^3 and 100 cm^3.

The gap spacing between both plates was controlled by a brass frame of dimensions 1300 × 120 mm and thickness $b = 1$ mm. The channel width was $W = 25.0 \pm 0.1$ mm. The long sides of the frame were very wide to avoid lateral flexion and ensure a constant channel width.

5.2 Fluid properties

For all the experiments we used silicone oil Rhodorsil 47V500 as viscous fluid. This fluid has a dynamic viscosity $\eta = 0.518 \pm 0.002$ Pa·s at 20°C, density $\rho = 975 \pm 10$ kg/m^3, and oil–air surface tension $\sigma = 20.7$ mN/m. The color contrast between air and oil was increased by coloring the oil with Oil Blue N (from Sigma-Aldrich), without a measurable change in viscosity, as verified by rheological tests (Fig. 5.4). We also measured the surface tension of the colored sample and found that the difference in surface tension between the colored sample and the uncolored sample was below 5%.

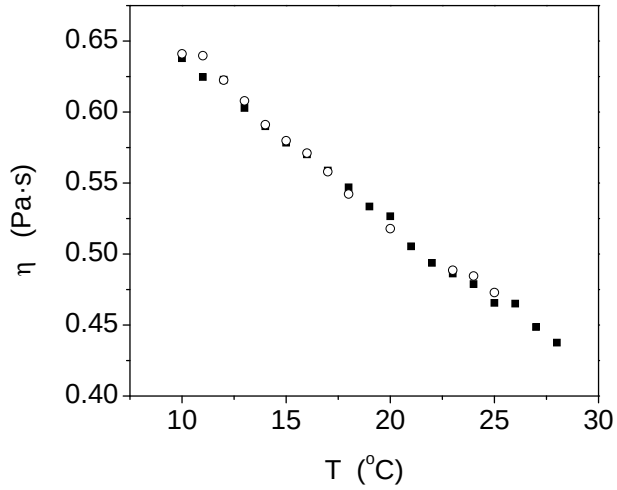

Figure 5.4: Dynamic viscosity of silicone oil Rhodorsil 47V500 at different temperatures. Filled squares correspond to uncolored oil and open circles to colored oil.

5.3 Experimental procedures and data analysis

5.3.1 Quenched disorder experiments

The disorder in the cell induces a lateral instability in the flat sides of the Saffman–Taylor finger. The typical wavelength of this instability has a value close tho the cell width W. In order to obtain an statistical measurement of this disorder–induced lateral instability, the experiments were performed with several different disorder realizations: 4 disorder plates in the experiments with $b = 1.3$ mm and 10 % occupation ratio, and 3 disorder plates in the other experiments.

Although the disorder plate had a length of 500 mm, we only used a part of the finger in our measurements. We observed that each finger presented three different regions (Fig. 5.5). The regions identified were:

- **Head**: the front part of the finger. In the head the lateral instability does not reach its full amplitude.
- **Tail**: the part that stays far away from the finger tip. The shape of the tail is strongly dependent on time.
- **Body**: the part of the finger where the amplitude of the instability has saturated and, thus, pictures of the finger at different times are identical.

In order to determine the size of the tip region, pictures of tips at different times were superimposed to each other. For the body and tail regions, we left the camera

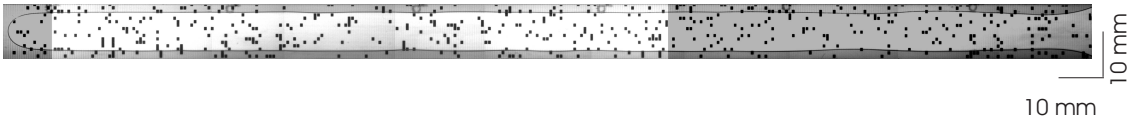

Figure 5.5: Example of a finger generated in quenched disorder experiments for $b = 0.8$ mm, 10% coverage. The average velocity of the finger was $U = 2$ mm/s. The bright region is the body of the finger and the dark regions correspond to the tip (left end) and the tail (right end).

fixed in space and captured pictures during the course of the whole experiment. Once the pictures awere overimposed, it was possible to determine the spatial extent of each region. The length of the tail was found to be almost independent of the velocity of the finger, and the length of the tip did show a nonmonotonic dependence with velocity. Care was taken to distinguish the three regions in each case and the results presented in this thesis correspond exclusively to the finger body.

We restricted to the body because of the low amplitude of the instability, which made necessary to increase the resolution of our images. We captured pictures at a resolution of 0.077 mm/pixel (0.003 W/pixel), which was enough for the instability to be characterized. On the other hand, each frame displayed a short part of the finger. The images of long fingers (Fig. 5.5) were obtained following the steps:

1. The CCD camera was placed at the end of the disorder plate.
2. The finger was generated by withdrawing oil at a constant velocity V_∞.
3. Once the finger tip had advanced a distance $L \gg W$, the CCD travelled towards the air inlet at a high velocity and took pictures at 2 frames per second.

The image of a long finger (Fig. 5.5) was obtained by mounting several frames. For each finger, we analyzed only the body (the stationary part) of the finger. The range of finger velocities U studied in quenched disorder experiments was (0.11, 15.00) mm/s.

Fluctuations in finger width

The body of the finger was digitized. For each finger we obtained the profiles of the left side of the finger $y_{left}(x_i)$ and the right side $y_{right}(x_i)$. From these two measurements we calculated the width of the finger $\lambda(x_i) = (y_{left}(x_i) - y_{right}(x_i))/W$ and the mean finger width λ:

$$\lambda = \frac{1}{N} \sum_i \lambda(x_i), \tag{5.1}$$

typically for $N \simeq 3000$ values of the width.

Fluctuations in finger width were characterized by the standard deviation of the finger width δ_λ along the finger:

$$\delta_\lambda = \sqrt{\frac{1}{N-1}\sum_i (\lambda - \lambda(x_i))^2}. \tag{5.2}$$

Last, for each velocity we generated 4 (or 3, in some of the configurations) independent fingers. The final value of λ and δ_λ was calculated as the weighted average of these quantities.

Frequency distribution of the lateral instability

We measured the wavelength Λ of the lateral instability as the distance between two maxima of the finger width. The corresponding frequency of the lateral fluctuations was calculated as follows:

$$\nu_{out} = \frac{U}{\Lambda} = \frac{V_\infty}{\lambda\Lambda}, \tag{5.3}$$

where withdrawal velocity far from finger tip V_∞, and finger tip velocity U, are used.

For each finger, frequencies of the lateral fluctuations were determined independently at each side of the finger, since fluctuations in both sides do not seem to be correlated in an obvious way. The results for different disorder plates were also considered as independent measurements.

5.3.2 Periodic perturbation experiments

The fingers were generated by withdrawing oil at constant rate V_∞. Once the finger had reached its stationary width and advanced by the center of the channel (a distance $6W$ from the air inlet), the pump was switched on. As a result, the velocity of the tip of the finger oscillated around the mean value imposed by the withdrawal velocity. The resolution was fixed to 0.16 mm/pixel (0.006 W/pixel) and the withdrawal velocities used were $V_\infty = 1.42$ mm/s and $V_\infty = 2.83$ mm/s.

Pictures of long fingers in periodic perturbation experiments were generated with the same procedure described in Section 5.3.1. However, we observed that the stationary region of the finger at high forcing frequencies was reached very far from finger tip. In addition, the maximum velocity at which our CCD could travel along the cell was comparable to the finger velocities. Thus, at high forcing frequencies the stationary part of the finger was very small. Although at lower forcing frequencies the

Figure 5.6: Example of a long finger generated in periodic perturbation experiments. The forcing frequency was 0.22 Hz and $V_\infty = 1.42$ mm/s. The bright region is the ROI analized in time evolution experiments.

stationary region was close to the finger tip (Fig. 5.6), we performed measurements of the time evolution of the sides of the finger at a fixed distance of the air inlet for all forcing frequencies except the two lowest ones.

Measurements of the stationary frequency of the lateral instability.

The section of the finger we captured (our region of interest or ROI) had dimensions $W \times 4W$. First, it was important to decide the position of the ROI (Fig. 5.6). We located the ROI following two criteria:

- It was important to set the CCD far enough from the oil outlet to allow for the lateral instability of the finger to reach its stationary state.

- It was important to discard possible transient effects due to switching on the forcing.

Consequently, the ROI was placed at $12.5W$ of the air inlet. The capture began when the finger tip entered the ROI (at time 0) and ended when the tip of the finger had advanced a distance of approximately $30W$ from the ROI (at time T).

The wavelength of the lateral instability was measured in the same way than in quenched disorder experiments. Differently from the lateral instability in quenched disorder experiments, the lateral instability at each side of the finger under periodic forcing was strongly correlated. Thus, we measured the lateral instability of only one side of the finger.

To find out wether an stationary state had been reached, we compared the wavelength of the lateral instability at times $0.8T$, $0.9T$ and T. If the difference between the wavelengths measured at $0.9T$ and T were below our experimental resolution, we concluded that the lateral instability had reached an stationary value. When this happened, the mean value of the measured wavelength at time T, Λ, was taken as the wavelength of the lateral instability.

The width of the finger $\lambda(x)$ was measured as in quenched disorder experiments, and only for the ROI. The mean finger width λ was obtained as an average over 640 values.

Last, the frequency of the lateral instability was calculated using Eq. (5.3) and the fluctuations in finger width were calculated following Eq. (5.2).

As the measurements were performed in a small region of the finger, we could measure only a few Λ in each finger. We performed 5 independent runs of each experiment. The value of ν_{out} and λ were obtained as weighted averages over the five independent runs. For the smaller frequencies we considered both the instrumental uncertainty and the standard deviation of the measurements to compute the final uncertainty. For the middle and high frequencies, since the number of measurements in each run increased, it sufficed to consider only the instrumental uncertainty of the measurements.

Low frequencies: long fingers

For the two lowest forcing frequencies studied (0.02 and 0.03 Hz) the typical wavelength of the pattern was longer than the ROI lateral size. The ROI could not be enlarged because of the low amplitude of the lateral instability. In principle, since the wavelength evolved as it propagated far from the tip, an image reconstruction of the finger made of pictures taken at different times was not possible. However, for very small forcing frequencies, the structure that was born close to the finger tip persisted along the finger as this one advanced. We therefore decided to analyze these fingers by making the camera travel above the well-developed finger and by making an image reconstruction of the whole finger.

At low forcing frequencies, the shape of the finger sides did not have a sinusoidal-like profile. Instead, it was characterized by a saw-tooth wave profile. We applied a fast Fourier transform (FFT) analysis to the two lowest frequencies studied in the following way: we carried out three realizations of the experiment for each forcing frequency and we obtained a reconstruction of a long finger for each realization. The reconstructions were digitized and a FFT transform was applied to repeated structures on one of the finger sides. The position of the largest peak of the FFT was associated with the wavelength, Λ, for each realization. This, together with the mean finger width, λ, allowed for the calculation of the response frequency. We obtained the final response frequency as the weighted average over the three realizations.

In order to check that this method gave reasonable results, we applied both types of data analysis to the lowest four forcing frequencies for which the regular data

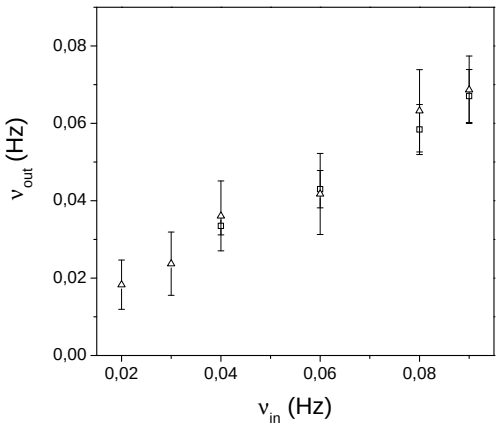

Figure 5.7: Frequency of the lateral instability ν_{out} as a function of forcing frequency ν_{in} for $V_\infty = 1.42$ mm/s at low forcing frequencies. The graph contains ν_{out} measured with two different experimental procedures: (□) time evolution measurements and (△) long finger measurements (FFT).

analysis was possible. We confirmed that the results of the FFT analysis of the reconstructed image leaded to the same response frequencies than the regular analysis applied for the higher forcing frequencies (Fig. 5.7).

Chapter 6

Quenched disorder

In all the series of experiments, the aspect ratio of the cell W/b was chosen to be $\simeq 10$, which is small compared to the aspect ratios explored by the long fingers reported in [Moore 02]. The sides of the fingers reported in [Moore 02] presented spontaneous fluctuations, while our intention was to induce the instability in fingers which would present flat sides in the absence of perturbations.

The lateral instability measured both for quenched disorder and for periodic perturbation experiments, was a long wavelength, low amplitude instability. As commented in Ch. 10, for both kinds of experiments we were interested in the frequency ν_{out} and the amplitude δ_λ of the lateral instability.

The first noticeable result was to find out that the lateral instability was developed with a very weak disorder in the gap spacing (even for variations in the gap spacing below 5%, the finger sides developed the instability). The lateral instability had a very low amplitude and a wide spectra of wavelengths (Fig. 6.1) .

The static disorder was feeble enough to allow normal Saffman-Taylor fingers to develop. The tip of a finger generated in our Hele-Shaw cell resembled the tip of a normal Saffman-Taylor finger and was stable to the presence of the quenched disorder. On the contrary, the flat sides of the finger were unstable and developed a lateral instability which propagated away from the finger tip (in the finger frame of reference). The amplitude of the instability increased to a saturation value. Once the saturation amplitude was reached, and in the laboratory frame of reference, the shape of the finger was stationary. For fixed experimental parameters (b, V_∞, and disorder plate) the fingers were identical. Clearly, the details of the fluctuations on the finger sides differed for different configurations of static disorder, but the statistical behavior was the same.

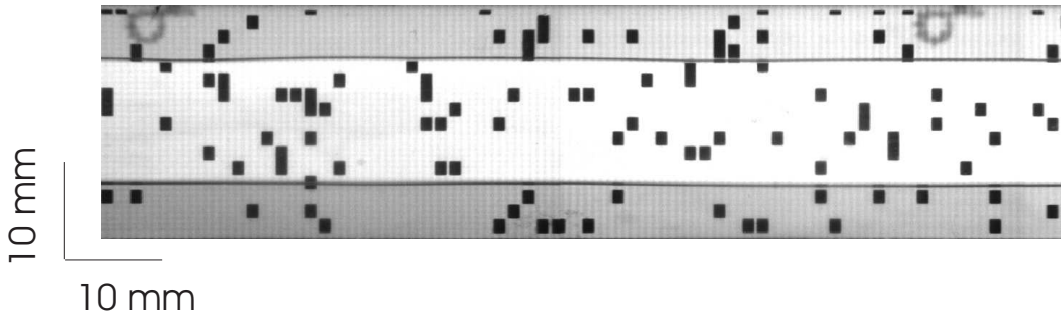

Figure 6.1: Detail of the lateral instability observed in quenched disorder experiments. The image corresponds to a finger with a mean velocity $U = 7.84$ mm/s in a cell with $b = 1.3$ mm and 10% coverage.

Geometry		A	B	C
Coverage	%	10	10	35
Effective gap spacing	b (mm)	0.8	1.3	1.3
Cell width	W (mm)	24	24	24
Relative variations in gap spacing	h/b (%)	7.5	4.6	4.6
Withdrawal velocity	V_∞ (mm/s)	1.12	1.22	1.22
Characteristic frequency at infinity	ν_∞ (Hz)	0.047	0.051	0.051

Table 6.1: Experimental parameters of the three geometries studied.

6.1 Effect of the static disorder

The properties of the static disorder were controlled by two variables: the coverage and the gap spacing b, while flow rates were chosen to give equal finger velocities up to two significant figures. Experimental parameters for the tree configurations studied are shown in Table 6.1.

Representative fingers for each geometry are displayed in Fig. 6.2. The distributions displayed in Fig. 6.3 are results of the different configurations of static disorder for each geometry. A summary of the main results for each geometry is shown in Table 6.2.

The properties of the disorder were related to the statistical properties of the lateral instability in the following way:

- Effect of the intensity of static noise

  We compared the results of two geometries with the same coverage (10%) varying only the gap spacing (geometries A ($h/b = 7.5\%$) and B ($h/b = 4.6\%$)).

The smallest the gap, the larger the intensity of the noise. Top and middle fingers in Fig. 6.2 are two examples of fingers for each geometry. In the top and middle graphs of Fig. 6.3 we show the corresponding distributions.

In both cases, most of the frequencies of the lateral instability were contained in a band $\nu_\infty < \nu < \nu_{fing}$. The smallest frequencies observed were close to ν_∞. At high frequencies the behavior in both geometries was also similar: a tail that decayed to zero at frequencies few times larger than the characteristic frequency of the finger. The width of the distributions was also similar. The standard deviations of the data, 0.052 Hz and 0.046 Hz for the 0.8 mm and 1.3 mm gaps, respectively, and the means of the distributions, 0.124 Hz and 0.116 Hz for the 0.8 mm and 1.3 mm gaps, respectively, also indicated that there was not an obviously quantifiable difference in the distributions.

- Effect of the coverage

  We also compared the results of two geometries with the same intensity of noise (4.6% variation of gap spacing) and different coverage (geometries B and C). The frequency distributions for coverage of 10% and 35% are displayed in the middle and bottom graphs of Fig. 6.3. At low frequencies the behavior was the same as described above. At high frequencies, the tail for high coverage reached larger frequencies than the tail for small coverage. This indicated that high coverage induced the presence of fluctuations of small wavelength in the lateral instability. Nevertheless, in both cases the tail of the distribution decayed to zero at frequencies few times larger than the characteristic frequency of the finger. The standard deviations of the data, 0.046 Hz and 0.090 Hz for coverages of 10% and 35%, respectively, and the means of the distributions, 0.116 Hz and

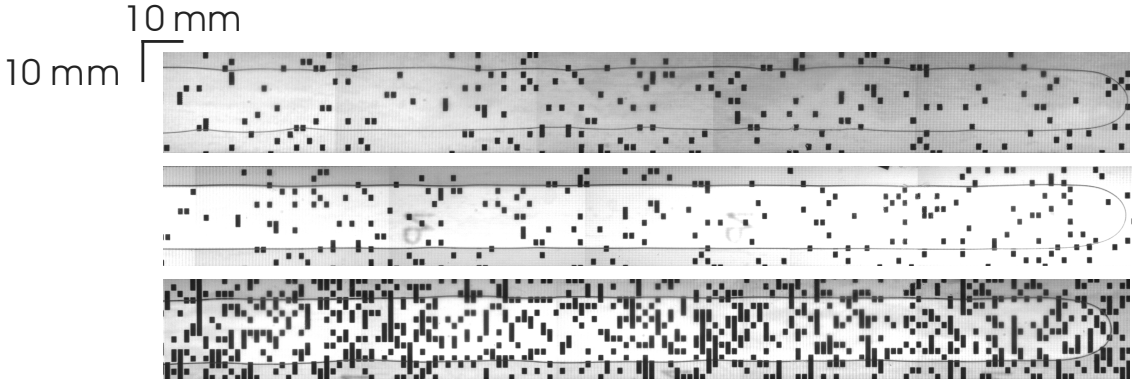

Figure 6.2: Images of fingers obtained at fixed finger velocity (U = 2 mm/s) in the three different geometries described in table 6.1 A, B, and C (from top to bottom).

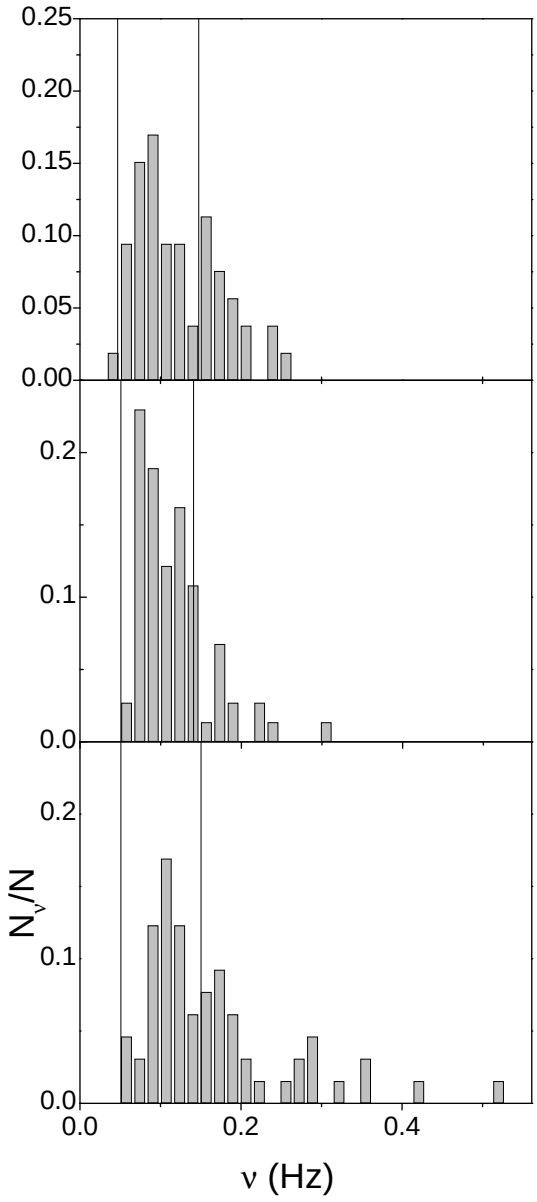

Figure 6.3: Distributions of frequencies of the lateral instability corresponding to the three different geometries described in Table 6.1. Vertical lines are the characteristic frequencies of the system (left: ν_∞, right: ν_{fing}). The geometries A, B and C are ordered from top to bottom.

0.164 Hz, also indicated that the range of frequencies that grew in the lateral instability was larger for the high coverage case, and that the distribution was slightly shifted towards high frequencies which correspond to short wavelengths.

Table 6.2 describes the properties of the fingers developed in each geometry. We observe that the rms fluctuations of finger width increased with the intensity of the static noise and with the coverage. Since these fluctuations provide a measure of the

Geometry		A	B	C	
	U (mm/s)	2.01	2.03	2.01	($\pm$0.05 mm/s)
	λ	0.56	0.60	0.58	
	ν_{fing} (Hz)	0.15	0.14	0.15	($\pm$0.03 Hz)
	δ_λ (mm)	0.0185	0.0064	0.0115	($\pm$0.0012 mm)
	N	53	74	65	

Table 6.2: Measured finger properties for the geometries described in Table 6.1. U: Mean finger velocity. λ: Mean finger width. ν_{fing}: Characteristic frequency of the finger. δ_λ: rms fluctuations in finger width. N: Total number of measurements.

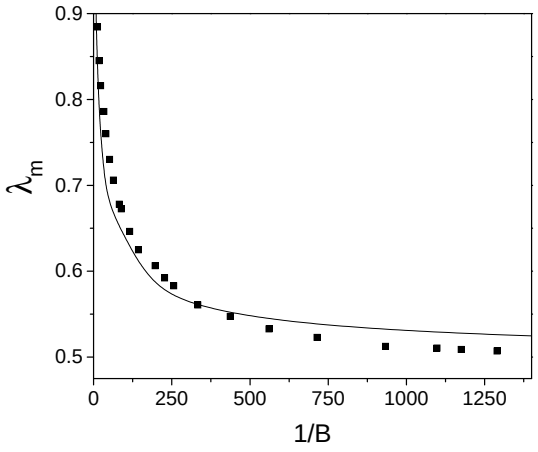

Figure 6.4: Mean finger width as a function of $1/B$. The solid line correspond to the theoretical values of McLean and Saffman [McLean 81]. Solid squares are the experimental values of the mean width averaged over four different disorder configurations.

amplitude of the lateral instability, we concluded that fluctuations increased with the two possible mechanisms of increasing the static noise in the cell.

Summarizing, the frequency distribution of the lateral instability was very similar in all the geometries. Most of the frequencies were contained in the range (ν_∞, ν_{fing}) pointing to a possible preferred frequency which did not seem to depend on the properties of the static noise. On the other hand, rms fluctuations of the finger width increased with increasing the intensity of static noise.

6.2 Relation with capillary number

We studied the finger instability with static disorder for different flow rates. A plot of the average finger width as a function of capillary number (Fig. 6.4) shows that,

for all of our experiments, we had normal Saffman-Taylor fingers. Agreement with the McLean and Saffman curve is similar to results for the steady state reported in the literature [Tabeling 86].

We studied fingers in a wide range of capillary numbers $1/B$. Figs. 6.5 and 6.6 show six typical fingers obtained at different $1/B$ (fingers appear compressed in the horizontal axis, in order to facilitate the visual appreciation of the fluctuations).

6.2.1 Fluctuations in finger width

We studied the relation between the capillary number $1/B$ and the amplitude of the lateral instability. These experiments were performed at a fixed aspect ratio W/b. Thus, all the variations of $1/B$ corresponded to variations of Ca.

In some sense, our analysis was similar to the one carried out by Moore *et al.* [Moore 02]. But, differently from their measurements, we were interested on spatial variations in finger width instead of temporal variations. As can be appreciated in Figs. 6.5 and 6.6, the relation between the amplitude of the lateral instability and the capillary number was clearly non-monotonic. Fig. 6.7 shows the relation between $1/B$ and δ_λ.

Our results are qualitatively similar to those of [Moore 02], in the sense that δ_λ decreases as Ca increases and scales as a power law. At larger values of the capillary number δ_λ increases at increasing Ca, similarly to what happened in the experiments mentioned. Our results for the rms fluctuations of the finger width scale at low capillary number as $Ca^{-1/3}$ or, equivalently in our experiments, as $1/B^{-1/3}$.

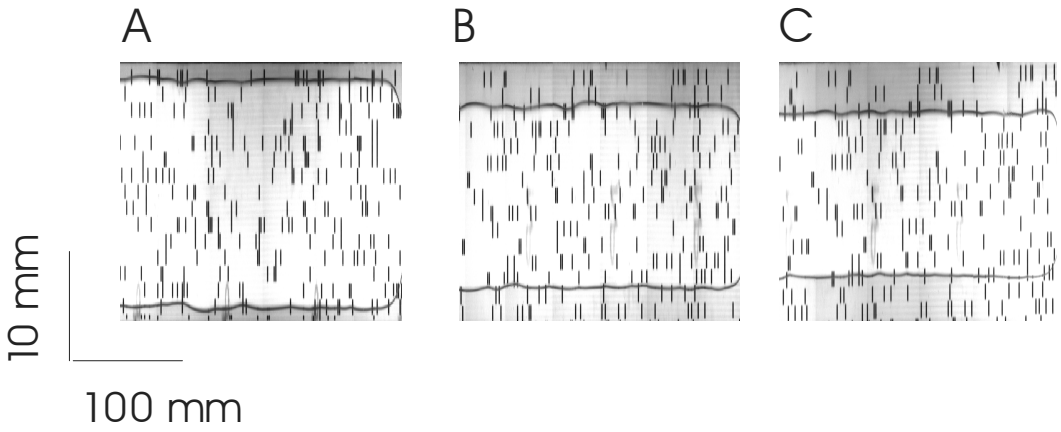

Figure 6.5: Plot of fingers in a cell with a 10% of area filled by copper islands, gap spacing $b = 1.3$ mm at several velocities. Each finger is marked in figure 6.7. **A:** $1/B = 18$, **B:** $1/B = 88$, **C:** $1/B = 198$.

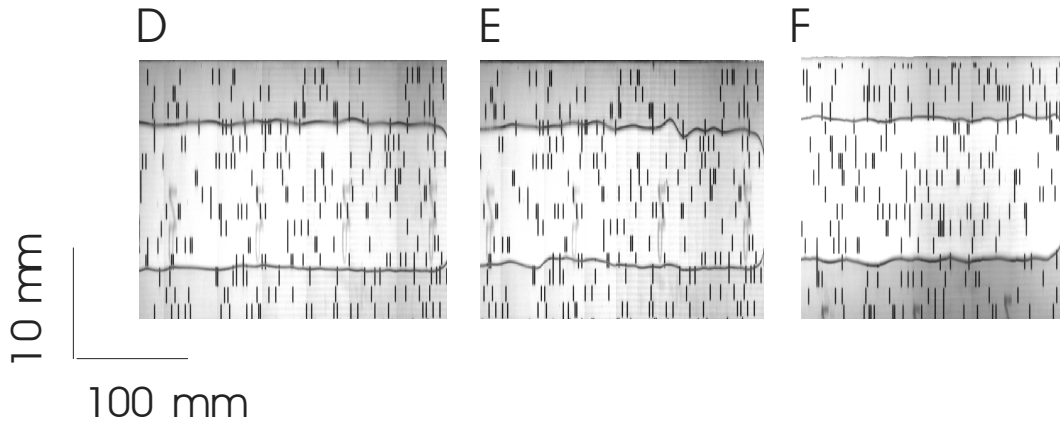

Figure 6.6: Plot of fingers in a cell with a 10% of area filled by copper islands, gap spacing $b = 1.3$ mm at several velocities. Each finger is marked in figure 6.7. **D:** $1/B = 339$, **E:** $1/B = 1091$, **F:** $1/B = 1300$.

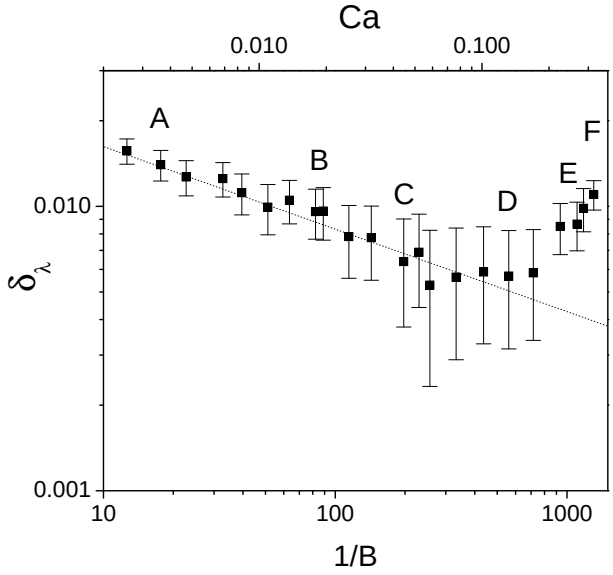

Figure 6.7: Fluctuations in the finger width vs $1/B$. Solid squares are the average fluctuations over four different disorder configurations. Dotted line is the best fit for the low velocity regime ($1/B$ from 0 to 250).

Specifically $\delta_\lambda = (0.034 \pm 0.008)(1/B)^{(-0.30\pm0.13)}$, for values of $1/B$ from 0 to 250.

6.2.2 Frequency distribution of the lateral instability

The particular properties of the disorder (coverage and intensity) did not affect the frequency distribution of the lateral instability (Section 6.1). Most of the frequencies of the lateral instability were contained in the range (ν_∞, ν_{fing}). But these two

characteristic frequencies depended on the velocity of the finger. Thus, we also studied the distribution of frequencies for fingers in a wide range of velocities.

Figs. 6.9 and 6.8 show these results. Fig. 6.8 displays frequency distributions for different velocities, while Fig. 6.9 shows variations of the mean and standard deviations for the data contained in the distributions as a function of Ca. From both figures, it is clear that the velocity of the finger determined the frequency distribution of the lateral instability. The frequency that dominated the pattern of the lateral fluctuation increased with increasing Ca (increasing U, in our experiments) indicating that, at large Ca, short wavelength fluctuations were more and more favorable. Also, the width of the distribution increased with increasing Ca, indicating that the range of frequencies that were not suppressed by surface tension increased with increasing Ca.

The mean frequency of the distribution increased linearly with Ca (Fig. 6.9): $\nu_{mean} = (4.9 \pm 0.4) \cdot 10^{-4}(1/B)^{(1.02\pm0.04)}$ Hz. The standard deviation of the distributions also presented this linear behavior.

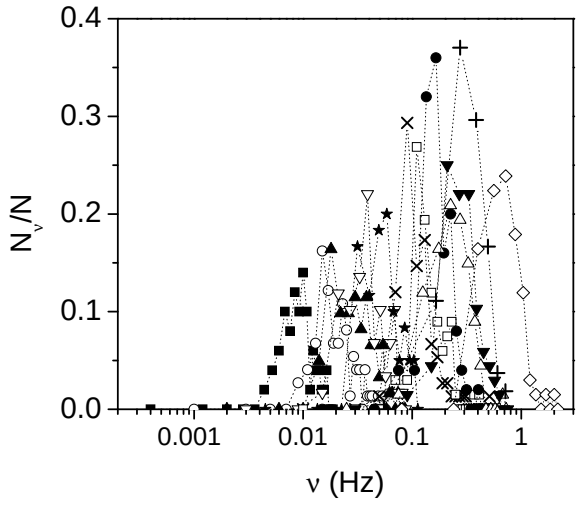

Figure 6.8: Histogram of the distribution of frequencies of the lateral fluctuations at different velocities. The symbols are: ■ $1/B = 23$, ∘ $1/B = 39$, ▲ $1/B = 63$, ▽ $1/B = 82$, ⋆ $1/B = 118$, × $1/B = 198$, □ $1/B = 254$, • $1/B = 339$, △ $1/B = 435$, ▼ $1/B = 558$, + $1/B = 925$, ◇ $1/B = 1268$.

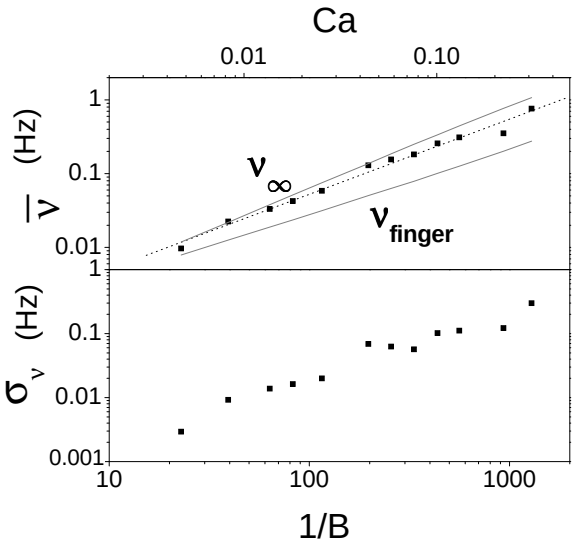

Figure 6.9: Top: Mean of the frequency distribution of the lateral instability vs $1/B$. Dotted line is the best fit for the experimental values of the frequencies of the lateral instability. **Bottom:** Standard deviation of the frequencies of the lateral instability as a function of $1/B$.

Chapter 7

Periodic perturbation

The instability developed in fingers subjected to periodic forcing had also a low amplitude and a long wavelength, but a simple look to the typical fingers developed in each series of experiments (Figs. 6.1 and 7.1) shows that both instabilities are very different. Fingers periodically forced display a symmetric instability, whereas the instability observed in fingers perturbed with static disorder is not symmetric at all. Another noticeable difference is the spatial periodicity of the lateral instability displayed for fingers periodically forced, which was not observed in quenched disorder experiments, where the instability had several wavelengths associated.

We performed measurements for two different withdrawal velocities $V_\infty = 1.42$ and 2.83 mm/s. As an example, a picture of the ROI of a finger at the lowest velocity is displayed in Fig. 7.1.

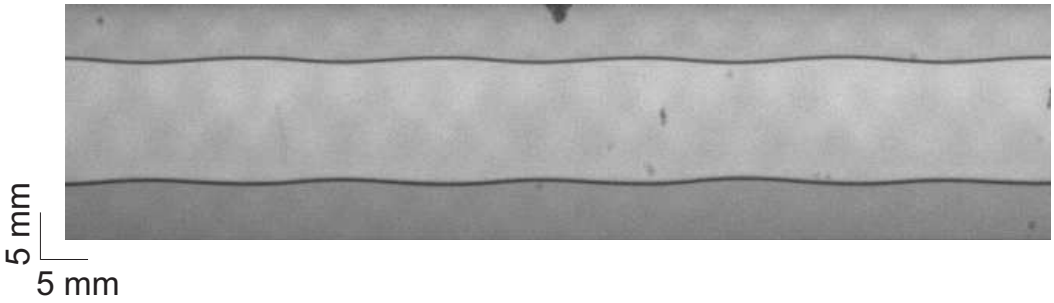

Figure 7.1: Image of the ROI studied in periodic perturbation experiments. The image corresponds to the stationary state of the lateral instability for a finger with a withdrawal velocity $V_\infty = 1.42$ mm/s and a forcing frequency $\nu_{in} = 0.19$ Hz.

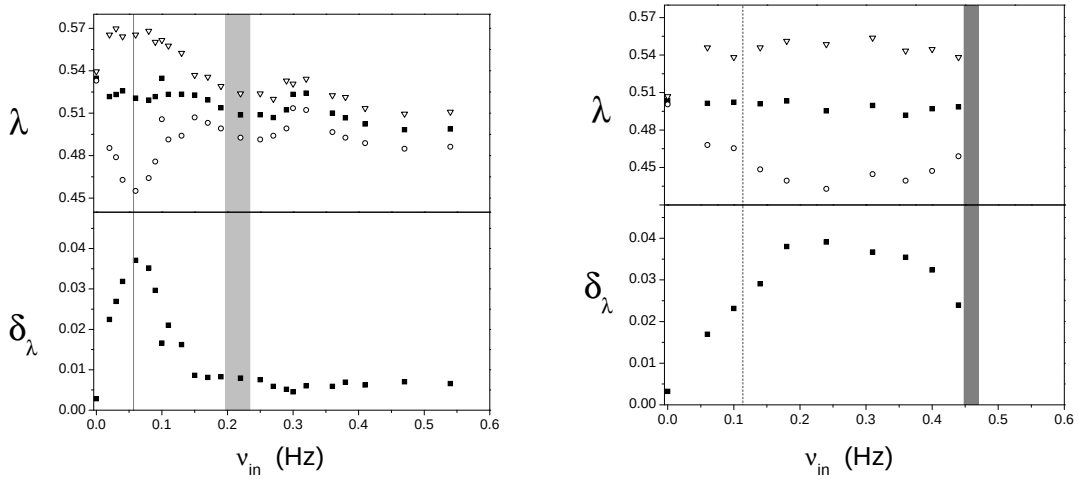

Figure 7.2: Top: Finger width as a function of forcing frequency: ■: λ_{max}, ▽: λ, and ○: λ_{min}. Bottom: Fluctuations in finger width as a function of forcing frequency. Vertical lines, from left to right, correspond to ν_∞, $\nu_{fing-min}$, and $\nu_{fing-max}$. **Left:** Results for a withdrawal velocity $V_\infty = 1.42$ mm/s. **Right:** Results for a withdrawal velocity $V_\infty = 2.83$ mm/s.

7.1 Finger width and fluctuations in finger width

The measures of the mean finger width λ, the maximum and minimum finger width λ_{max} and λ_{min}, and fluctuations in finger width δ_λ are displayed in Fig. 7.2 for both withdrawal velocities.

For each velocity, we observed that the mean finger width λ was not constant over the whole range of ν_{in} studied. Both for $V_\infty = 1.42$ mm/s and for $V_\infty = 2.83$ mm/s, $\lambda(\nu_{in} \neq 0) < \lambda(\nu_{in} = 0)$. For the lowest velocity, the mean finger width decreased considerably (from 0.54 for the unperturbed finger to a nearly constant value of 0.50 for the highest forcing frequencies). For the highest velocity, the finger width decreased from 0.51 to 0.50, which was a relatively small variation in finger width.

Considering that λ is not constant, we could not associate a single characteristic finger frequency to the experiment. Instead of a single ν_{fing}, we associated a band of characteristic finger frequencies ($\nu_{fing-min}$, $\nu_{fing-max}$) to each velocity:

$$\nu_{fing-min} = \frac{V_\infty}{\langle\lambda\rangle_{max}^2 W}, \tag{7.1}$$

$$\nu_{fing-max} = \frac{V_\infty}{\langle\lambda\rangle_{min}^2 W}, \tag{7.2}$$

where $\langle\lambda\rangle_{max}$ and $\langle\lambda\rangle_{min}$ correspond to the maximum and minimum value of the mean finger width λ measured over all the forcing frequencies. The range of finger

V_∞ (mm/s)	$\Delta\lambda$	ν_∞ (Hz)	$\Delta\nu_{fing}$ (Hz)
1.42	$0.498 - 0.535$	0.057	$0.197 - 0.234$
2.83	$0.492 - 0.504$	0.114	$0.449 - 0.470$

Table 7.1: Withdrawal velocities, range of values of average finger width, frequency characteristic of infinity, range of frequencies characteristic of the finger.

widths, velocities and the corresponding characteristic frequencies for each finger tip velocity are detailed in Table 7.1.

The behavior of λ_{min} and λ_{max} was strongly correlated: the highest value of λ_{max} corresponded to the minimum λ_{min}. Thus, although the width of the finger was locally subjected to strong variations, variations in λ were not dramatic. This was true for both withdrawal velocities. For $V_\infty = 1.42$ mm/s, and for forcing frequencies $\nu_{in} \gg \nu_{fig-max}$, both widths approached the value of λ. For the higher velocity, the range of high frequencies ($\nu \gg \nu_{fing-max}$) was not reached but the behavior of the amplitude of the instability was consistent with the one observed at the lowest velocity.

A direct measurement of the amplitude of the instability was δ_λ (Fig. 7.2). For both withdrawal velocities we found a forcing frequency for which the amplitude of the perturbation was maximum. For $V_\infty = 1.42$ mm/s this forcing frequency roughly coincided with ν_∞ whereas for $V_\infty = 2.83$ mm/s the maximum amplitude was slightly displaced to higher forcing frequencies.

The fluctuations in finger width at high frequencies were almost constant and very small for the lower velocity.

7.2 Lateral instability

In all experiments the first stage of the instability was similar: the lateral instability appeared near the finger tip, shortly after the air pump was switched on. The effect of the pump was an instantaneous change in finger tip velocity which advanced at a higher or a lower velocity. As a result, the finger width was modulated around a mean value with a typical frequency in the range ($0.4\nu_{in}$, ν_{in}).

As the finger tip travelled along the cell, this first stage could be stable or could be unstable and evolve to a new stage. We divided the experimental results in three different regimes, considering the modulations to the finger width very far from the finger tip (Figs. 7.3 and 7.4):

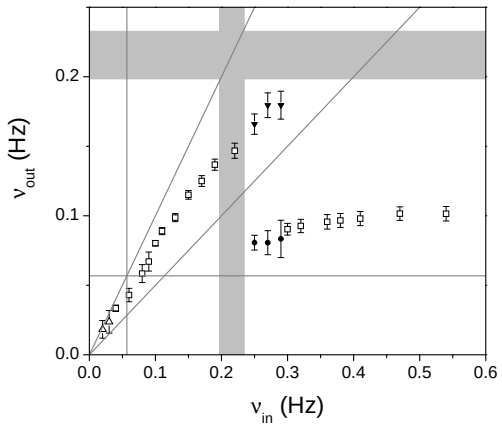

Figure 7.3: Frequency of the lateral instability as a function of forcing frequency for a withdrawal velocity $V_\infty = 1.42$ mm/s. □: Stationary states △: FFT of reconstructed fingers. Solid symbols: Non stationary states. Horizontal and vertical grey lines correspond to ν_∞. Horizontal and vertical grey colored bands correspond to the band of frequencies ($\nu_{fing-min}$, $\nu_{fing-max}$). Functions $y = x$ and $y = x/2$ are also plotted as guidelines.

- Frequency dependent regime ($\nu_{out} < \nu_{fing-min}$)
- Non stationary response region
- Selection regime ($\nu_{out} > 1.5\nu_{fing-max}$)

In Fig. 7.4 we have plotted the response frequency for the two velocities studied in

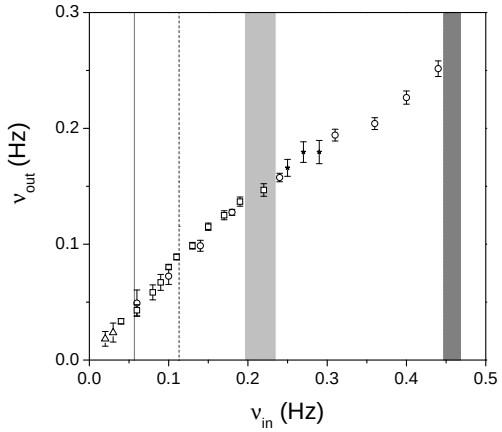

Figure 7.4: Frequency of the lateral instability as a function of forcing frequency for withdrawal velocities $V_\infty = 1.42$ mm/s and $V_\infty = 2.83$ mm/s. Open circles correspond to stationary states of $V_\infty = 2.83$ mm/s, the rest of the symbols are the same as in Fig. 7.3. Characteristic frequency of the flow and the band of finger characteristic frequencies are displayed for each one of the withdrawal velocities.

order to show that, as long as the forcing frequency is below the band of frequencies characteristic of the finger, the response frequency is independent of the withdrawal velocity. To study the selection regime at this higher velocity, one would need to apply frequencies much higher than the ones used in our experiment.

7.2.1 Frequency dependent regime ($\nu_{out} < \nu_{fing-min}$)

At low forcing frequencies, the response frequency increased monotonically as a function of forcing frequency up to forcing frequencies of the order of the characteristic band. Response frequencies in this zone seem to be bounded by the forcing frequency and half of the forcing frequency. The slope of the response frequency decreases systematically. At very low forcing frequencies the response was linear and, as the forcing frequency increased, the response approached $\nu_{out} = \nu_{in}/2$.

Fingers forced with a frequency below ν_∞ developed a lateral instability for which $\nu_{out} = \nu_{in}$ within experimental error. The lateral instability was symmetric but the sides of the finger did not present a sinusoidal-like profile. Actually, there were several frequencies present in the interface profiles. However, the dominant frequency (ν_{out}) always matched the forcing frequency. Finger profiles evolved from triangular periodic structures at very low frequencies (Fig. 7.5, left) to almost sinusoidal profiles as we approached ν_∞ (Fig. 7.5, right).

Fingers forced with a frequency in the range $\nu_\infty < \nu_{in} < \nu_{fing-min}$ presented a sinusoidal-like symmetric profile. The amplitude of the instability saturated near the finger tip (Figs. 7.6 and 7.7). As commented before, the results for both velocities were equivalent.

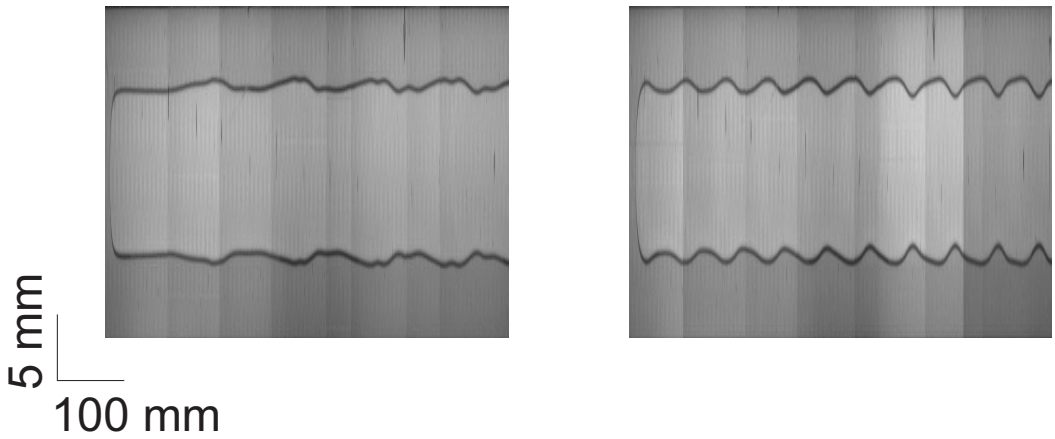

Figure 7.5: Long fingers for a withdrawal velocity $V_\infty = 1.42$ mm/s in the frequency dependent regime. **Left:** $\nu_{in} = 0.03$ Hz. **Right:** $\nu_{in} = 0.06$ Hz.

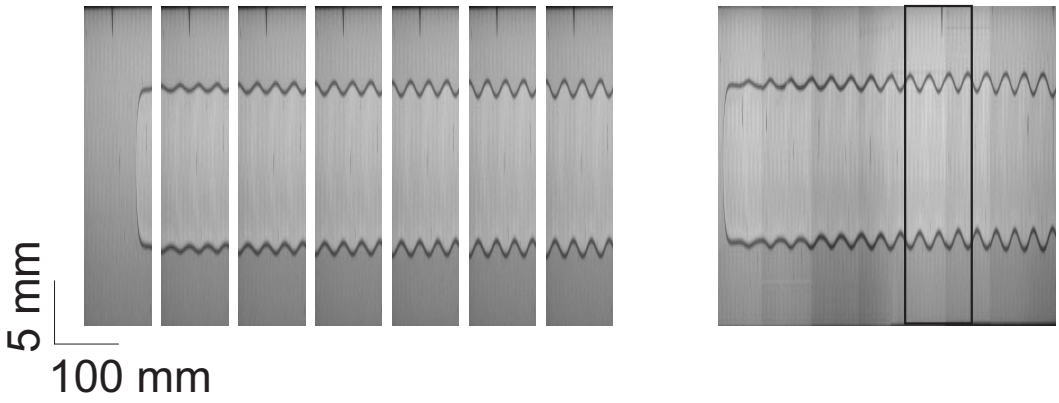

Figure 7.6: Typical fingers for a withdrawal velocity of $V_\infty = 2.83$ mm/s in the frequency dependent regime ($\nu_{in} = 0.36$ Hz). **Left:** time evolution of the ROI (shown in the long finger at right). The images are separated 12.5 s (1/10 of the total duration of the experiment). **Right:** picture of a long finger obtained by mounting together several images captured while the CCD camera travelled from the tip of the finger to the air inlet.

7.2.2 Non stationary response regime

At the lower velocity ($V_\infty = 1.42$ mm/s) we found a band of frequencies for which the finger did not reach a stationary final state (Fig. 7.3). A possible reason for this could be that the dynamics of the instability within this band was too slow. In that case the finger tip should advance a longer distance than the total length of our experimental setup to reach a stationary state.

For these frequencies we observed two kind of profiles. At early and interme-

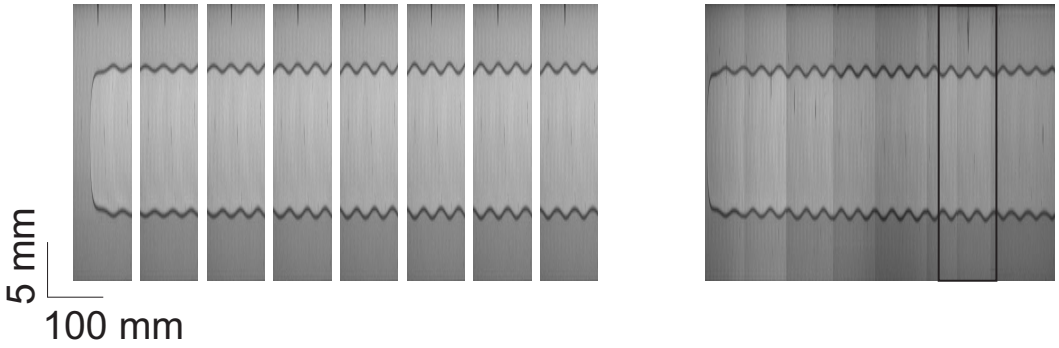

Figure 7.7: Typical fingers for a withdrawal velocity of $V_\infty = 1.42$ mm/s in the frequency dependent regime ($\nu_{in} = 0.11$ Hz). **Left:** time evolution of the ROI (shown in the long finger at right). The images are separated 25 s (1/10 of the total duration of the experiment). **Right:** picture of a long finger obtained by mounting together several images captured while the CCD camera travelled from the tip of the finger to the air inlet.

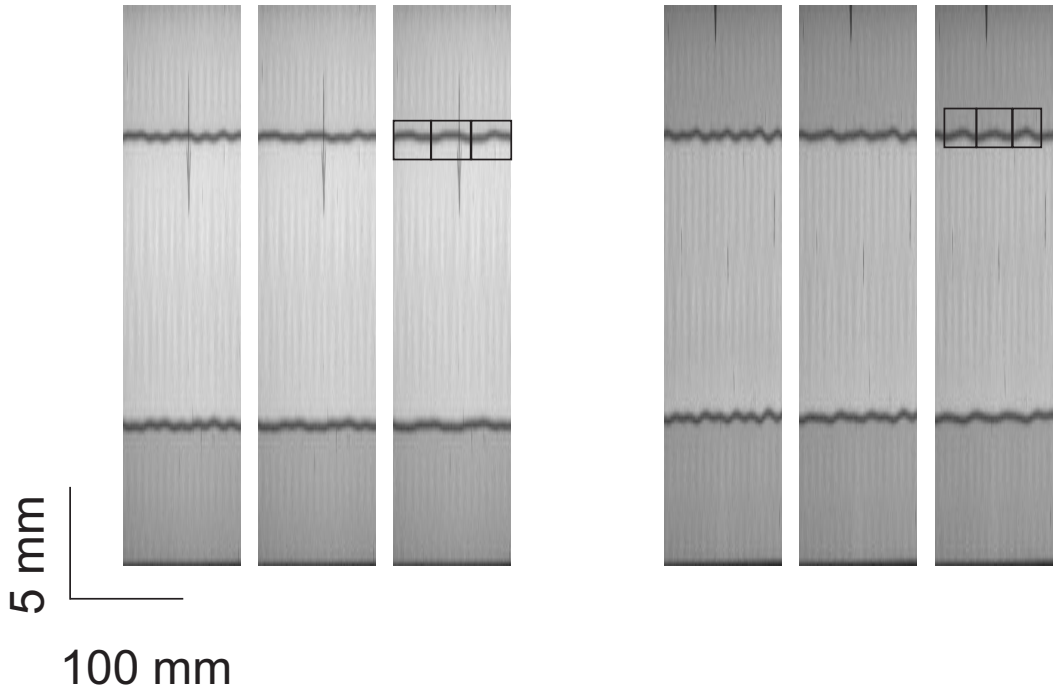

Figure 7.8: Images of the ROI for fingers with a withdrawal velocity $V_\infty = 1.42$ mm/s. The frames are separated 25 s (1/10 of the total duration of the experiment). **Left:** Last stages for a finger in the non stationary response regime ($\nu_{in} = 0.29$ Hz). **Right:** Middle stages of a finger in the selection regime ($\nu_{in} = 0.41$ Hz).

diate times the finger presented a sinusoidal-like response like the one observed for frequencies below $\nu_{fing-min}$. The response frequency was calculated as usual, for the last image presenting a sinusoidal–like profile. The results, shown as inverted black triangles in Fig. 7.3, follow the trend of the results in the frequency dependent regime.

On the other hand, for some of the experimental realizations the sinusoidal-like profile of the fingers evolved into a structure with a much longer wavelength (Fig. 7.8). Although the stationary state was not reached, we can associate a wavelength to the emerging structure and compute the corresponding response frequency. The results, shown as black circles in Fig. 7.3, are consistent with the results found for the stationary states in the selection regime. So the black symbols indicate two things, that a stationary state was not reached and that structures seem to be evolving from shapes characteristic of the frequency dependent regime to shapes characteristic of the selection regime.

In addition, a comparison of the final state observed at these frequencies with the state measured at intermediate times of the selection regime showed that they were equivalent (Fig. 7.8). This points to the possibility that, for longer cells, the final

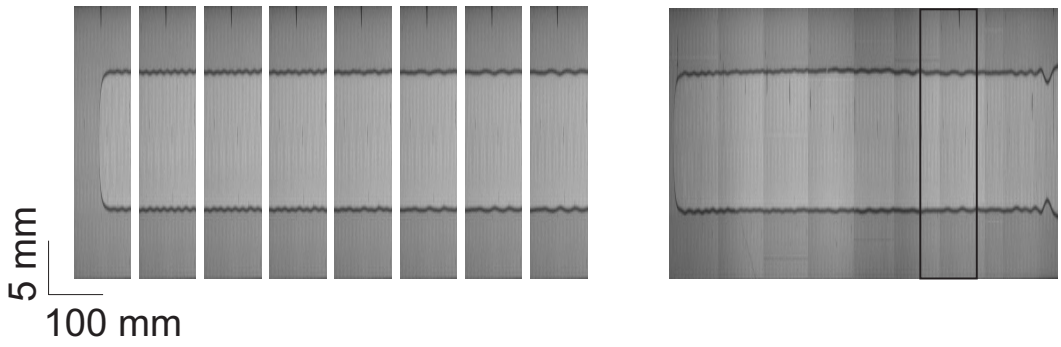

Figure 7.9: Typical fingers for a withdrawal velocity $V_\infty = 1.42$ mm/s in the selection regime ($\nu_{in} = 0.36$ Hz). **Left:** time evolution of the ROI (shown in the long finger at right). The images are separated 25 s (1/10 of the total duration of the experiment). **Right:** picture of a long finger obtained by mounting together several images captured while the CCD camera travelled from the tip of the finger to the air inlet.

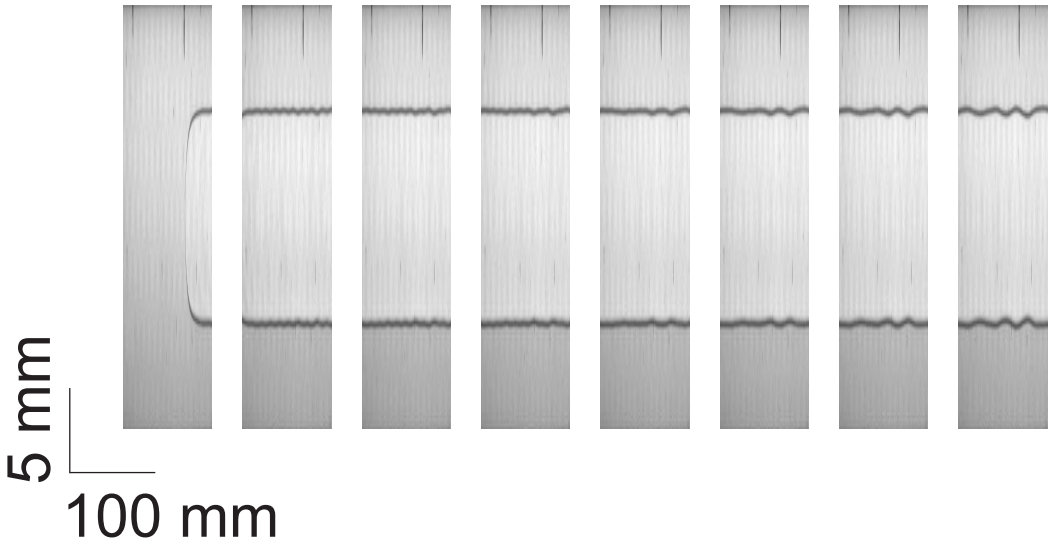

Figure 7.10: Time evolution of the lateral instability for a withdrawal velocity $V_\infty = 1.42$ mm/s in the selection regime ($\nu_{in} = 0.47$ Hz). The frames are separated 25 s (1/10 of the total duration of the experiment).

state reached at these frequencies would be a stationary state of the selection regime.

7.2.3 Selection regime ($\nu_{out} > 1.5\nu_{fing-min}$)

The lateral instability for fingers in the selection regime was strongly dependent on the distance to the finger tip (Figs. 7.9 and 7.10). We could distinguish three different stages in the evolution of the lateral instability:

- **Sinusoidal high frequency response**. Near the finger tip, the interface evolved similarly than in the transient regime. The frequency of the lateral instability at these times was consistent with the one of the transition regime. The second frame in Fig. 7.10 corresponds to this behavior.

- **Destabilitzation of the high frequency profile**. As the finger tip advanced, the high frequency profile presented peak suppression, and the lateral instability evolved to a lower frequency profile. We could not associate a single frequency to this stage of the lateral instability. Frames from 3 to 5 in Fig. 7.10 are good examples of this behavior.

- **Low frequency stationary response**. Very far from the finger tip the sides of the finger presented a periodic modulation with a frequency much smaller than the input frequency. As the finger tip advanced, the new frequency remained constant until the end of the experiment. This frequency was almost independent of forcing frequency. The three last frames in Fig. 7.10 are good examples of the stationary finger profiles in the selection regime.

Although the selected frequency of the lateral instability was not constant with forcing frequency, the finger always evolved to a selected frequency much smaller than the forcing frequency (Fig. 7.3). A fit of the selected frequency gives:

$$\nu_{sel} = (0.077 \pm 0.009) + (0.05 \pm 0.02)\nu_{in}, \tag{7.3}$$

which shows that ν_{sel} increases slightly with ν_{in}.

7.3 Dynamics and saturation distance

As it has been explained before, the instability was born at the finger tip and a wave was propagated far away from the tip as the finger advanced. There was a dynamic process as the wave propagated and, in many cases, the instability reached a stationary state with a wavelength that no longer changed in the course of the experiment.

First, for fingers in the frequency dependent regime the instability was born with a wavelength very close to the one in which the shape saturated. This happened at a distance from the finger tip $d_{sat} \simeq 2.5W$.

Second, for fingers in the selection regime the instability was born with a wavelength much shorter than the one of the stationary state. As the wave propagated far from the tip, this wavelength was unstable and, for some time, it was impossible to

associate a single wavelength to the lateral instability. However, when the wave had travelled even further from the tip, a new wavelength, much larger than the previous one, dominated the pattern. This wavelength evolved rapidly into the stationary one. The distance, d_{sat} at which the shape saturated was nearly constant in all the selection regime and was given by $d_{sat} \simeq 14W$.

Chapter 8

Lateral instability in Saffman–Taylor fingers: Summary and discussion

In our experiments we verified experimentally the destabilization of the flat sides of the Saffman–Taylor finger predicted by simulation results. We observed a low amplitude long wavelength instability both for fingers in a non-homogeneous Hele-Shaw cell and in fingers subjected to periodic driving. Differently from the experiments reported in Refs. [Couder 86; Rabaud 88], all the fingers studied here had a width $\lambda \geq 1/2$.

Both perturbations induced a lateral instability in the initially flat sides of the finger. For fingers periodically driven, this instability was symmetric and periodic, while fingers in cells with non uniform gap spacing developed a non symmetric, non periodic instability.

• **Fingers in cells with quenched disorder**

We studied the effect of the quenched disorder on the lateral instability and we concluded that the main effect was on the amplitude of the instability, which increased as the magnitude of the disorder increased . This explains why the sides of the fingers are flat for typical Saffman-Taylor experiments despite the fact that any experiment has, inevitably, some static noise present in the cell. Another possible explanation is the long wavelength of the lateral instability ($\sim W$) that would require long channels to allow the instability to develop.

On the other hand, the capillary number (or the velocity, in our experiments) had a strong effect on the lateral instability. We observed that the amplitude of the instability decayed as a power law of Ca, at low Ca, and increased for large values of

Ca. This behavior was qualitatively similar to the one observed in Ref. [Moore 02] and was obtained for a low aspect ratio ($W/b \simeq 25$),in contrast with the large aspect ratios explored in Ref. [Moore 02] ($W/b > 50$). Distributions of frequencies at different capillary numbers indicated that the frequency that dominated the lateral fluctuation increased linearly with Ca. Also, the width of the distribution increased with increasing Ca.

• **Fingers subjected to periodic forcing**

The lateral instability observed in periodically driven fingers near the finger tip was symmetric. We observed that Saffman-Taylor fingers responded to periodic forcing by generating a wave on its tip. As the finger advanced, this wave propagated away from the tip towards the finger sides.

At low forcing frequencies the instability quickly reached a stationary state. The response frequency of the stationary state increased monotonically as a function of forcing frequency ν_{in}, up to forcing frequencies of the order of $\nu_{fing-min}$. On the other hand, the ratio ν_{out}/ν_{in} decreased from $\nu_{out}/\nu_{in} \simeq 1$ at low forcing frequencies to $\nu_{out}/\nu_{in} \simeq 0.6$ as the forcing frequency approached the finger characteristic frequency. Also, we observed that for forcing frequencies below the band of frequencies characteristic of the finger, the response frequency was independent of the withdrawal velocity.

An important result was obtained at forcing frequencies larger than any characteristic frequency of the finger. Near the finger tip, the frequency of the lateral instability was consistent with the behavior observed at lower frequencies. As the wave propagated far from the tip, this frequency became unstable and, for some time, the lateral instability presented a non periodic profile. However, at long distances from the finger tip the lateral instability reached a stationary state which was periodic, symmetric and for which $\nu_{out} \ll \nu_{in}$. More details of this regime will be discussed in Sec. 8.2

The lateral instability in fingers forced at some intermediate frequencies over the characteristic finger frequency never reached an stationary state. For these forcing frequencies, the structures observed on the finger sides appear to be evolving from shapes characteristic of the lower frequency regime to shapes characteristic of the highest frequencies. It is possible that, with a longer cell, a stationary state with $\nu_{out} \ll \nu_{in}$ would have been reached. It is also possible that for these forcing frequencies two different response frequencies are equally likely, since we did not observe this shape evolution for all of the experimental realizations.

We also observed that periodic forcing modulated the average finger width in a

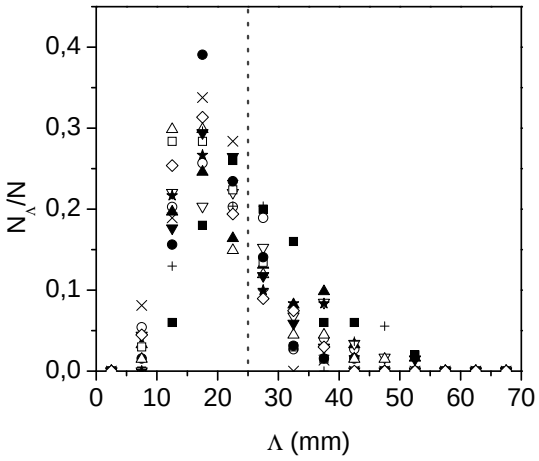

Figure 8.1: Fingers in cells with static disorder: Histogram of the distribution of the wavelength of the lateral instability at different velocities. The symbols are: ■ $1/B = 23$, ○ $1/B = 39$, ▲ $1/B = 63$, ▽ $1/B = 82$, ⋆ $1/B = 118$, × $1/B = 198$, □ $1/B = 254$, ● $1/B = 339$, △ $1/B = 435$, ▼ $1/B = 558$, + $1/B = 925$, ◇ $1/B = 1268$. The vertical dotted line corresponds to the cell width.

non monotonic way. We noticed that the average finger width was always smaller than the steady-state finger width. The amplitude of the lateral instability had also a non monotonic behavior as a function of forcing frequency.

8.1 Wavelength of the lateral instability

Although all the results presented in this work have been explained in terms of the frequency of the lateral instability, it would have been more natural to talk about the wavelength of the lateral instability. Our choice was motivated by the simulation results [Ledesma-Aguilar 05] that we wanted to compare directly with our experiments. In addition, the results of the periodic perturbation experiments are more clear when they are presented in terms of the frequency.

Let us now consider our direct measurements of the wavelength of the lateral instability. A plot of the histogram of the wavelength of the lateral instability in a wide range of withdrawal velocities (Fig. 8.1) provides an interesting result: the wavelength of the lateral instability is almost independent of $1/B$. This result was already shown in Chapter 6, where we observed that the mean frequency of the distribution increased linearly with $1/B$ (the velocity). Given that ν_{out} depends linearly on the mean velocity of the finger ($\nu_{out} = U/\Lambda$) it can be seen that this result is equivalent to the direct measurement displayed in Fig. 8.1. From this result, we

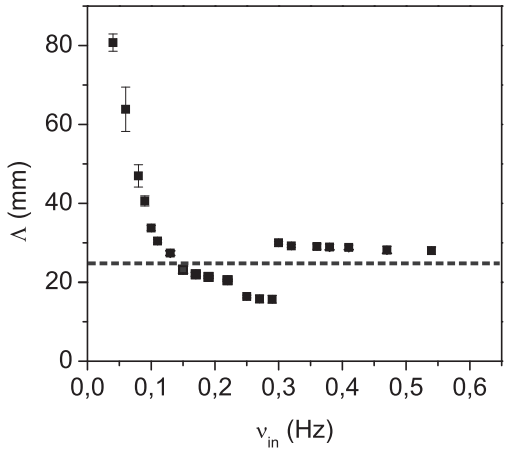

Figure 8.2: Wavelength of the lateral instability of the stationary state in fingers periodically forced as a function of ν_{in} for a withdrawal velocity $V_\infty = 1.42$ mm/s. The horizontal dotted line corresponds to the cell width.

can affirm that W is the relevant length scale of the system (in quenched disorder experiments). Computing the mean wavelength of the distributions we find that is slightly below the channel width for most experiments (only for the lowest velocity it is slightly higher).

Also, we plotted the wavelength of the lateral instability for fingers periodically driven (Fig. 8.2). The selected wavelength is slightly above the channel width for all the frequencies in the selection regime. The selected wavelength is not completely independent of driving frequency, as we observed for the selected frequency. It is interesting to notice that wavelengths much shorter than the channel width were not stable in our system.

8.2 Selection regime

Both in periodic perturbation and in quenched disorder experiments we observed a selection process in which the system selected a particular frequency for the lateral instability. Our results were in good agreement with the simulation results of Ledesma–Aguilar *et al.* [Ledesma-Aguilar 05]. The selected frequency in both series of experiments fell between the two characteristic frequencies of the system.

In quenched disorder experiments the selected frequency corresponds to a wavelenght close to the cell width for all driving velocities.

In fingers subjected to periodic forcing, when the frequency is made dimensionless in terms of ν_{fing} we obtain a selected frequency which is independent of forcing

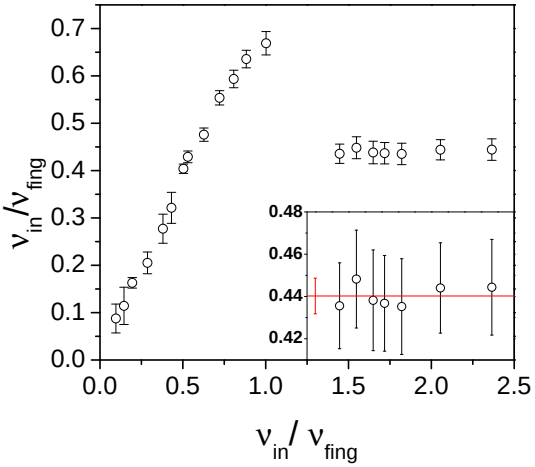

Figure 8.3: Dimensionless selected frequency as a function of dimensionless forcing frequency for a withdrawal velocity of $V_\infty = 1.42$ mm/s. The inbox shows in more detail the selection regime. The average dimensionless selected frequency is given by the red line.

frequency (Fig. 8.3) in a wide range of forcing frequencies. The result is:

$$\nu_{sel} = (0.440 \pm 0.008)\nu_{fing}. \tag{8.1}$$

This linear relation between ν_{sel} and ν_{fing} points to the fact that finger width λW and the mean finger tip velocity U are the relevant parameters of the periodically driven lateral instability. The other natural frequency of the system, ν_∞, does not play a relevant role in the selection process for fingers under periodic forcing.

Chapter 9

Oscillating flow of a Maxwell fluid in a tube: Background

Coupling between flow and liquid structure makes the dynamic response of non–Newtonian (complex) fluids much richer than that of Newtonian (simple) fluids [Gelbart 96; Larson 99]. In particular, depending on the relevant time scale of the flow, viscoelastic fluids exhibit the dissipative behavior of ordinary viscous liquids and the elastic response of solids. Due to their elastic properties, these fluids are potential candidates to exhibit interesting resonance phenomena under different flow conditions.

In this respect, the response of a viscoelastic fluid to an oscillatory pressure gradient has been analyzed theoretically in some detail (see Sec. 3.3.2 for details). The response, measured in terms of the velocity for a given amplitude of the pressure gradient, exceeds that of an ordinary fluid by several orders of magnitude at a number of resonant frequencies. The remarkable enhancement in the dynamic response of the viscoelastic fluid is attributed to a resonant effect due to the elastic behaviour of the fluid and the geometry of the container [López de Haro 96; del Río 98; Tsiklauri 01].

In Ref. [Castrejón-Pita 03b] Laser Doppler Anemometry (LDA) measurements were used to study the response of a Maxwell fluid to an oscillatory pressure gradient (measured by the flow velocity at the the tube axis, for a given amplitude of the pressure gradient). They observed that the dynamic response exhibited very large resonance peaks at particular driving frequencies while a purely dissipative behavior was observed for a Newtonian fluid. However, the linear model (Eq. (3.18)) had several interesting predictions which were still open. For instance, the shape of the velocity profiles was not measured, as the experimental study performed in Ref. [Castrejón-Pita 03b] was focused on the dynamic response at the tube axis.

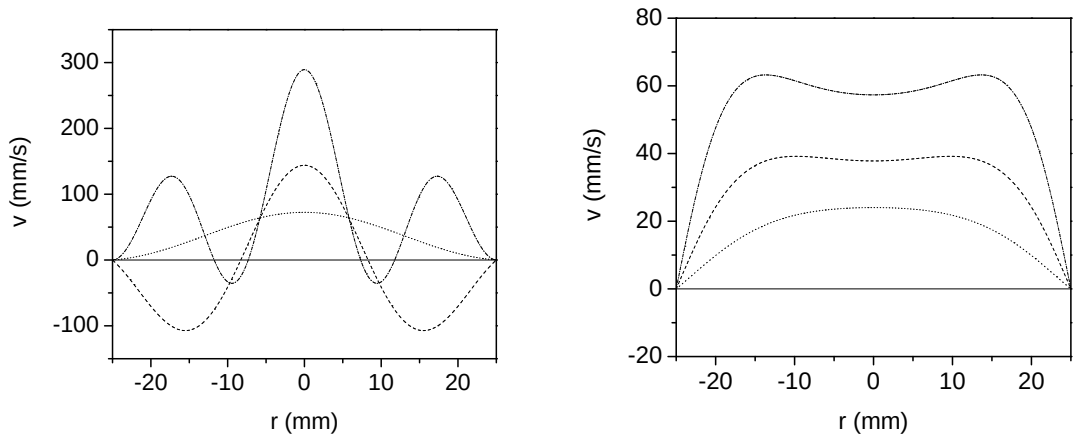

Figure 9.1: Left: Theoretical velocity profiles for a Maxwell fluid with $\eta = 60$ Pa·s, $\rho = 1050$ kg/m^3, $t_m = 1.8$ s in a tube of radius $a = 25$ mm. **Right:** Theoretical velocity profiles for a Newtonian fluid with $\eta = 1$ Pa·s, $\rho = 1250$ kg/m^3 in a tube of radius $a = 25$ mm. Three different driving frequencies are displayed for each fluid: 4 Hz (dots), 7 Hz (dash) and 11.5 Hz (dash-dot).

A natural extension of the characterization of the flow was the study of the stability of the laminar flow. We were interested in explore experimentally in which ways the basic parallel shear flow described in Sec. 3.18 became unstable as the fluid was subjected to a harder oscillatory driving, by increasing the forcing amplitude and/or the forcing frequency. We focused on driving frequencies that corresponded to either maxima or minima of the viscoelastic fluid response. In all instances the Reynolds number remained very small ($\mathrm{Re} < 10^{-1}$), ensuring that the increasing complexity of the flow (in the case of the viscoelastic fluid) was due to the rheological properties of the fluid, not to inertial effects.

In this Chapter, we will present the main objectives of our experimental study: the full characterization of the laminar velocity profiles as well as the stability of the complex oscillating flow.

9.1 Laminar flow velocity profiles

The linear model presented in Sec. 3.18 predicts velocity fields which depend on the radial position (Fig. 9.1):

$$v(r,t) = -i\omega z_0 \left(1 - \frac{J_0(\beta r)}{J_0(\beta a)}\right) e^{i\omega t}, \tag{9.1}$$

$$\beta = \sqrt{\frac{\rho}{\eta t_m}\left((\omega t_m)^2 + i\omega t_m\right)}. \tag{9.2}$$

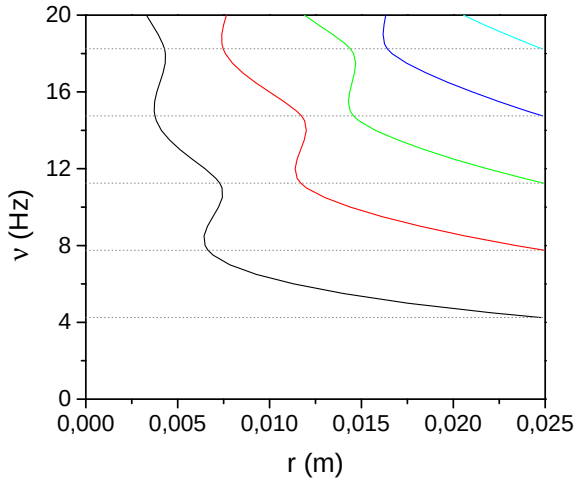

Figure 9.2: Diagram showing the theoretical location of the quiescent flow points along the radial coordinate of the cylinder, r, as a function of driving frequency, ν, for a Maxwell fluid. The dashed horizontal lines separate the frequency axis in intervals of constant number of quiescent flow points. For calculations the parameters for the Maxwell fluid were $\eta = 60$ Pa·s, $t_m = 1.8$ s and $\rho = 1050$ kg/m^3, the radius of the tube was $a = 25$ mm.

For a Newtonian fluid ($t_m = 0$) there is only one node of the velocity profile, at $r = a$, which accounts for the non–slip condition at the wall. Remarkably, if $t_m \neq 0$ (Maxwellian fluid) the velocity profile may present several nodes. These nodes define quiescent points of the flow. For given material and geometrical parameters, the location of the nodes depends on the driving frequency (Fig. 9.2). At low frequencies the profiles have only a pair of quiescent flow points at the tube walls. As driving frequency increases, quiescent flow points detach from the tube wall and approach the tube axis. Thus, the 3–d flow is structured in cylinders of alternating upward/downward motion separated by quiescent flow cylindrical surfaces.

The linear model is calculated for an infinite fluid column and does not consider the effect of the fluid-air interface. As a result, there is no dependence on the z-coordinate for the velocity profiles. But real systems are finite and the effect of a fluid-air interface can be important. An approximation of the shape of the interface can be calculated from the linear model if oil–air/maxwell fluid–air surface tension is neglected. The position of a fluid volume element in the tube is obtained by time integration of Eq. 9.2, and corresponds to the real part of:

$$h(r,t) = h_0 + \delta_h(r,t) = h_0 - z_0 \left(1 - \frac{J_0(\beta r)}{J_0(\beta a)}\right) e^{i\omega t}, \tag{9.3}$$

where we have already considered that the velocity profile is independent of the vertical position z in the tube. Since the position of a fluid volume element can be

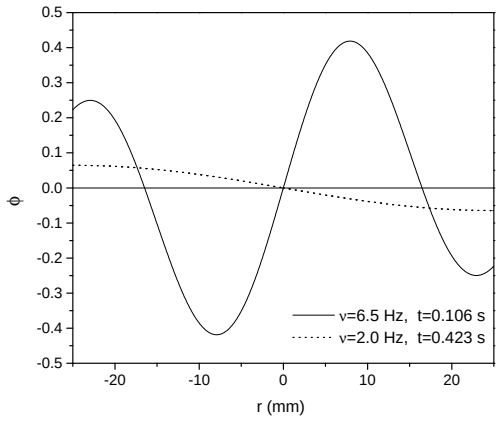

Figure 9.3: Theoretical deformation profiles for a Maxwell fluid driven at 2 Hz (dashed line) and at 6.5 Hz (solid line). For calculations the parameters for the Maxwell fluid were $\eta = 60$ Pa·s, $t_m = 1.8$ s and $\rho = 1050$ kg/m^3, the radius of the tube was $a = 25$ mm, and the amplitude of the driving was $z_0 = 0.8$ mm.

described by Eq. 9.3 for any vertical position, the shape of the fluid–air interface $h_i(r,t)$ is also described by $h(r,t)$.

In our experiments, we could measure the deformation profiles of the interface ϕ_i by means of an optical technique (Optical Deflectometry, described in Ch. 10). These deformation profiles are related to the shape of the interface as $\phi_i = \partial h_i(r,t)/\partial r$. The linear model provides us with a theoretical prediction of the deformation profiles in the bulk of the flow (which in absence of fluid–air surface tension would correspond to the deformation profiles of the interface) $\phi = \partial h(r,t)/\partial r$. The theoretical predictions for a Maxwell fluid in a tube for two different driving frequencies and the same driving amplitude are displayed in Fig. 9.3. The profiles are very different. While the deformation profile at 2 Hz is monotonic and very smooth, the profile at 6.5 Hz shows a more complex behavior: instead of a single central node, it presents three nodes which, in the velocity profile, correspond to a maximum at the tube center and a minimum near the tube wall. The maximum deformation between these nodes corresponds to an inflection point of the velocity profile, very close to the quiescent flow point.

9.2 Hydrodynamic instabilities

A natural extension of the characterization of the laminar flow is to explore experimentally in which ways the basic parallel shear flow generated at low driving amplitudes is distorted, as the fluid is subjected to a harder oscillatory forcing by

increasing its amplitude and/or its frequency.

This experimental study can be compared with the study performed in Refs. [Hino 76; Eckmann 91] on the transition to turbulence in an oscillatory pipe flow. The onset of the instability occurs at values of the Reynolds number around $\mathrm{Re}_{osc} \sim 700$, a value which is $\ll$ Re in the stationary unidirectional Poiseuille flow [Drazin 02]. However, $\mathrm{Re}_{osc} \gg 1$, indicating that inertial forces are necessary to the destabilization of the flow. Both stationary and oscillatory flows are laminar for values of the Reynolds number for which inertial forces are comparable to viscous dissipative forces.

We are more interested in the study of the stability of the flow at $\mathrm{Re} < 1$. In this regime, the Newtonian flow is stable [Hino 76] but the viscoelastic flow may be unstable. This study is important in the field of elastic instabilities [Arora 02; Groisman 98; Groisman 00]. As described in Section 3.3.1, although parallel shear flows of viscoelastic fluids are acknowledged to be linearly stable [Pakdel 96], Morozov and van Saarloos have demonstrated very recently that plane Couette flow undergoes a purely elastic subcritical instability, by which a small finite–size perturbation is sufficient to create a secondary flow [Morozov 05]. The oscillatory flow of the viscoelastic–fluid–pipe system is a parallel shear flow in which shear stresses accumulate near the quiescent cylindrical boundaries and, as such, it is a promising candidate to exhibit the same kind of nonlinear elastic instability.

The flow of a Maxwell fluid (viscosity η, density ρ, Maxwell time t_m) in a tube (radius a) under periodic driving (frequency ν, amplitude z_0) is characterized by the dimensionless numbers:

- Reynolds number: $\mathrm{Re} = \rho 2\pi\nu z_0 a/\eta$. The maximum velocity of the piston $2\pi\nu z_0$ is chosen characteristic velocity and the radius of the tube a is the characteristic length scale. It is necessary to work at $\mathrm{Re} \ll 1$ according with the assumptions of the linear model, where inertial terms are neglected.

- Deborah number: $\mathrm{De} = t_m\eta/(a^2\rho)$. Where the characteristic time of the fluid is compared to the characteristic dissipation time scale. In order to observe elastic effects, it is necessary to set $\mathrm{De} \gg 1$. The amplitude of the resonant peaks of the dynamic response is actually a function of De

- Weissenberg number: $\mathrm{Wi} = t_m\dot{\gamma}$. This is the usual definition for Weissenberg number. As characteristic fluid time we select the Maxwell time of the fluid. The characteristic shear rate for the oscillating flow in the tube is defined a ratio between a characteristic velocity (the maximum velocity of the piston) and a characteristic length scale for variations in the velocity profile (the distance r_q

between the tube axis where the velocity is maximum and the first quiescent point of the flow where the velocity is zero):

$$\dot{\gamma}_{char} \equiv \frac{2\pi\nu z_0}{r_q}. \tag{9.4}$$

The resulting Weissenberg number is $\mathrm{Wi} = \frac{2\pi\nu t_m z_0}{r_q}$.

- Stokes parameter: For an oscillatory viscous flow in a tube, the Stoke's parameter measures the ratio of the tube radius to the viscous penetration depth $\Lambda = a/\delta_\nu$, where $\delta_\nu = \sqrt{\eta/(\rho\pi\nu)}$. [Hino 76].

The experimental device used in the experiments is described in Ch. 10 and the main results for the laminar profiles and the hydrodynamic instability are presented in Ch. 11 and 12. We will finish with a dicussion presented in Ch. 13.

Chapter 10

Oscillating flow of a Maxwell fluid in a tube: Experimental methods

In order to characterize the velocity fields of Maxwell and Newton fluids in a tube, we used three different techniques: Optical Deflectometry, Particle Image Velocimetry and Birefringence. In this Chapter we will describe these techniques and we will also present the experimental device we used in the experiments with complex fluids.

10.1 Techniques used

10.1.1 Optical Deflectometry (OD)

Optical Deflectometry is a technique commonly used to measure deformations of the surface of transparent thin films [Fermigier 92]. However, for small surface deformations, the technique can be used to measure deformations in the surface of transparent fluids, not necessarily thin films.

This technique can be understood by means of simple optics laws. When a light ray crosses perpendicularly a flat interface separating two media it is not deviated. As the interface is deformed, the incident ray does not enter the interface perpendicularly anymore (Fig. 10.1). As a consequence, the ray will be deviated from its initial trajectory when entering the new medium. The displacement of this ray allows measuring the local slope of the interface, from which the deformations of the interface between both media can be calculated.

In our case we used a liquid column as a variable–thickness lens. In the bottom part of the liquid column we placed a plastic sheet with a regular array (grid spacing $d = 5.0$ or 5.5 mm). The grid was imaged trough the liquid column using a CCD

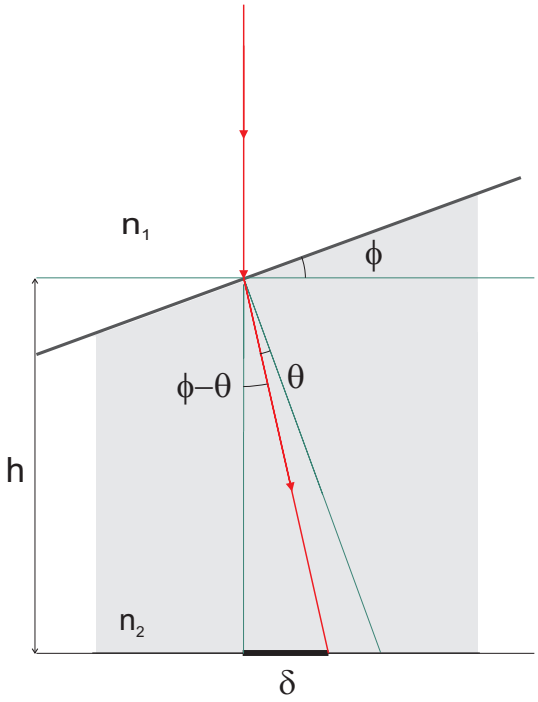

Figure 10.1: Sketch of the path followed by a light ray in the system.

camera (640 × 480 pixels) placed on top of the column (Fig. 10.2). As the fluid-air interface was distorted, each point was displaced a certain distance $\delta(x, y)$ of its initial position, depending on the slope of the interface $\phi(x, y)$ (Fig. 10.1). An example of the recorded deformations is displayed in Fig. 10.3.

The relation $\phi(\delta)$ was obtained by simple optical relations. According to Snells' refraction law for small angles $n_1\theta = n_2\phi$. From Fig. 10.1 it is clear that:

$$\tan(\phi - \theta) = \frac{\delta}{h}. \tag{10.1}$$

Therefore, the relation between ϕ and δ reads:

$$\phi = \frac{1}{1 - n_2/n_1} \arctan\left(\frac{\delta}{h}\right). \tag{10.2}$$

In our setup the height of the liquid column ($H = 240$ mm) was much larger than the local height variations produced by the deformation of the interface (of the order of mm), and we could safely take $h \simeq H$ in Eq. (10.2).

As Eq. (10.2) shows, deflection of the points of the grid increased with the depth of the layer. This increases the resolution of the measurement, but is also limiting the use of the technique to smooth interfaces. For highly deformed interfaces, the image of different points of the grid can mesh or strongly deform the points.

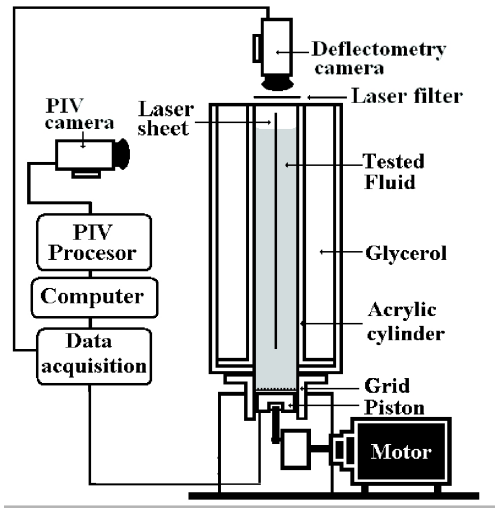

Figure 10.2: Scheme of the experimental device used in OD measurements.

Experimental procedure and data analysis

We used grid spacings of $d = 5.0$ and 5.5 mm. The refractive indices of our materials were $n = 1.33407(01)$ for Maxwell-A fluid (measured by Abbé refractometry), and $n = 1.473$ for glycerol (nominal).

Once the deformation map $\pi(x, y.t)$ of the interface was obtained, we averaged it in the azimuthal direction, considering that the flow preserved axial symmetry. Thus, from the initial map $\phi(x, y, t)$, we obtained the deformation profile of the interface $\phi(r, t)$. This profile could be simply related to the local height of the column by $\phi(r, t) = \partial h(r, t)/\partial r$. Hence:

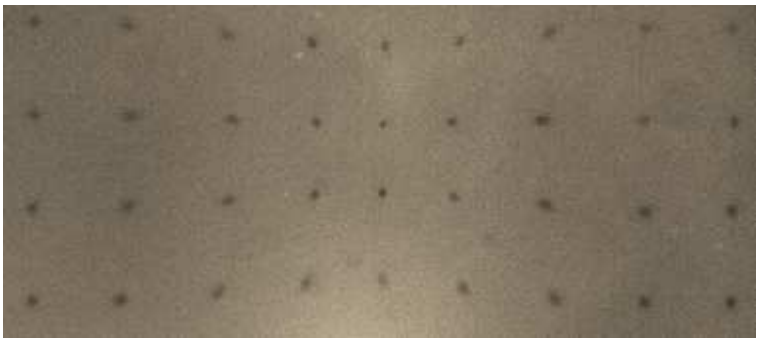

Figure 10.3: A typical picture recorded in Optical Deflectometry measurements. The image of a regular array of black dots (grid spacing $d = 5.0$ mm) is distorted by the interface deformation.

$$h(r,t) = h(r_0,t) + \int_{r_0}^{r} \phi(r,t)\, dr. \tag{10.3}$$

We chose for r_0 a position where the interface was motionless, because the reference height $h(r_0,t)$ was then a constant taken equal to 0.

Finally, the velocity profile of the interface was obtained from the time derivative of the local height, $v(r,t) = \partial h(r,t)/\partial t$. For the numerical calculation of the time derivative at time t we used the height profiles at three time phases (t_-, t and t_+):

$$v(r,t) = \frac{h(r,t_+) - h(r,t)}{t_+ - t} + \frac{h(r,t) - h(r,t_-)}{t - t_-} - \frac{h(r,t_+) - h(r,t_-)}{t_+ - t_-}. \tag{10.4}$$

10.1.2 Particle Image Velocimetry (PIV)

PIV is a non intrusive measurement technique used to study flows in transparent fluids, and it can be used for flows in a wide range of velocities. A detailed description of the technique can be found at Ref. [Adrian 91]. The following is a simple explanation of the technique. Naively, the technique consists on identifying the motion of fluid particles with the motion of density–matched seeding particles in the fluid.

PIV systems capture pairs of images of the seeding particles. From one pair of images, a flow velocity map is generated. The procedure is simple. For a pair of images A and B, the images are divided in interrogation subareas l_A and l_B. These subareas must be small enough to provide a detailed flow map and large enough to contain several seeding particles (typically > 10 [Adrian 91]). In our experiments the size of the subareas was around 16×16 pixels (1 cm^2). The interrogation areas of each image are cross-correlated pixel by pixel:

$$C(\mathbf{s}) = \int\int l_A(\mathbf{x}) l_B(\mathbf{x}+\mathbf{s}) d\mathbf{x}, \tag{10.5}$$

where $\mathbf{s}$ is a two–dimensional vector. The correlation produces a peak for a given displacement vector $\mathbf{s}$. This displacement vector is associated with the displacement of all the particles of the interrogation subarea l_A. The velocity associated to the interrogation subarea l_A is calculated as follows:

$$\mathbf{v} = \frac{\mathbf{s}}{\Delta t}, \tag{10.6}$$

where Δt is the time between images in a pair.

The size of the interrogation area ($d_A \times d_A$) and the time between images in a pair (Δt) are related, and strongly depend on the experiment we are performing.

The highest velocity measurable in an experiment will be clearly smaller $d_A/\Delta t$. This constraint combined with the spatial resolution that we require for each experiment, will guide the choice of d_A and Δt.

Experimental procedures and data analysis

The measurements were performed in an interrogation plane of 50 $\times$ 50 mm, at different distances from the neutral position of the fluid-air interface. In all cases this distance was far enough from both the fluid–air interface (top) ant the piston (bottom) to ensure that the flow in the interrogation plane did not felt the proximity of these two discontinuities.

The 2d PIV technique provided only the two in–plane components of the actual 3d velocity field in the interrogation plane, in a vertical section of the tube. This information was complete only if the velocity field was contained within the interrogation plane and the flow was axisymmetric. We investigated whether this was the case in our experiments by checking whether the velocity field in the interrogation plane satisfied $\vec{\nabla} \cdot \vec{v} = 0$ (within experimental error), meaning that the velocity component perpendicular to the interrogation plane was negligible. The background (zero) level of $\vec{\nabla} \cdot \vec{v}$ was determined by the laminar base flow, for which the radial and azimuthal components of $\vec{v}$ are 0 and the vertical component of $\vec{v}$ depends only on the radius.

Velocities measured in cartesian coordinates (x, y, v_x, v_y) are mapped into cylindrical coordinates ($rcos(\theta)$, z, $v_r cos(\theta)$, v_z). For an interrogation plane passing for the axis of the tube the relation is very simple: ($\pm r$, z, $\pm v_r$, v_z) . For convenience,we will use v_x and v_y.

The analysis of the velocity maps was automatized with an algorithm written in C^{++} for this purpose. We were interested mainly in the evaluation of the fluctuations, the vorticity map of the flow, and the correlations in the radial component of the velocity.

An integrated measure of the destabilization of the basic laminar flow can be obtained by the rms fluctuations of the x and y components of the velocity along the vertical direction. We define:

$$\sigma_{v_x}(x,t) = \sqrt{\frac{1}{N}\sum_i [v_x(x,y_i) - \overline{v_x}(x)]^2}, \tag{10.7}$$

$$\sigma_{v_y}(x,t) = \sqrt{\frac{1}{N}\sum_i [v_y(x,y_i) - \overline{v_y}(x)]^2}, \tag{10.8}$$

where $\overline{v_x}(x)$, $\overline{v_y}(x)$ correspond to the velocity components averaged along the vertical (y) direction and N to the number of velocity measurements in the interrogation plane

along the vertical direction. To make the rms fluctuations comparable for different magnitudes of the forcing we make them dimensionless in the form:

$$\widetilde{\sigma}_{v_x}(x,t) = \frac{\sigma_{v_x}(x,t)}{2\pi\nu z_0} \tag{10.9}$$

$$\widetilde{\sigma}_{v_y}(x,t) = \frac{\sigma_{v_y}(x,t)}{2\pi\nu z_0} \tag{10.10}$$

The time dependence of the velocity fluctuations is computed by averaging $\widetilde{\sigma}_{v_x}(x,t)$ and $\widetilde{\sigma}_{v_y}(x,t)$ along the radial direction x. Similarly, the spatial dependence of the velocity fluctuations is computed by averaging $\widetilde{\sigma}_{v_x}(x,t)$ and $\widetilde{\sigma}_{v_y}(x,t)$ in a time period.

In order to study the destabilization of the laminar base flow by the generation of vortices, we calculate the azimuthal (θ) component of the vorticity. It is easy to check that the calculation of the azimuthal component of the velocity is the same in cylindrical than in cartesian coordinates:

$$w = \frac{\partial v_x}{\partial y} - \frac{\partial v_y}{\partial x}. \tag{10.11}$$

10.1.3 Birefringence

Birefringence or double refraction is an optical property of some anisotropic materials. In anisotropic materials the speed propagation of a light wave is a function of the direction of propagation and the polarization of the light. When a ray of light enters a birefringent medium, it splits in two different rays linearly polarized, and with orthogonal polarizations. If the material is uniaxial (has a single anisotropy axis), we can describe birefringence by associating a refractive index to each polarization: n_O and n_E. The ordinary refractive index n_O corresponds to the wave which propagates following Snell's law, and has a polarization perpendicular to the anisotropy axis. The extraordinary refractive index n_E corresponds to the wave with a polarization parallel to the anisotropy axis. Birefringence can be quantified by the difference between both refractive index: $\Delta n = n_O - n_E$.

Stress induced birefringence

Some isotropic materials subjected to mechanical stresses become optically anisotropic and thus birefringent. This is the so called stress induced birefringence, the effect observed in our experiments. The relation between the stresses and the birefringence can be expressed in terms of the stress-optic law [Lerouge 00]:

$$\Delta n \propto \sigma_1 - \sigma_2, \tag{10.12}$$

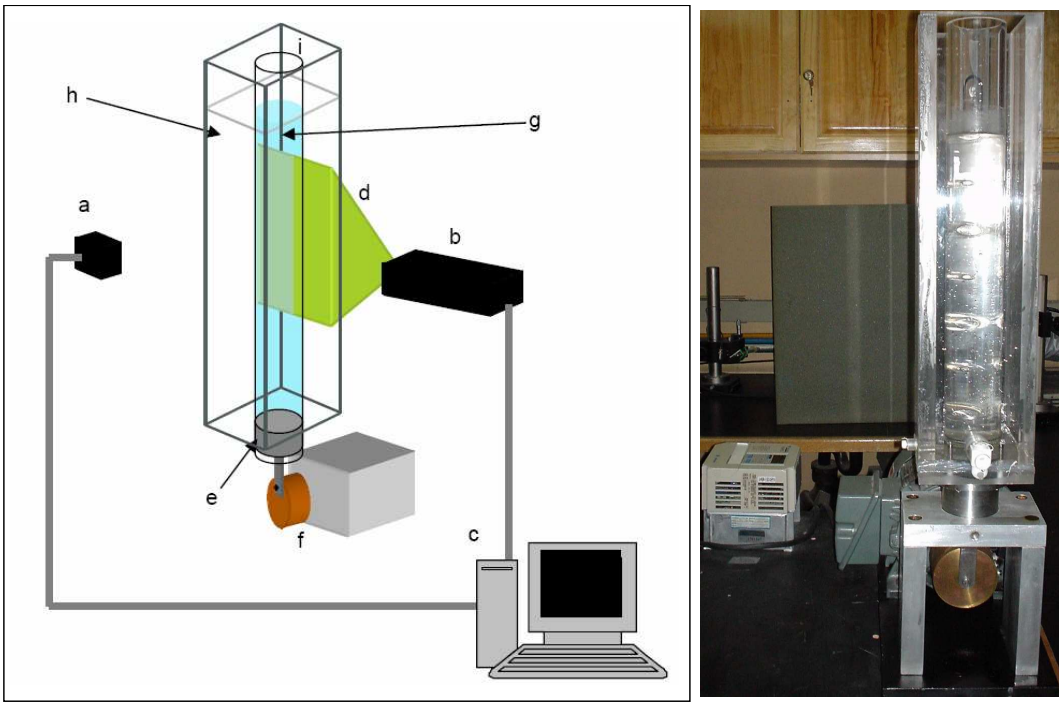

Figure 10.4: Left: PIV system scheme: (a) PIV camera, (b) PIV laser, (c) PIV processor, (d) laser sheet, (e) teflon piston, (f) motor, (g) test fluid, (h) glycerol, (i) acrylic cylinder. **Right:** Picture of the actual experimental device.

where σ_i are the principal stresses at a point in the material.

10.2 Experimental setup

The experimental device (Fig. 10.4) consisted on a vertical cylinder made of transparent acrylic, of inner radius $a = 25$ mm and height 500 mm, filled with the test fluid. In order to avoid optical aberrations, this cylinder was placed inside a second recipient of transparent acrylic, of square section, filled with glycerol to match the refractive index of the acrylic walls. A Teflon piston at the bottom end of the cylinder, driven by a motor of variable frequency, produced harmonic oscillations of the pressure gradient in the liquid column. The amplitude of the oscillation could be modified by changing the eccentricity of the driving wheel. Amplitudes of $z_0 = 0.8, 1.2, 1.6, 2.0,$ and 2.5 (± 0.05) mm were studied.

The velocity fields in a vertical plane, along the symmetry axis of the tube, were measured by 2d particle imaging velocimetry (PIV) [Adrian 91]. Our PIV system contained a two pulsed Nd-YAG laser unit, that included an optical array to produce a laser light sheet in a vertical plane of the acrylic cylinder (Fig. 10.4). A CCD

camera (Kodak E1.0, spatial resolution 1008 × 1016 pixels), perpendicular to the laser light sheet, was used to record the digital images. The camera recorded two consecutive frames, one corresponding to each laser light pulse. The acquisition rate was limited by the camera to three pairs of images every two seconds (1.5 Hz). A *Dantec FlowMap 1100* processor took care of the synchronization between the laser pulses and the camera trigger. Post–processing of the data, to determine velocity maps, was carried out by the *Dantec FlowMap v5.1* software. *Dantec* 20–μm polyamid spheres were used as seeding particles in all the experiments. These particles were small enough to follow the flow with minimal drag, but sufficiently large to scatter enough light to obtain good particle images.

This experimental setup was designed to measure the dynamic permeability of a Maxwell fluid under periodic forcing [Castrejón-Pita 03a; Castrejón-Pita 03b]. We performed new series of measurements using three different techniques: Particle Image Velocimetry (PIV), Optical Deflectometry (OD) and Birefringence. These measurements required slight modifications of the original setup:

- Simultaneous measurement of bulk and interface velocity profiles (PIV and OD).

  The simultaneous measurements of PIV and OD were performed in perpendicular sections of the tube. In OD measurements the illumination consisted on white light. PIV required laser illumination; we used a laser which emitted in the green band. In the OD pictures, laser illumination produced a bright band in the center of the tube. To avoid this effect, we placed an orange optical filter on top of the tube and suppressed the bright central band. For these experiments, the height of the fluid column was approximately 240 mm.

- Destabilization of the periodic flow (PIV and Birefringence).

  Some of these experiments were performed with a polarizer placed between the PIV camera and the measurement area. By this simple modification of the experimental device we eliminated noise in the PIV images and, in addition, we visualized birefringence bands in the measurement area.

10.3 Fluid properties

In our experiments we used several fluids: silicone oil, glycerol and viscoelastic surfactant solutions. A summary of the main properties is shown in Table 10.1.

Fluid	ρ (kg/m^3)	η (Pa·s)	t_m (s)
Silicone Oil	973	56	—
Glycerol	1250	1	—
Maxwell-A	1050	60	1.9
Maxwell-B	1005	30	1.25

Table 10.1: Summary of the physical properties of the fluids used in the experiments. ρ : density, η : viscosity, t_m : Maxwell relaxation time.

The Newtonian fluids used in these experiments (Silicone Oil and Glycerol) were used as test fluids, to compare the behavior of Newtonian fluids with the behavior of maxwelian fluids. We used the nominal values of their material parameters as the correct ones.

The viscoelastic solutions were prepared by solving Cetylpiridinium Chloride (CPyCl) and Sodium Salicylate (NaSal) (both from Sigma) in distilled water. The solutions were left on a dark chamber for three days. Most of the experiments were performed using CPyCl/NaSal [100/60] mM (Maxwell-A). The others used a solution of CPyCl/NaSal [40/40] mM (Maxwell-B).

The complete rheological characterization of fluid Maxell-A is presented in Appendix A.

Chapter 11

Laminar regime

In this chapter and newt, our results for the oscillating flow of a Maxwell fluid in a tube are presented. The behavior of a Maxwell fluid and that of a Newtonian fluid showed dramatic differences. These differences were observed in the laminar velocity profiles (Sections 11.2 and 11.3) and in the destabilization of the laminar flow (Chapter 12).

We studied the velocity profiles of the Maxwell-a viscoelastic fluid at driving frequencies that coincided with the three first maxima of the dynamic response of the system (Eq. 9.2): 2.0, 6.5 and 10.5 Hz. Some of the measurements were also carried out for the three first minima of the dynamic response of the system: 3.5, 8.2 and 11.5 Hz.

In our experiments we also varied the driving amplitude. It is important to mention the range of relevant dimensionless numbers in our measurements:

- **Reynolds number**. For the values of ν and z_0 explored in the present experiments Re was very small, in the range $4 \cdot 10^{-3}$ to $8 \cdot 10^{-2}$, ensuring that inertia was not responsible for the destabilization of the basic flow. If the decrease in η due to shear thinning was taken into account, Re increased about two orders of magnitude but remained much smaller than the critical value for which a Newtonian fluid would show an unstable flow [Hino 76].

- **Deborah number**. In our case De $= 174 \gg 1$, so that elasticity of the viscoelastic fluid was important enough for resonances to occur. The decrease in η due to shear-thinning led still to a minimum De$\gg$1.

- **Weissenberg number**. For the experiments reported, Wi lied between 0.7 and 60.

- **Stokes parameter**. For all the experiments reported here $\Lambda < 2$. That means that all the flow is influenced by the tube wall, i.e. viscous oscillatory boundary layers occupy all the tube.

For all the driving frequencies the PIV acquisition rate was very low compared to the driving frequency. Actually, we could not acquire a significative number of image pairs in a single oscillation period for none of the driving frequencies. In practice, we acquired pairs of images at the maximum affordable rate. Time series were generated by folding PIV measurements back to the first period during data post processing. This strategy optimised the temporal resolution of our experiments within a driving period, assuming that the flow followed exactly the periodicity of the driving, and it was adopted in all the PIV and OD measurements presented in this chapter.

11.1 Dynamic permeability for different Maxwell fluids

The amplitude of the velocity field given by the linear model presented resonance peaks at several resonance frequencies. As mentioned, this phenomenon was demonstrated experimentally and compared to the purely dissipative behavior of a Newtonian fluid in Ref. [Castrejón-Pita 03b]. These results showed that the linear theory gave a good prediction of the resonance frequencies but overestimated the amplitude of the resonance peaks.

We repeated this same kind of measurements, to check the dependence of the resonance frequencies on the rheological properties of the Maxwell fluid. To this purpose the driving frequency ω was made dimensionless by a characteristic time τ. This characteristic time was related to Deborah number:

$$\tau \propto t_m De^{-\frac{1}{2}}. \tag{11.1}$$

As it was shown in Ref. [del Río 98], the location of the resonance peaks became universal (independent of fluid parameters and system dimensions) if ω was made dimensionless in the form $\omega\tau$.

Then, we rewrited Eq. (9.2) in the form

$$V(r,\omega) = \xi(r,\omega)\frac{dP}{dz}, \tag{11.2}$$

and we plotted the dimensionless response function $\xi(r,\omega)/\xi(r,0)$ as a function of the dimensionless driving frequency $\omega\tau$. The results at the center of the tube ($r = 0$), for

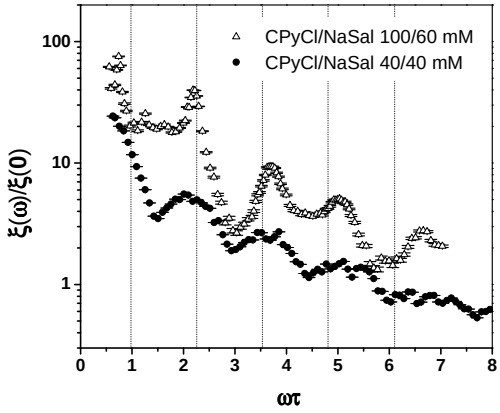

Figure 11.1: Dimensionless response function at the centre of the cylinder, as a function of dimensionless driving frequency, for two concentrations of the CPyCl/NaSal solution. The vertical dashed lines give the location of the resonance frequencies predicted by a linear theory.

the two different concentrations of the CPyCl/NaSal solution used, are shown in Fig. 11.1. Comparison with the linear theory is given by the vertical dashed lines, which give the resonance frequencies corresponding to maxima of $\xi(r = 0, \omega)$. The figure shows that the dimensionless frequency $\omega\tau$ suggested by the linear theory leads to a satisfactory reproducibility of the resonance frequencies independently of viscoelastic fluid parameters.

The magnitude of the response function at the resonance peaks for the surfactant solution of concentration 100/60 (Maxwell-a) was considerably lower in our measurements than in the previous ones of Ref. [Castrejón-Pita 03b]. The reason was that the reported measurements were carried out at 6 cm of the free air–liquid interface, while the previous ones had been taken at 10 cm. The different measured velocities provided a first evidence of the damping influence of the free interface on the flow.

11.2 Deflection of the air–liquid interface

The results obtained by Optical Deflectometry for a forcing amplitude of $z_0 = 0.8$ mm are presented on top of Figs. 11.2 (2.0 Hz), and 11.3 (6.5 Hz). We performed measurements also at 10 Hz. These measurements are not shown because, at this driving frequency, the deformations of the free interface of the Maxwellian fluid were so large that the technique was not applicable. Each figure displays measurements at two different time–phases.

The experimental deformation profiles of the interface at 2.0 and 6.5 Hz (top of Figs. 11.2 and 11.3) for the viscoelastic fluid can be compared to the theoretical

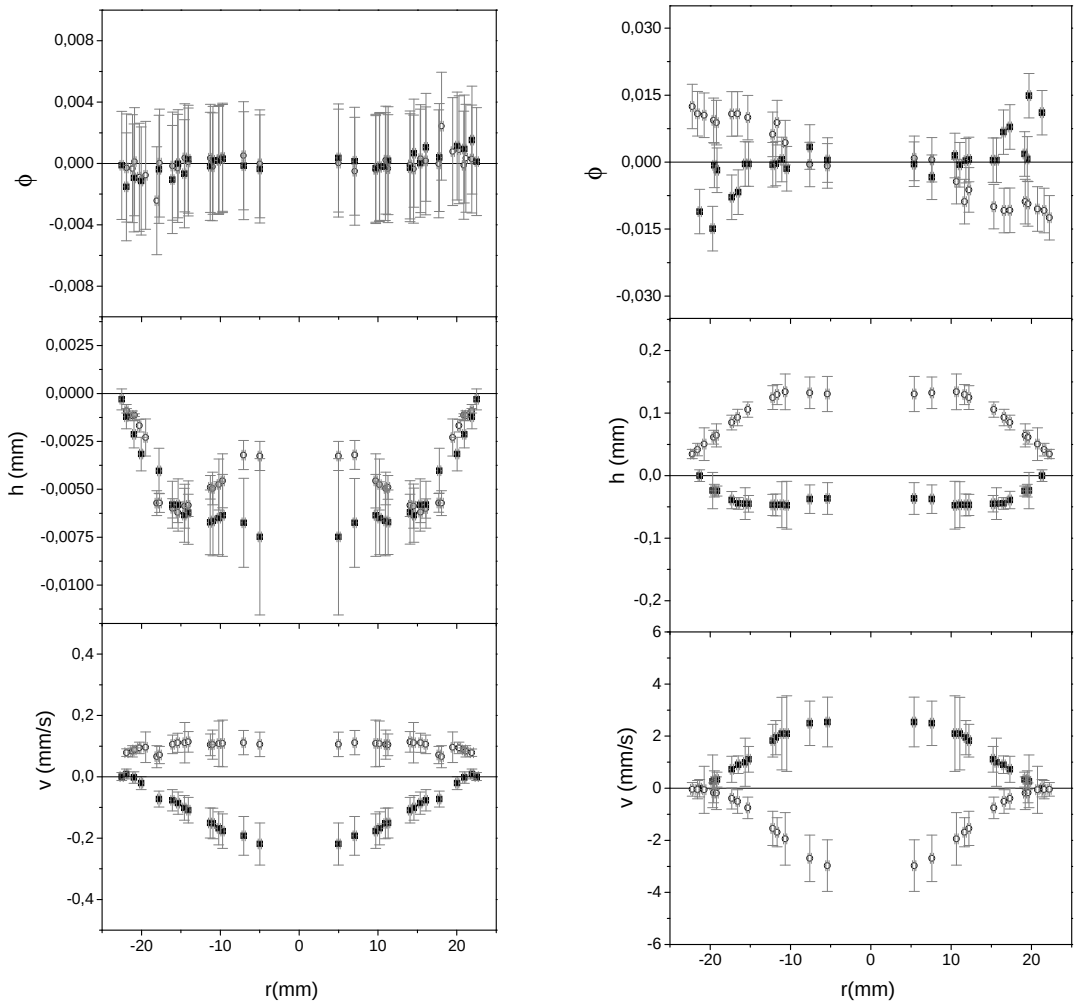

Figure 11.2: OD measures at two different time–phases within an oscillation for a driving amplitude $z_0 = 0.8$ mm and driving frequency $\nu = 2.0$ Hz. **Left:** Glycerol. **Right:** 100/60 CPyCl/NaSal solution.

ones (computed for the bulk) displayed in Fig. 9.2. We observed that their shapes were fully coincident for each of the two driving frequencies. This showed that the quiescent flow points of the velocity profiles did not change their position along the vertical direction, and thus their location in the bulk could be used as reference to compute the velocity profiles at the interface from the deformation profiles.

For the calculation of $h(r,t)$, we chose r_0 as the radial coordinate of the quiescent flow point (in the bulk) closest to the cylinder axis. Implicitly, we assumed that the stagnation points predicted by Eq. (9.2) for the bulk did not change their position as the interface was approached. This assumption was confirmed by our OD and PIV results (Section 11.3). We performed measurements for a viscoelastic fluid (Maxwell-a) and a Newtonian one (glycerol).

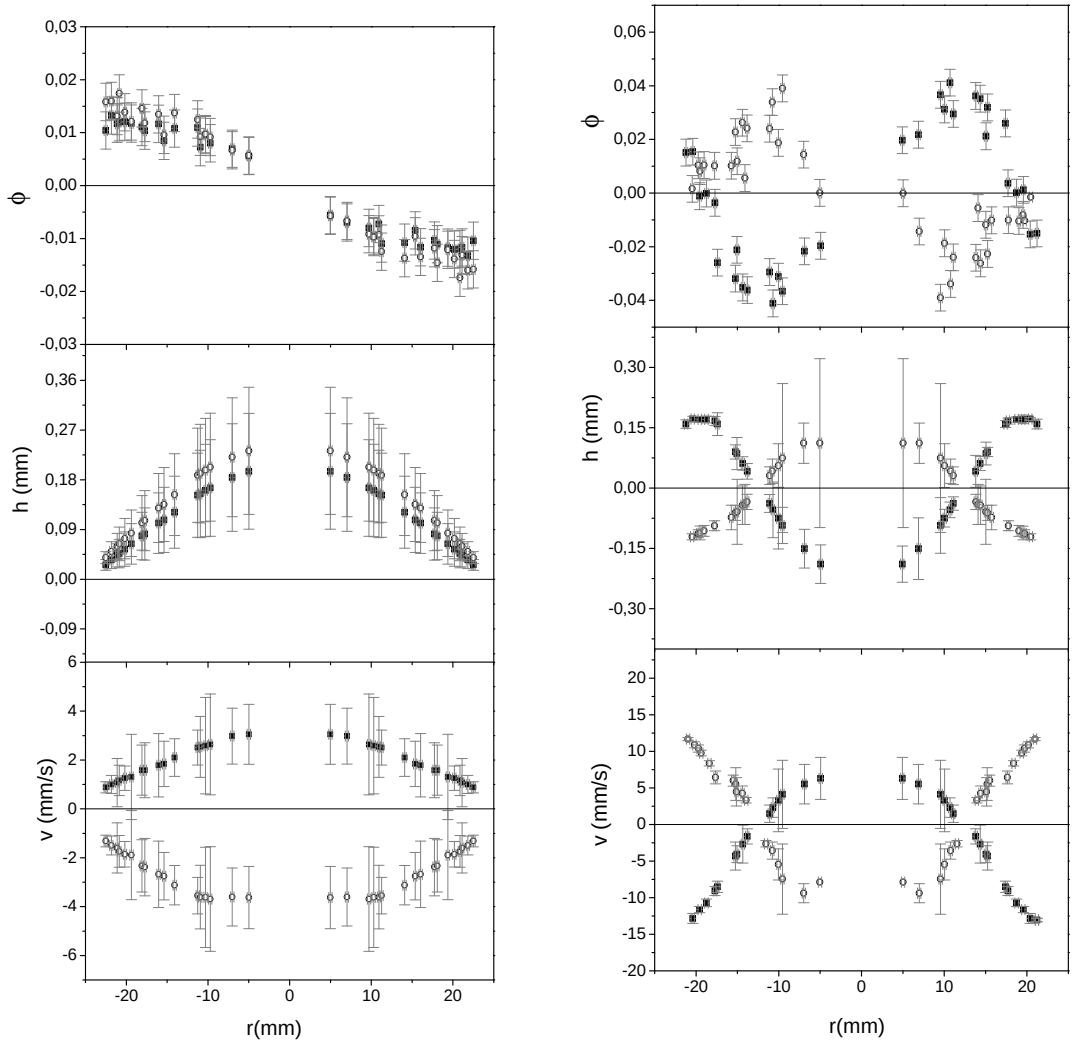

Figure 11.3: OD measures at two different time–phases within an oscillation for a driving amplitude $z_0 = 0.8$ mm and driving frequency $\nu = 6.5$ Hz. **Left:** Glycerol. **Right:** 100/60 CPyCl/NaSal solution.

The velocity profiles are presented on the bottom of Figs. 11.2 and 11.3. The magnitude of the interfacial velocities was in all cases much lower than the one measured in the bulk of the fluid. This was mostly due to the stabilizing role of surface tension, as confirmed by PIV measurements (Section 11.3).

It is interesting to note that the velocity profiles of the interface depended also on the direction of motion of the driving piston. The magnitude of the velocity was systematically lower for positive displacements of the piston (liquid displacing air) than for negative ones (air displacing liquid). We attribute this asymmetry to the fact that the large viscosity contrast across the interface stabilized the displacement of a nearly inviscid fluid (air) by a viscous liquid, and destabilized the opposite displacement.

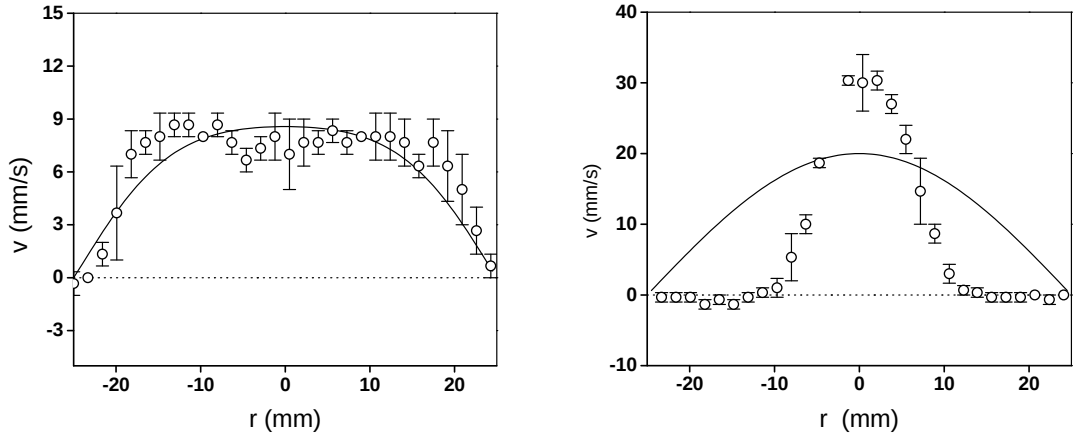

Figure 11.4: PIV results at 2 Hz (dots), measured at 6 cm from the upper free interface, and the corresponding theoretical prediction (solid line) for a driving amplitude $z_0 = 0.8$ mm. **Left:** Glycerol at $t = 0.125$ s. **Right:** 100/60 CPyCl/NaSal solution at $t = 0.375$ s.

11.3 Bulk velocity profiles

The results presented in this section provide measurements of the whole velocity profile, instead of measurements at a single point in the flow [Castrejón-Pita 03b]. The velocity profiles were measured in the bulk of the fluid, and can be compared to the ones obtained at the fluid-air interface (Section 11.2). For bulk measurements, we obtained velocity profiles at three distances from the air-fluid interface: 60, 100 and 250 mm. As Newtonian test fluids we used glycerol and silicone oil.

The following set of figures presents the velocity profiles in the bulk of the fluid column, determined by PIV measurements, together with the theoretical profiles given by Eq. (9.2) at coincident time–phases, for comparison. The profiles were determined at the driving frequencies of 2 Hz (Fig. 11.4), 6.5 Hz (Fig. 11.5), and 10 Hz (Fig. 11.6) at 60 mm of the fluid-air interface for a driving amplitude $z_0 = 0.8$ mm. The time–phases were selected by the criterion that the velocity at the tube axis was a maximum.

The first observation to make is that the instantaneous velocity profiles of the Maxwell fluid, driven at 2 Hz, presented a single defined sign of velocity (single direction of motion) along the whole radius of the tube. As the driving frequency was increased to 6.5 and 10 Hz, however, the instantaneous profiles displayed a progressively more complex structure, revealing the presence of annular regions within the tube with alternating upward/downward motion. Notice that this complexity is inherent to the viscoelastic properties of the Maxwell fluid. For the Newtonian fluid (glycerol) the instantaneous flow in the tube followed the same direction for the three driving frequencies tested and for all the radial positions of the tube.

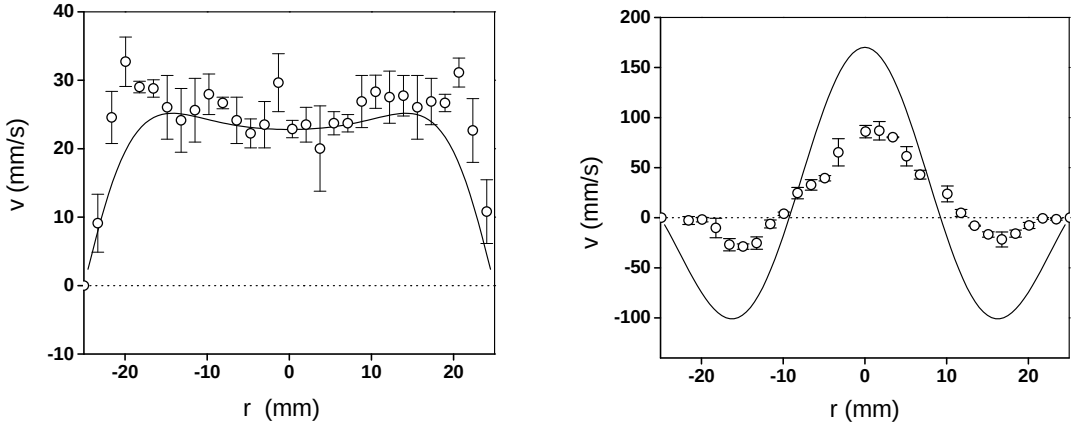

Figure 11.5: PIV results at 6.5 Hz (dots), measured at 6 cm from the upper free interface, and the corresponding theoretical prediction (solid line) for a driving amplitude $z_0 = 0.8mm$ **Left:** Glycerol at $t = 0.115$ s. **Right:** 100/60 CPyCl/NaSal solution at $t = 0.038$ s.

For the viscoelastic fluid the boundaries between consecutive annular regions with alternating signs of the velocity did not move. They correspond to the stagnation regions of the flow which were already discussed in Section 9. The PIV results showed that the number of quiescent flow points along the radial direction of the tube increased with the driving frequency, in agreement with the theoretical prediction (Fig. 9.2).

Some of the measured profiles of the viscoelastic fluid showed regions near the walls with vanishingly small velocities and near zero velocity gradients, most noticeably the one at 2 Hz shown in Fig. 11.4. These profiles were reminiscent of velocity profiles obtained for systems that display shear–banding. Indeed, the CPyCl/NaSal solution

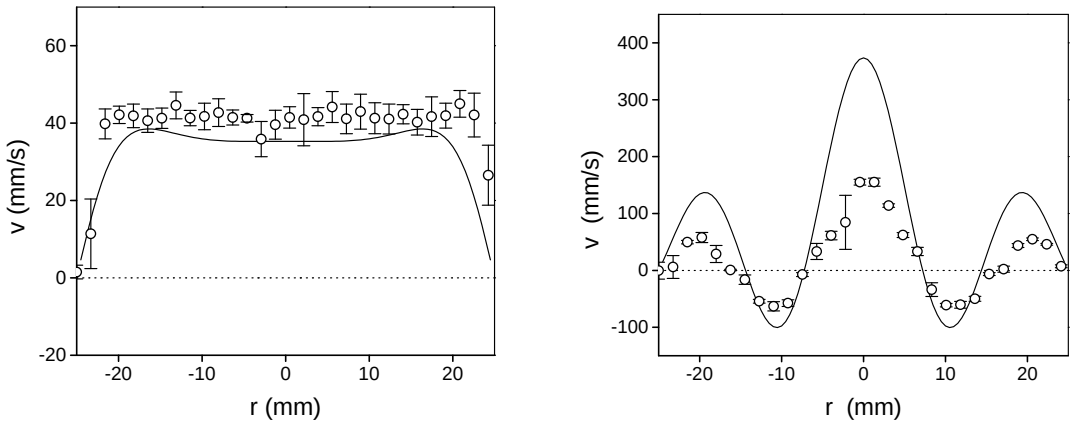

Figure 11.6: PIV results at 10 Hz (dots), measured at 6 cm from the upper free interface, and the corresponding theoretical prediction (solid line) for a driving frequency $z_0 = 0.8$ mm. **Left:** Glycerol at $t = 0.075$ s. **Right:** 100/60 CPyCl/NaSal solution at $t = 0.025$ s.

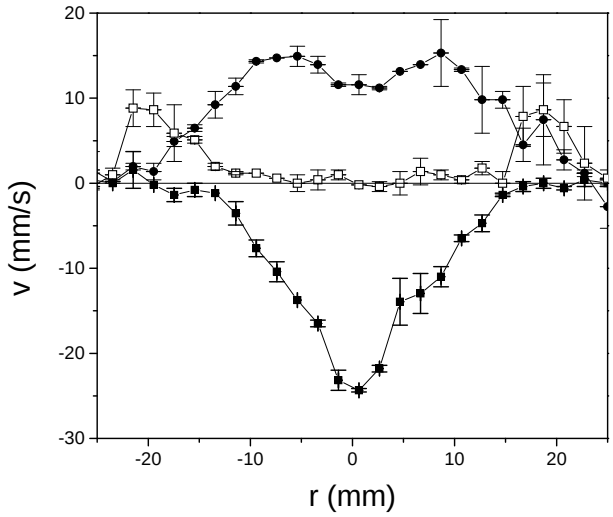

Figure 11.7: 100/60 CPyCl/NaSal solution: PIV results at 2 Hz, measured at 6 cm from the upper free interface and at different time phases within a driving period for a driving amplitude $z_0 = 0.8$ mm.

is commonly known to exhibit shear-banding [Méndez-Sánchez-03b], but we have enough evidence to discard this effect in our experiments. We did not observe an increase in turbidity in the region of the fluid close to the walls, nor changes in the local intensity of the scattered light that could be attributed to inhomogeneities. Furthermore, we monitored possible changes on the polarization state of the scattered light, an indication of banding [Lerouge 00]. No changes in the optical properties were observed for the amplitude and frequency range explored in laminar flows. In addition, Fig. 11.7 demonstrates that the velocity near the walls took values distinctly different from zero at different phases within an oscillation period.

Performing PIV measurements at two different heights of the liquid column allowed the study of the influence of the upper free interface on the velocity profiles. Thus, it is interesting to compare the results presented above, which were performed at 6 cm from the upper interface, to the results shown in Fig. 11.8, which have been performed at 10 cm from the upper interface. The first conclusion to draw from corresponding measurements at different heights is that the location of the quiescent flow points was not affected by the presence of the upper free interface. The second conclusion is that the magnitude of the velocity profile was smaller when the measurement was carried out closer to the free interface. The damping effect of the free interface, disregarded in the theory, originated from the air–liquid surface tension. This observation applied equally to the two fluids investigated (Newtonian and Maxwellian) and was also confimed by the asymmetry measured in the fluid-air

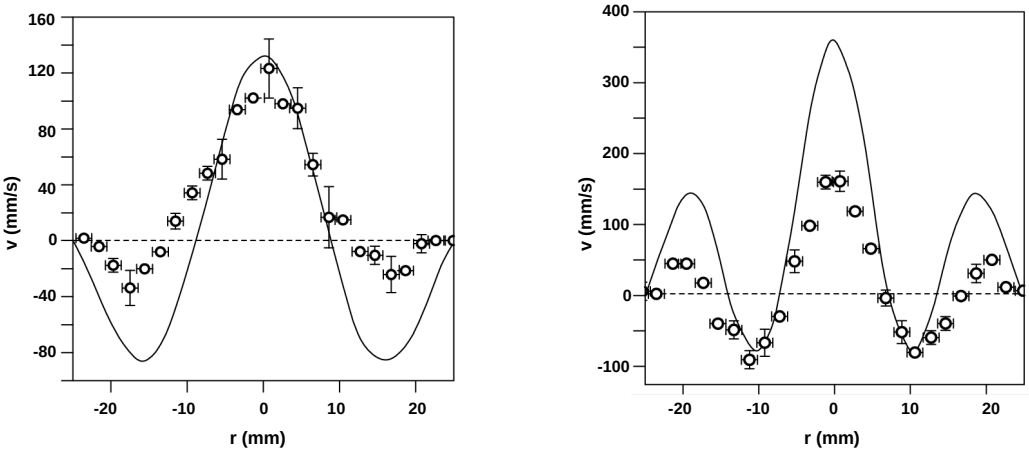

Figure 11.8: Left: 100/60 CPyCl/NaSal solution: PIV results at 6.5 Hz (dots), obtained at 10 cm from the upper free interface, and the corresponding theoretical prediction (solid line) at $t = 0.057$ s for a driving amplitude $z_0 = 0.8$ mm. **Right:** 100/60 CPyCl/NaSal solution: PIV results at 10 Hz (dots), obtained at 10 cm from the upper free interface, and the corresponding theoretical prediction (solid line) at $t = 0.022$ s for a driving amplitude $z_0 = 0.8$ mm.

interface velocity profiles.

The oscillating flow was also studied at a higher distance of the fluid-air interface (25 cm), for driving frequencies 2.0, 6.5 and 10.5 Hz (maxima of dynamic response) and 3.5, 8.2 and 11.5 Hz (minima of the dynamic response). For the two lowest frequencies, we measured laminar velocity profiles up to driving amplitudes $z_0 = 2.5$ mm (Fig. 11.9). For the rest of the frequencies explored, the velocity profile was laminar at a driving amplitude of $z_0 = 0.8$ mm . The experimental velocity profiles were in reasonable agreement with the theoretical ones. The number of quiescent flow points was the same, and their location very similar. As a general trend, however, the theory overestimated the measured velocity. Possible reasons for it will be discussed in Sec. 13.

Although for laminar flows the information provided by the velocity profiles and the velocity maps (x, y, v_x, v_y) is the same, it is interesting to look at the velocity maps and the vorticity maps of the flow. Since the flow has an strong dependence on the radial position, even for structureless laminar profiles ($\nu = 2.0$ and 3.5 Hz), the vorticity of the flow is important. We performed experiments for driving amplitudes of 0.8, 1.2, 1.6, 2.0 and 2.5 mm. For the lowest driving frequencies, results at all driving amplitudes were equivalent (Figs. 11.10, 11.11). As driving frequency increased, the number of annular regions increased and so did the vorticity (Fig. 11.12). At a driving amplitude of 0.8 mm, however, the flow still remained laminar for all the frequencies

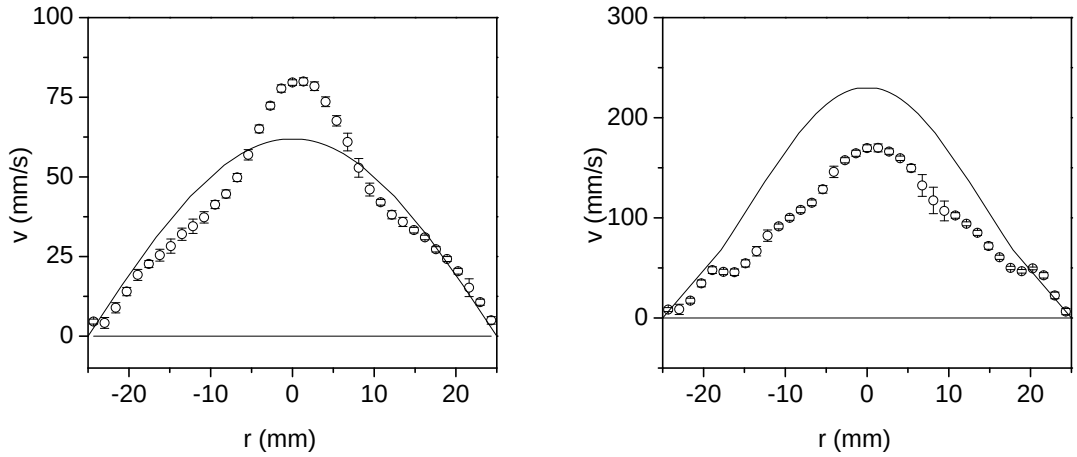

Figure 11.9: Left: 100/60 CPyCl/NaSal solution: PIV results at 2.0 Hz (dots) obtained at 25 cm from the upper free interface, for a driving amplitude $z_0 = 2.5$ mm, and the corresponding theoretical prediction (solid line) at $t = 0.2$ s. **Right:** 100/60 CPyCl/NaSal solution: PIV results at 3.5 Hz (dots) obtained at 25 cm from the upper free interface for a driving amplitude of 2.5 mm, and the corresponding theoretical prediction (solid line) at $t = 0.037$ s.

explored. The azimuthal vorticity contours reveal that the vorticity, as expected, concentrated near the regions where the flow was quiescent.

We also studied the behavior of a Newtonian fluid with a viscosity very similar

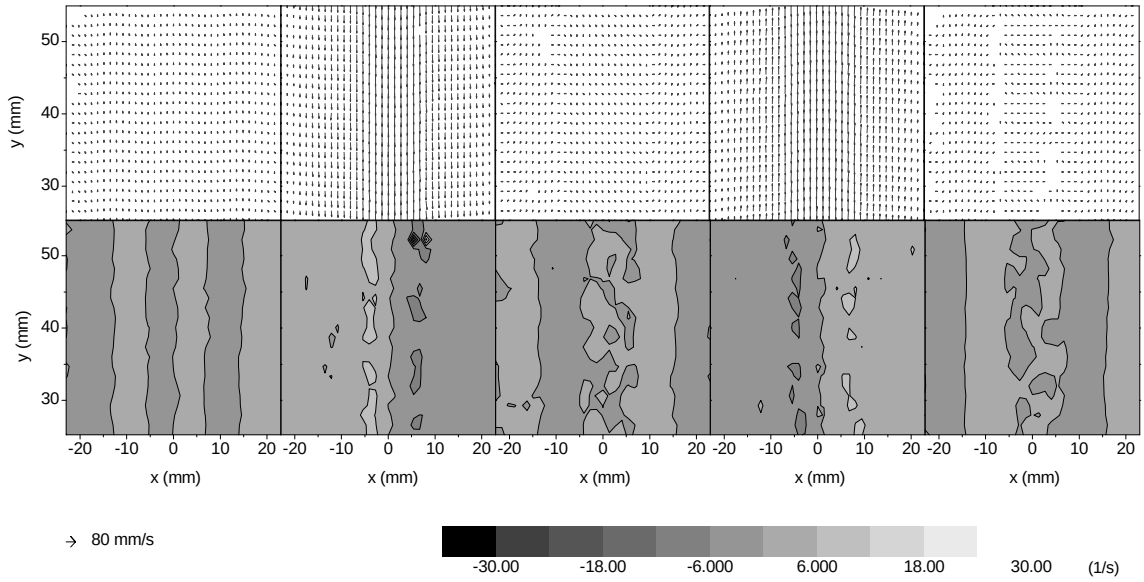

Figure 11.10: 100:60 CPyCl/NaSal solution: PIV results for $\nu = 2.0$ Hz and $z_0 = 2.5$ mm (Re $= 10^{-2}$, Wi $= 2.4$). Top: velocity vector field. Bottom: azimuthal vorticity contours. The corresponding scales are given by the little arrow and the grey level scale at the bottom of the figure.

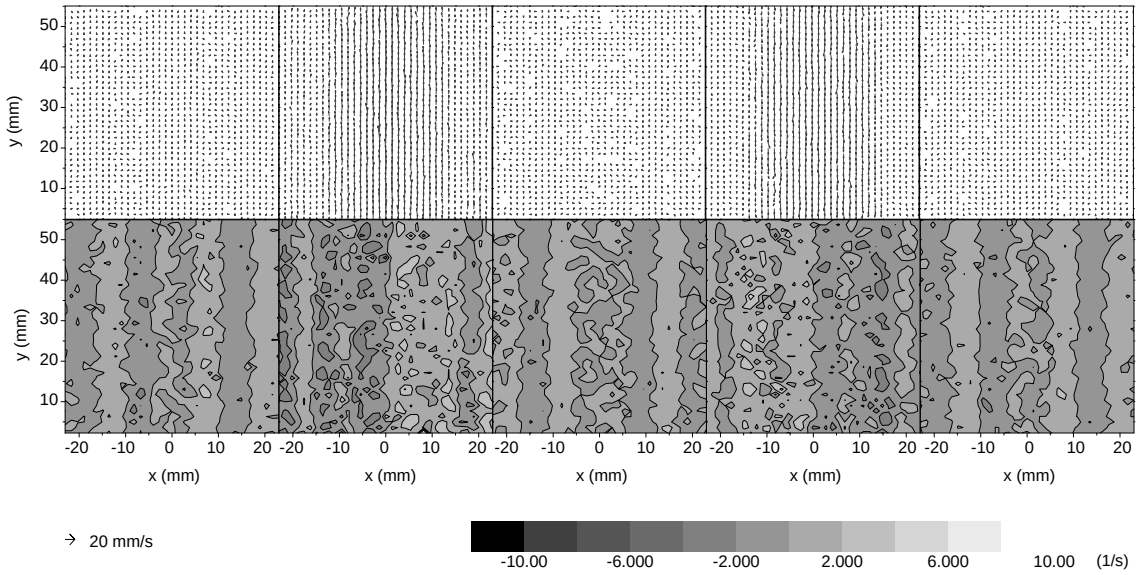

Figure 11.11: 100:60 CPyCl/NaSal solution: PIV results for $\nu = 3.5$ Hz and $z_0 = 0.8$ mm ($\mathrm{Re} = 8 \cdot 10^{-3}$, $\mathrm{Wi} = 1.3$). Top: velocity vector field. Bottom: azimuthal vorticity contours. The corresponding scales are given by the little arrow and the grey level scale at the bottom of the figure.

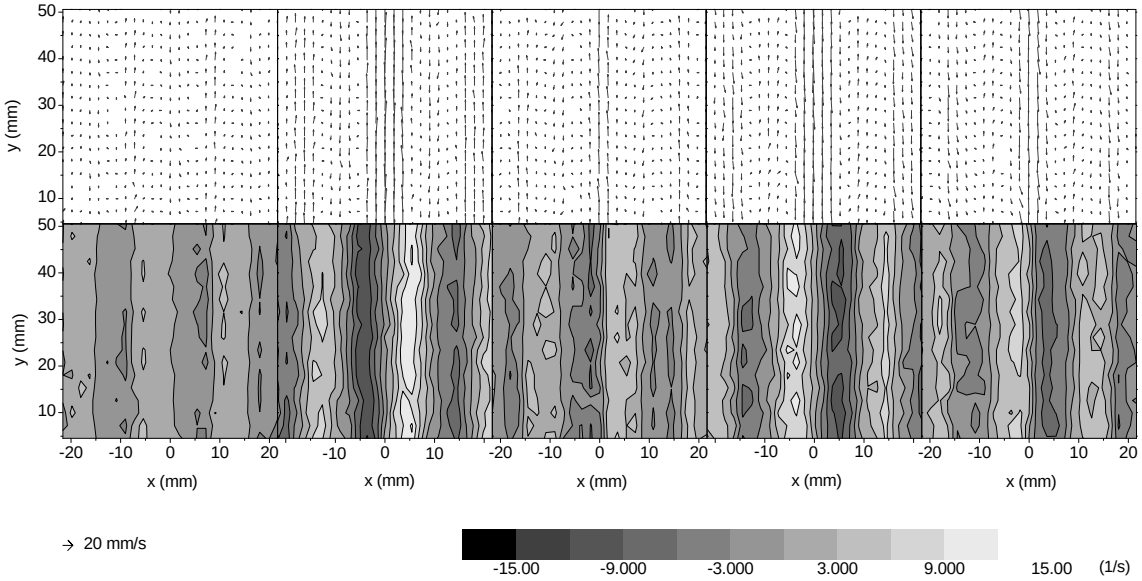

Figure 11.12: 100:60 CPyCl/NaSal solution: PIV results for $\nu = 11.5$ Hz and $z_0 = 0.8$ mm ($\mathrm{Re} = 3 \cdot 10^{-2}$, $\mathrm{Wi} = 18.6$). Top: velocity vector field. Bottom: azimuthal vorticity contours. The corresponding scales are given by the little arrow and the grey level scale at the bottom of the figure.

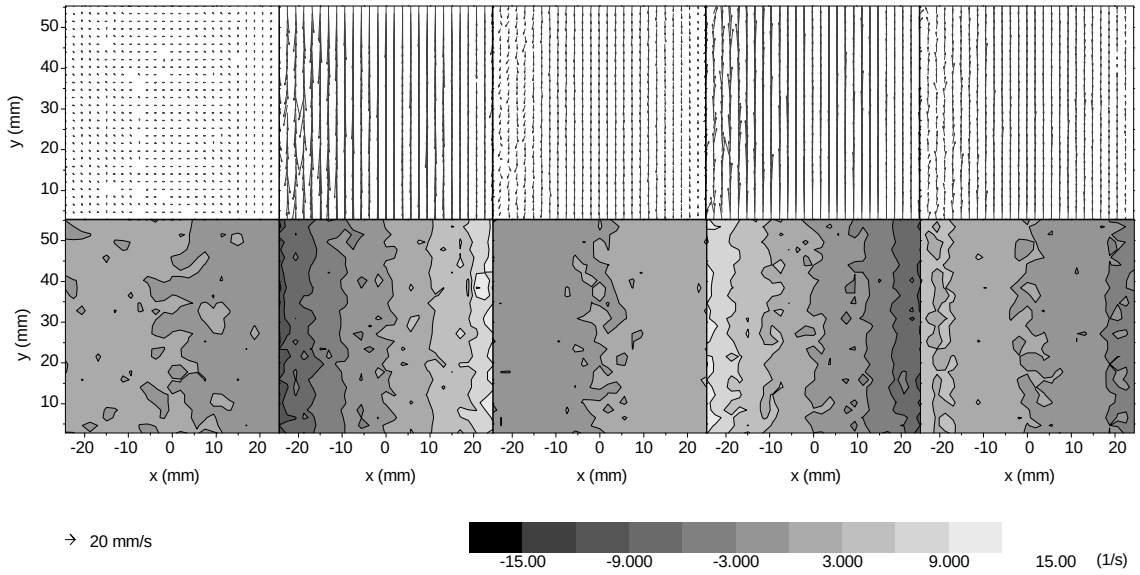

Figure 11.13: Silicone oil: PIV results for $\nu = 8.2$ Hz and $z_0 = 1.2$ mm ($\mathrm{Re} = 3 \cdot 10^{-2}$). Top: velocity vector field. Bottom: azimuthal vorticity contours. The corresponding scales are given by the little arrow and the grey level scale at the bottom of the figure.

to the viscosity of the viscoelastic fluid: a silicone oil of $\eta = 56$ Pa·s. From our experimental results we could conclude that the Newtonian laminar flow of the silicone oil was stable up to a driving amplitude of 10 mm in the range of frequencies explored in our experiments. As an example, Fig. 11.13 presents the velocity vector field of the silicone oil at different time–phases within an oscillation period, for a driving amplitude of 1.2 mm and a driving frequency of 8.2 Hz. The results show that a laminar parallel shear–flow was established. The fluid oscillated in the tube following the periodicity of the driving. All fluid elements in the interrogation plane moved instantaneously in the same direction, the velocity approaching zero near the tube boundaries.

Chapter 12

Hydrodynamic instabilities

The measurements presented in this section were all carried out at a distance of about 5 tube radius (12.5 cm) from the neutral position of the piston and 25 cm from the upper interface. By covering the fluid surface at the top end of the tube with a cover lid, we verified that oscillations of the free surface did not had any measurable effect on the flow in the region of interest. The experiments were performed at driving amplitudes and frequencies detailed in Table 12.1.

The results for the basic (laminar) flow of the viscoelastic fluid (Ch. 11) show that this flow consisted of annular regions of alternating upward/downward motion, separated by quiescent boundaries. Shear stresses concentrated at these quiescent boundaries and increased as the magnitude of the driving increased, until the laminar flow became unstable.

A linear theory [del Río 98], which is expected to be valid at low driving amplitudes, predicted that the number of annular regions increased with driving frequency but did not depend on driving amplitude. This is why, according to Table 12.1, the viscoelastic flow was laminar at all amplitudes for the two lower driving frequencies explored, 2.0 and 3.5 Hz. (Figs. 11.10 and 11.11)

As already discussed, the PIV measurements of the Newtonian fluids (silicone oil and glycerol) showed a laminar flow in the whole range of driving parameters explored. This was not the case for the viscoelastic fluid. Table 12.1 provides a summary of the flow structures observed at different values of the driving parameters. Laminar flows have been already described in Section 11.3. The viscoelastic flow became unstable at $\nu = 6.5$ Hz (second resonance frequency), $z_0 = 1.2$ mm, and at all higher frequencies and amplitudes.

At the onset of instability ($\nu = 6.5$ Hz, $z_0 = 1.2$ mm) the laminar flow exhibited modulations of the vertical streamlines, although in Fig. 12.1 these modulations are

		z_0 (mm)	0.8	1.2	1.6	2.0	2.5
Dynamic response	Nr. of nodes	ν (Hz)	Flow structure				
Maximum	0	2.0	L	L	L	L	L
Minimum	0	3.5	L	L	L	L	L
Maximum	2	6.5	L	F–L	V–s	V–s	V–ns
Minimum	2	8.2	L	V–s	V–s	V–ns	V–ns
Maximum	4	10.5	L	F–L	V–s	V–ns	V–ns
Minimum	4	11.5	L	V–s	V–s	V–ns	V–ns

Table 12.1: Summary of PIV results for the 100:60 CPyCl/NaSal solution. z_0, ν are driving amplitude and frequency. At each driving frequency, the behaviour of the dynamic response of the viscoelastic–fluid–tube system and the number of nodes observed in the laminar regime (away from the tube wall) are also indicated. (L) : Laminar flow, (F–L): Fluctuating Laminar, (V–s): Symmetric vortices, (V–ns): Non–symmetric vortices.

hardly visible. At $\nu = 10.5$ Hz, $z_0 = 1.2$ mm, i.e. at the next resonance frequency and same amplitude, an additional pair of nodes had formed. Even so, the same modulations of the vertical streamlines were observed.

Interestingly, at the intermediate frequency $\nu = 8.2$ Hz and at the same amplitude $z_0 = 1.2$ mm, the flow presented two stationary symmetric vortices (V–s) (Fig. 12.2).

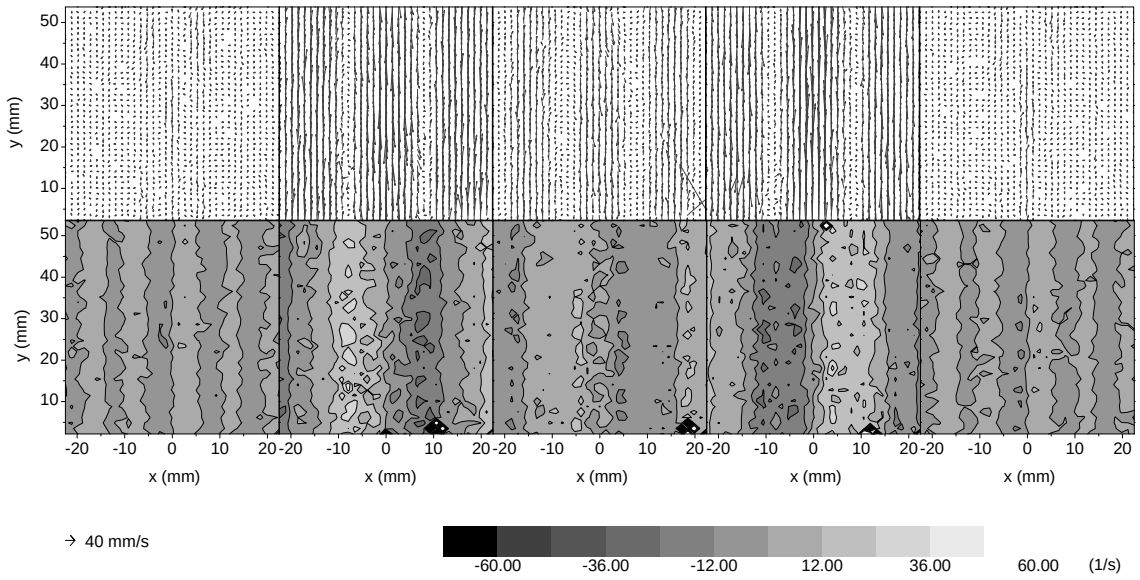

Figure 12.1: 100:60 CPyCl/NaSal solution: PIV results for $\nu = 6.5$ Hz and $z_0 = 1.2$ mm ($\mathrm{Re} = 2 \cdot 10^{-2}$, $\mathrm{Wi} = 11.4$). Top: velocity vector field. Bottom: azimuthal vorticity contours. The corresponding scales are given by the little arrow and the grey level scale at the bottom of the figure.

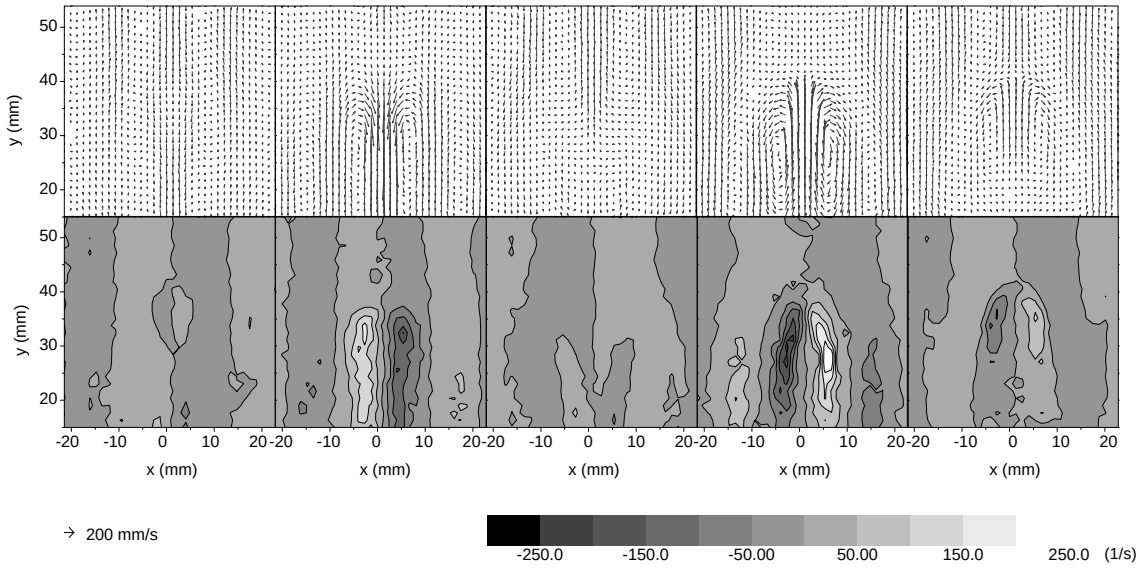

Figure 12.2: 100:60 CPyCl/NaSal solution: PIV results for $\nu = 8.2$ Hz and $z_0 = 1.2$ mm ($\mathrm{Re} = 3 \cdot 10^{-2}$, $\mathrm{Wi} = 19.3$). Top: velocity vector field. Bottom: azimuthal vorticity contours. The corresponding scales are given by the little arrow and the grey level scale at the bottom of the figure.

The two vortices were centered at the two nodes of the base flow closer to the tube axis, and changed their rotation direction every half-period of the driving.

By taking low resolution PIV measurements in a larger image area, we found that several equidistant vortices formed along the tube, with a centre–to–centre separation of about 2.5 tube radius for a forcing frequency of 8.2 Hz, and of 1.25 tube radius for a forcing frequency of 11.5 Hz. Figure 12.3 shows an example.

The cylindrical symmetry of the flow was still preserved at the onset of instability. This was verified by repeating the measurements several times from the state of repose. Therefore Fig. 12.2 is actually showing a transverse cut of a toroidal vortex around the symmetry axis of the tube. This was also true for the experiments at a driving amplitude of 1.6 mm (Figs. 12.4, 12.5, 12.6, 12.7), and for the experiment at 2.0 mm and 6.5 Hz (Fig. 12.8).

For stationary symmetric vortices the radial coordinate of the vortex center was independent of driving amplitude (Fig. 12.9) but strongly dependent on driving frequency. As the driving frequency increased the vortex center approached the center of the tube, following the behavior of the quiescent flow points (Fig. 12.9). It is also interesting to notice that the presence of these symmetric vortices did not modify the location of the quiescent flow points.

As the driving increased further, the vortices got distorted and led to more com-

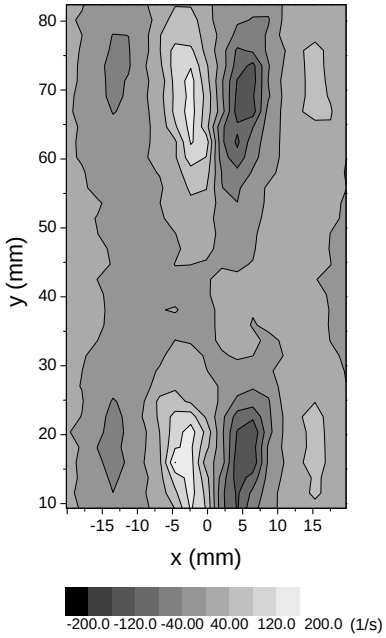

Figure 12.3: Low resolution azimuthal vorticity contours for the 100:60 CPyCl/NaSal solution driven at $\nu = 8.2$ Hz and $z_0 = 1.2$ mm ($\mathrm{Re} = 3 \cdot 10^{-2}$, $\mathrm{Wi} = 19.3$), showing that several toroidal vortices form along the tube.

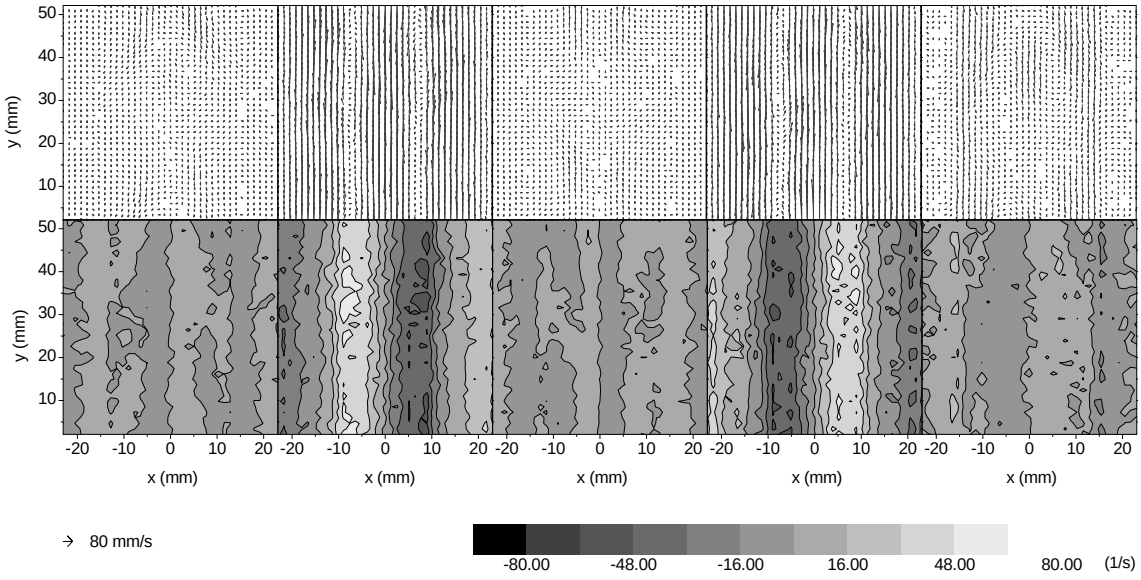

Figure 12.4: 100:60 CPyCl/NaSal solution: PIV results for $\nu = 6.5$ Hz and $z_0 = 1.6$ mm ($\mathrm{Re} = 3 \cdot 10^{-2}$, $\mathrm{Wi} = 15.1$). Top: velocity vector field. Bottom: azimuthal vorticity contours. The corresponding scales are given by the little arrow and the grey level scale at the bottom of the figure.

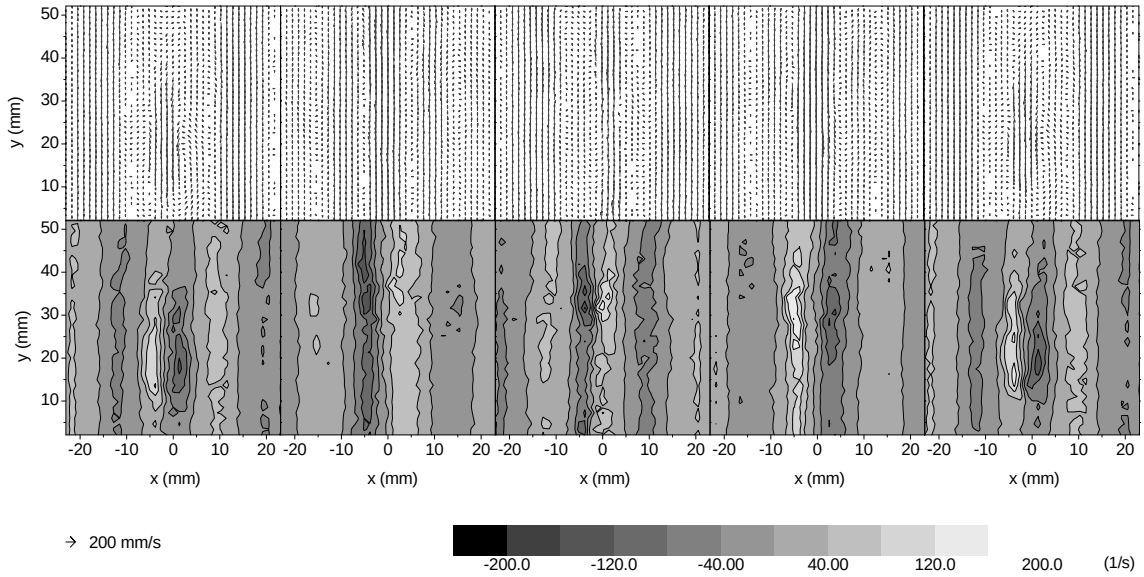

Figure 12.5: 100:60 CPyCl/NaSal solution: PIV results for $\nu = 8.2$ Hz and $z_0 = 1.6$ mm ($\mathrm{Re} = 4 \cdot 10^{-2}$, $\mathrm{Wi} = 25.7$). Top: velocity vector field. Bottom: azimuthal vorticity contours. The corresponding scales are given by the little arrow and the grey level scale at the bottom of the figure.

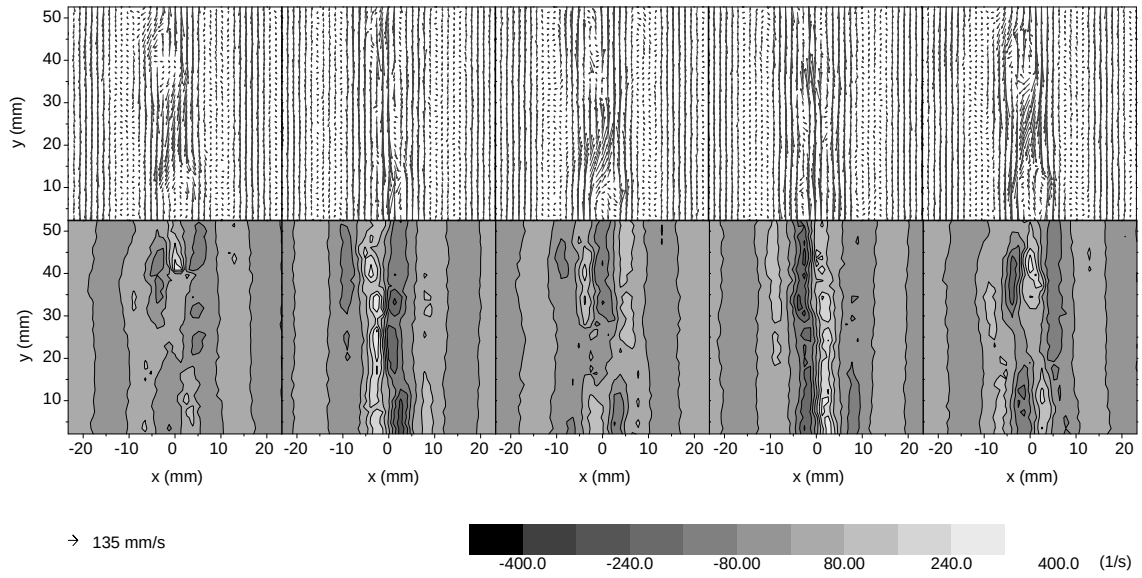

Figure 12.6: 100:60 CPyCl/NaSal solution: PIV results for $\nu = 10.5$ Hz and $z_0 = 1.6$ mm ($\mathrm{Re} = 5 \cdot 10^{-2}$, $\mathrm{Wi} = 32.9$). Top: velocity vector field. Bottom: azimuthal vorticity contours. The corresponding scales are given by the little arrow and the grey level scale at the bottom of the figure.

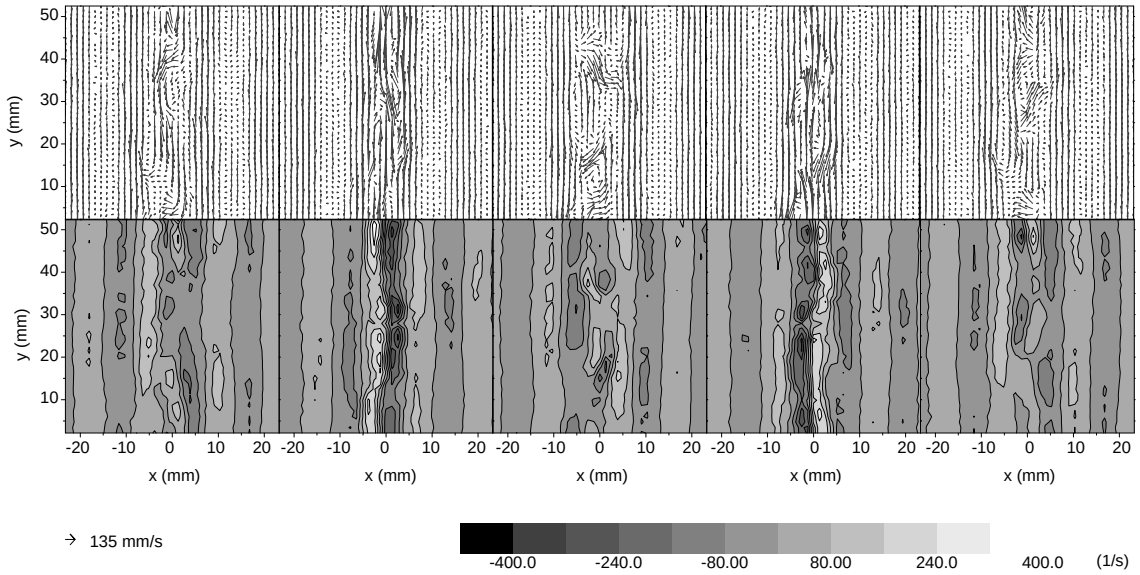

Figure 12.7: 100:60 CPyCl/NaSal solution: PIV results for $\nu = 11.5$ Hz and $z_0 = 1.6$ mm ($\mathrm{Re} = 5 \cdot 10^{-2}$, $\mathrm{Wi} = 37.2$). Top: velocity vector field. Bottom: azimuthal vorticity contours. The corresponding scales are given by the little arrow and the grey level scale at the bottom of the figure.

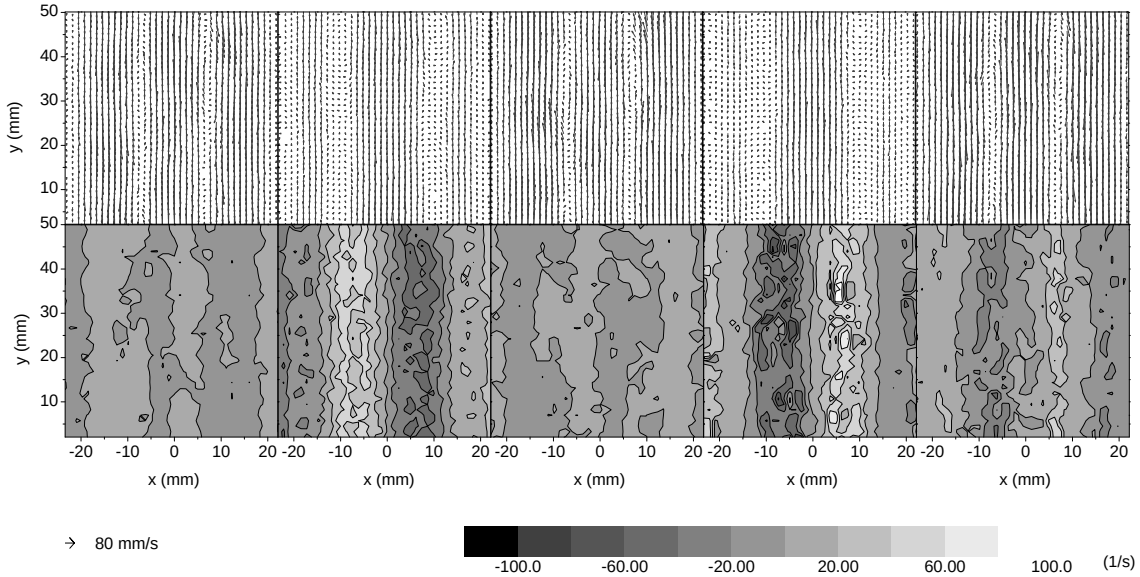

Figure 12.8: 100:60 CPyCl/NaSal solution: PIV results for $\nu = 6.5$ Hz and $z_0 = 2.0$ mm ($\mathrm{Re} = 4 \cdot 10^{-2}$, $\mathrm{Wi} = 18.9$). Top: velocity vector field. Bottom: azimuthal vorticity contours. The corresponding scales are given by the little arrow and the grey level scale at the bottom of the figure.

	Experimental measure
□	Quiescent flow points ($z_0 = 0.8$ mm)
●	Maximum of the vortex sheet adjacent to $r = 0$ ($z_0 = 0.8$ mm)
△	Center of the vortex ($z_0 = 1.2$ mm)
▲	Center of the vortex ($z_0 = 1.6$ mm)

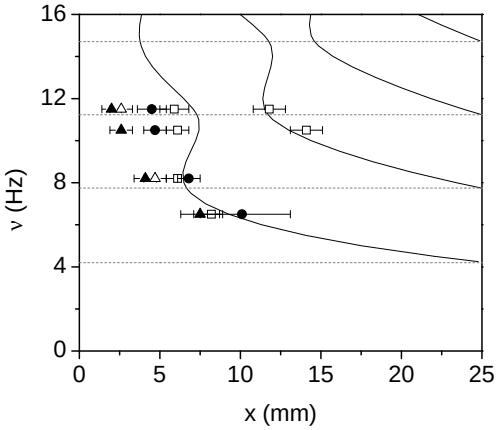

Figure 12.9: Solid lines: theoretical radial location of the quiescent flow points along the radial coordinate of the cylinder x. The dashed horizontal lines correspond to minima of the permeability. The parameters ρ, η and t_m used to calculate the diagram are the ones listed for CPyCl/NaSal 100:60 in Ch. 10, together with the cylinder radius $a = 25$ mm.

plex nonsymmetric structures (V–ns). At forcings of 2.0 mm, 8.2 Hz (Fig. 12.10), 10.5 Hz and 11.5 Hz, and at forcings of 2.5 mm, 8.2 Hz the vortices formed very close to the tube axis and were heavily distorted, but their center did not move in time. At this same amplitude (2.5 mm) and at forcing frequencies of 6.5, 10.5 and 11.5 Hz we observed nonsymmetric and non-stationary vortices. Figure 12.11 shows

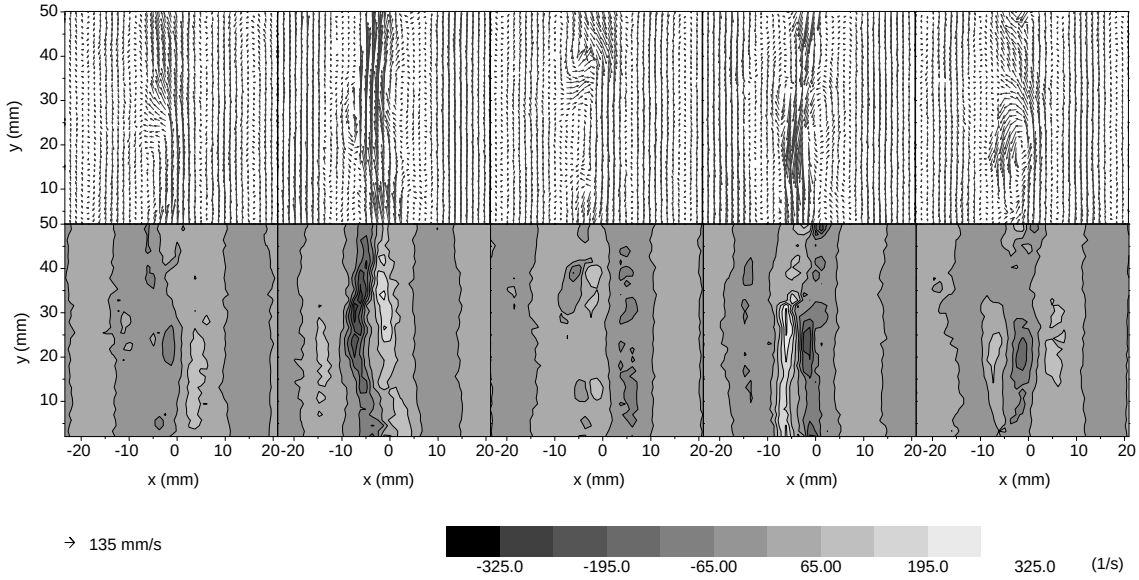

Figure 12.10: 100:60 CPyCl/NaSal solution: PIV results for $\nu = 8.2$ Hz and $z_0 = 2.0$ mm ($\mathrm{Re} = 5 \cdot 10^{-2}$, $\mathrm{Wi} = 32.1$). Top: velocity vector field. Bottom: azimuthal vorticity contours. The corresponding scales are given by the little arrow and the grey level scale at the bottom of the figure.

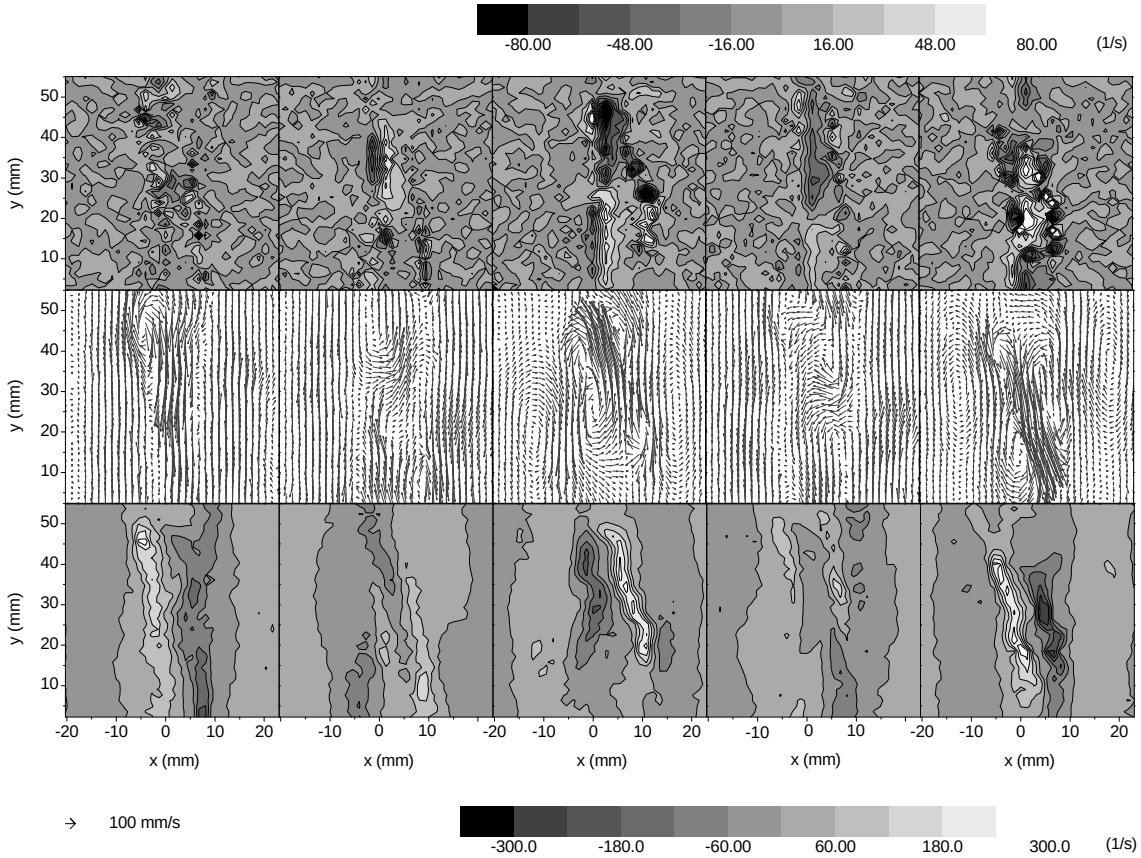

Figure 12.11: 100:60 CPyCl/NaSal solution: PIV results for $\nu = 6.5$ Hz and $z_0 = 2.5$ mm (Re $= 4 \cdot 10^{-2}$, Wi $= 40.1$). (a) Local divergence, (b) velocity vector field, (c) azimuthal vorticity contours. The corresponding scales are given by the little arrow and the grey level scales.

that the flow lost its axial symmetry and, furthermore, the non-negligible magnitude of the local divergence at the vortices revealed that the velocity field at the vortices presented an azimuthal component.

12.1 Velocity fluctuations

We observed that velocity fluctuations as defined by Eqs. (10.9) and (10.10) were very small in all the laminar velocity maps. The instability caused a noticeable increase of the velocity fluctuations in both the vertical and horizontal components of the velocity.

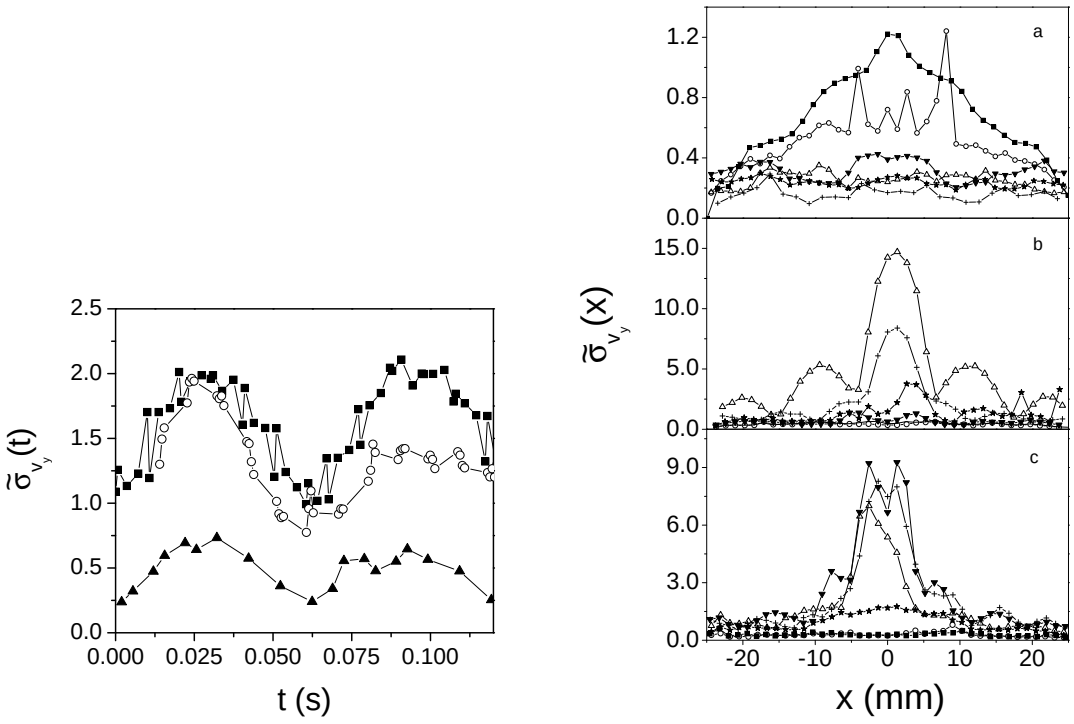

Figure 12.12: Left: 100:60 CPyCl/NaSal solution: x-averaged rms dimensionless fluctuations of the y component of the velocity, $\widetilde{\sigma}_{v_y}(t)$, as a function of time, for the viscoelastic fluid driven at 8.2 Hz and amplitudes $z_0 = 0.8$ (▲), $z_0 = 1.6$ (○) and 2.0 mm (■). **Right:** 100:60 CPyCl/NaSal solution: time-averaged rms fluctuations of the y component of the velocity, $\widetilde{\sigma}_{v_y}(x)$, as a function of the radial coordinate, x, for the viscoelastic fluid driven at an amplitude (a) 0.8 mm, (b) 1.2 mm, and (c) 1.6 mm. The symbols correspond to the different driving frequencies (in Hz): 2.0 (■), 3.5 (○), 6.5 (⋆), 8.2 (△), 10.5 (▼), and 11.5 (+). Notice the different magnitude of the vertical scales.

12.1.1 Space averages

If a velocity component follows the periodicity of the driving, its rms fluctuations are periodic as well, with a frequency two times the driving frequency. This is visible in Fig. 12.12 left, which shows the dimensionless x-averaged rms fluctuations of the y component of the velocity vs. time, $\widetilde{\sigma}_{v_y}(t)$, for the viscoelastic fluid driven at 8.2 Hz. The correlation between adjacent points validates the procedure of folding the PIV data back to the first oscillation period, thus confirming that even this non–laminar flow followed the periodicity of the basic flow.

12.1.2 Time averages

The spatial dependence of the velocity fluctuations was computed by averaging $\widetilde{\sigma}_{v_x}(x,t)$ and $\widetilde{\sigma}_{v_y}(x,t)$ in a time period. Figure 12.12 (right) shows the latter result,

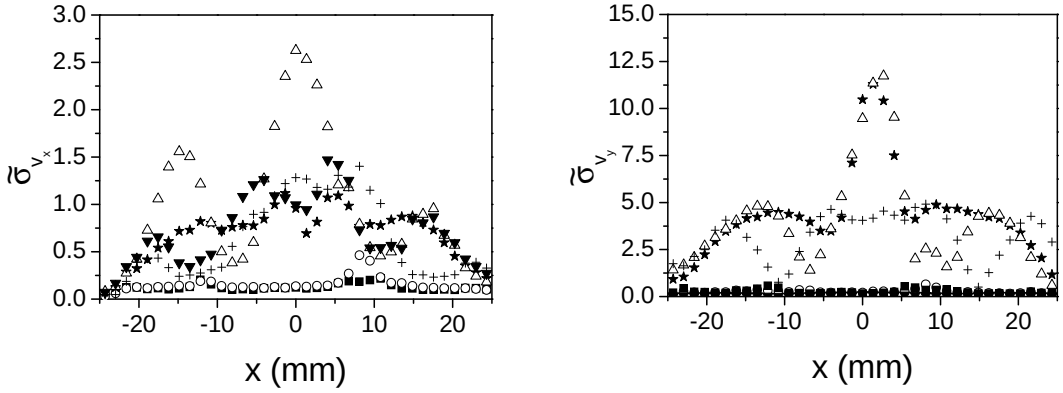

Figure 12.13: Left: 100:60 CPyCl/NaSal solution: time-averaged rms fluctuations of the x component of the velocity, $\widetilde{\sigma}_{v_x}(x)$, as a function of the radial coordinate, x, for the viscoelastic fluid driven at an amplitude of 2.5 mm. **Right:** 100:60 CPyCl/NaSal solution: time-averaged rms fluctuations of the y component of the velocity, $\widetilde{\sigma}_{v_y}(x)$, as a function of the radial coordinate, x, for the viscoelastic fluid driven at an amplitude of 2.5 mm. The symbols correspond to the different driving frequencies (in Hz): 2.0 (■), 3.5 (○), 6.5 (⋆), 8.2 (△), 10.5 (▼), and 11.5 (+). Notice the different magnitude of the vertical scales.

$\widetilde{\sigma}_{v_y}(x)$, for different driving amplitudes.

At the lowest driving amplitude, 0.8 mm (a), for which the flow was always laminar, $\widetilde{\sigma}_{v_y}(x)$ was nearly structureless and had a small magnitude at all driving frequencies. Fluctuations were slightly larger for the weakest forcing, simply because of the experimental uncertainty in the velocity measurements. At 1.2 mm (b), $\widetilde{\sigma}_{v_y}(x)$ was still very small for the two lowest frequencies (laminar flow); for the second and third resonance frequencies it had a similar value than for 0.8 mm; for the second and third minima of the dynamic response, instead, it became large and peaked at the tube axis . Finally, at 1.6 mm (c), $\widetilde{\sigma}_{v_y}(x)$ exhibited similar trends than at the previous driving amplitude for the three higher driving frequencies.

Although the magnitude of σ_{v_y} was higher than σ_{v_x} for most of the experiments, they behaved very similarly for all the driving frequencies and amplitudes (Fig. 12.13).

The time-averaged rms fluctuations of the velocity could also be integrated in space, to obtain a global magnitude $\widetilde{\sigma}_{v_y}$ that behaved as an order parameter for the instability. Fig. 12.14 shows how rms fluctuations increased abruptly at the onset of the instability for the different driving frequencies.

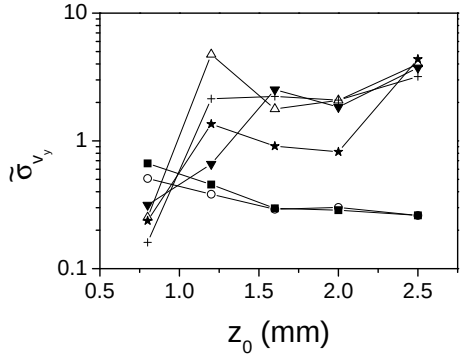

Figure 12.14: 100:60 CPyCl/NaSal solution: space– and time–averaged rms fluctuations of the y component of the velocity, as a function of driving amplitude z_0, at the different driving frequencies (in Hz): 2.0 (■), 3.5 (○), 6.5 (⋆), 8.2 (△), 10.5 (▼), and 11.5 (+).

12.2 Birefringence measurements

We performed simultaneous PIV measurements and birefringence visualization in our system, at forcing frequencies of 8.2 and 11.5 Hz, and a forcing amplitude of $z_0 = 1.2$ mm. Fig. 12.15 shows the images obtained at $\nu = 8.2$ Hz and $z_0 = 1.2$ mm. The time phase of each image corresponds approximately to the time phases of the velocity and vorticity maps in Fig. 12.2.

Near the tube walls the stresses aligned vertical and were rather large at all time phases. On the contrary, the stress field at the central part of the flow depended strongly on the time phase. The stresses were not homogeneously distributed in the vertical direction. The bands were wider at the center of the vortices at time phases $T/4$, $3T/4$, when the vorticity was large. At time phases when the vorticity was small (0, $T/2$, T) the stress field relaxed and the bands brooked into small birefringent zones.

The time evolution of the birefringence map from an stage close to the repose state to an stage for which periodic stationary vortices were fully developed is also

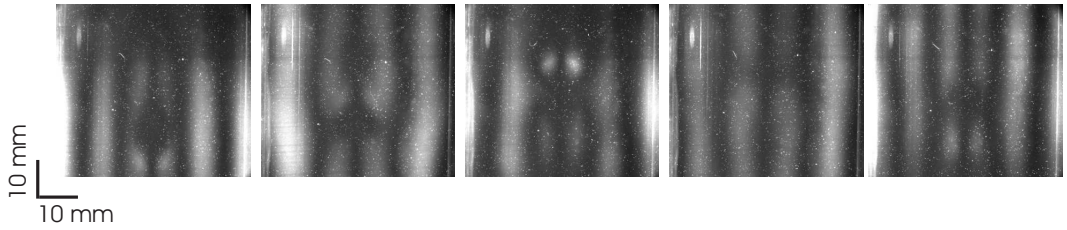

Figure 12.15: Birefringence map for $\nu = 8.2$ Hz and $z_0 = 1.2$ mm. Time phases: 0, $T/4$, $T/2$, $3T/4$ and T.

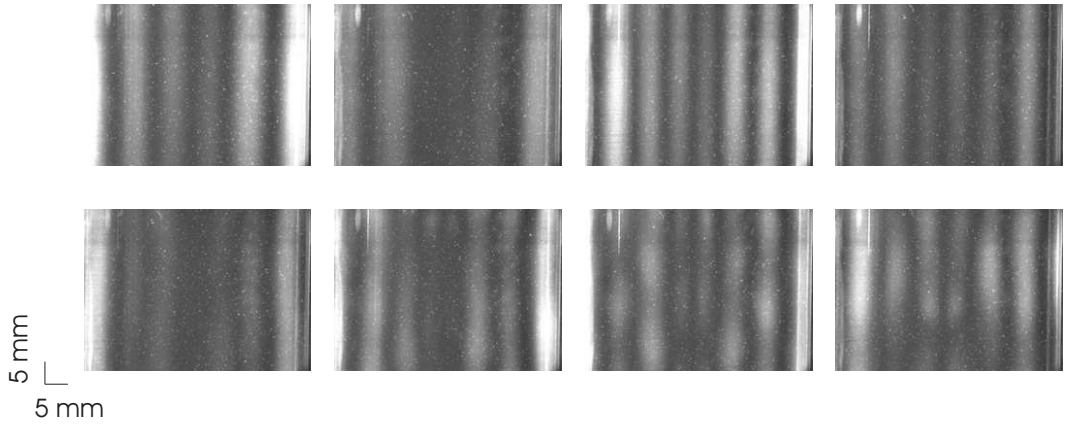

Figure 12.16: Birefringence map for $\nu = 11.5$ Hz and $z_0 = 1.2$ mm. The time between frames (from left to right and from top to bottom) is 2.667 s.

shown for $\nu = 11.5$ Hz, $z_0 = 1.2$ mm (Fig. 12.16). In the first images, for which the instability was not still developed, the stresses were homogeneous in the vertical direction. It is also noticeable that the number of birefringence bands increased before the destabilization of the flow took place. In the last images of the time evolution, the behavior was similar to the behavior described for Fig. 12.15.

Chapter 13

Oscillating flow of a Maxwell fluid: Summary and discussion

13.1 Dynamic permeability

LDA measurements of the fluid velocity at the symmetry axis of the cylinder as a function of driving frequency, for two different compositions of the surfactant solution, enabled us to show that the frequencies of the resonance peaks can be predicted accurately in terms of the fluid rheological properties by a simple linear theory [del Río 98]. This theory neglects inertial effects, and makes use of a linear Maxwell model as constitutive relation for the viscoelastic fluid.

13.2 Laminar base flow

The laminar oscillating flow of Maxwell and Newtonian fluids in a tube was characterized by two optical techniques: PIV and OD. Systematic PIV measurements of the radial velocity field in the bulk of the fluid were performed at six different driving frequencies. While the velocity profile of Newtonian fluids along the radial direction did not change sign, this was not the case for the Maxwellian fluid. The profiles measured at 6.5, 8.2, 10.5 and 11.5 Hz presented regions with alternating signs of the velocity, separated by quiescent flow points. The number of quiescent flow points increased with the driving frequency, revealing the increasing complexity of the flow. Measurements within the fluid column at different heights showed that these quiescent flow points did not shift as one moved along the vertical direction, and that their radial location was accurately reproduced by the linear theory.

The linear theory also predicts that the shape of the laminar velocity profiles is

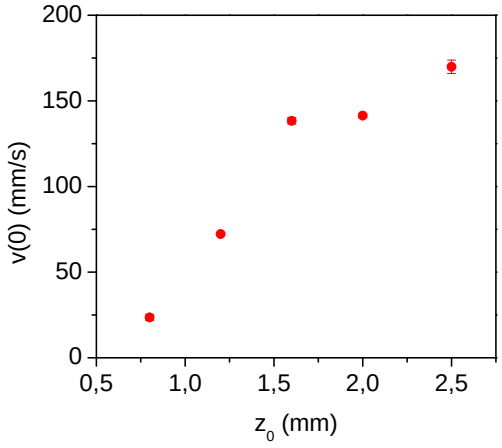

Figure 13.1: 100/60 CPyCl/NaSal: Velocity at the tube axis at the different driving amplitudes for a driving frequency $\nu = 3.5$ Hz measured at 25 cm of the free interface.

independent of driving amplitude. For some driving frequencies (2.0 and 3.5 Hz) we obtained laminar velocity profiles at different driving amplitudes. The magnitude of the velocity at the center of the tube showed a linear dependence with driving amplitude (Fig. 13.1) in agreement with the theoretical predictions. The dimensionless velocity profiles were found to be independent of driving amplitude for 3.5 Hz (Fig. 13.2, right), whereas for 2.0 Hz, however, there was a noticeable difference on the velocity profile corresponding to the lowest driving amplitude (Fig. 13.2, left).

We also observed that the theoretical magnitude of the velocity was systematically larger than the measured one. There are several possible reasons for this disagreement:

- A first explanation would be that the theory disregarded nonlinearities, and these tended to limit the attainable values of the velocity. Nonlinearities could arise from either the hydrodynamic equations or the constitutive relation of the fluid. In our case, however, since the small amplitude of the piston oscillations ensured that Re was vanishingly small, the linearized momentum equation was a very good approximation. On the other hand, taking into account the cylindrical symmetry of the problem and assuming that the velocity depended only on the radial coordinate (as our results confirmed to a very good approximation), it turned out that the first nonlinear correction to the constitutive equation of the fluid cancelled out exactly.

- This quantitative mismatch between theory and experiment was probably due to shear–thinning of the viscoelastic fluid. As shown in Ref. [Méndez-Sánchez 03a],

our fluid is properly described by a Maxwell model up to shear rates $\dot{\gamma} \simeq 0.1$ s^{-1}, and experiences shear–thinning beyond that value. A close inspection of Figs. 11.4, 11.5, and 11.6 reveals that the shear rate actually experienced by the fluid in some phase intervals of the oscillation was larger [Castrejón-Pita 03b]. In these conditions the viscosity of the fluid decreased with shear (Appendix A). The theory predicted that the dynamic response of the system at the resonant frequencies becomes smaller as the viscosity is reduced [del Río 98], and thus would support the view that the measured velocity profiles were systematically smaller than the theoretical ones for the viscoelastic fluid (and not for the Newtonian fluid) because of shear–thinning.

- Finally, the presence of a free interface on top of the liquid column had a damping effect on the velocity amplitude. This observation was visible, both with LDA and PIV, when the results of measurements carried out at different heights within the liquid column were compared.

In addition, Optical Deflectometry measurements of the free interface confirmed that the velocity field was severely damped by the surface tension of the air–liquid interface, compared to the velocity field within the bulk. Interestingly, the deflectometry results showed also that the oscillations of the velocity field at the interface were asymmetric, the profiles corresponding to positive displacements of the piston having a slightly but systematically smaller amplitude than those corresponding to negative displacements. We attribute this asymmetry to the fact that the upward

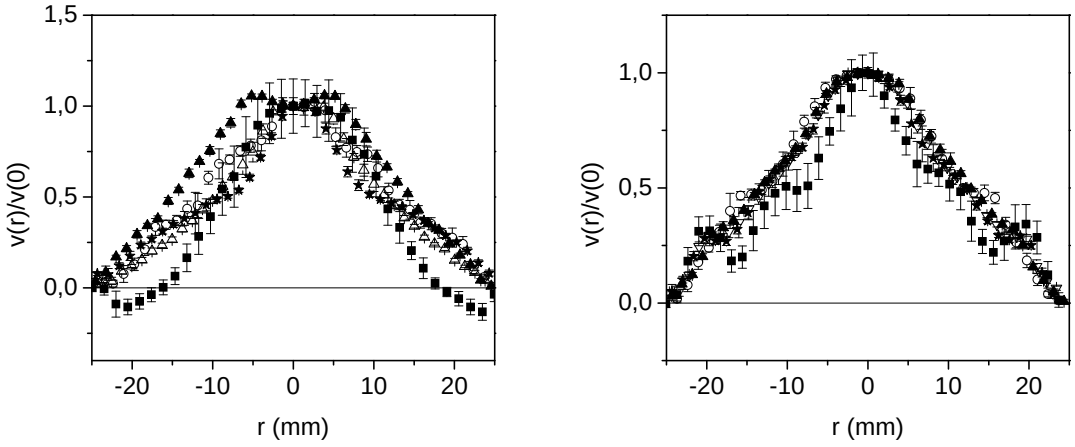

Figure 13.2: 100/60 CPyCl/NaSal solution: dimensionless velocity profiles measured at a distance $h = 25$ cm from the air-fluid interface. Different symbols correspond to driving amplitudes: (■) $z_0 = 0.8$ mm, (○) $z_0 = 1.2$ mm, (▲) $z_0 = 1.6$ mm, (△) $z_0 = 2.0$ mm, (⋆) $z_0 = 2.5$ mm. **Left:** $\nu = 2.0$ Hz. **Right:** $\nu = 3.5$ Hz.

motion of the interface (liquid displacing air) was stabilized by the viscous pressure gradient in the liquid.

13.3 Hydrodynamic instabilities

The periodic flow of a Newtonian fluid in a vertical pipe, driven by an oscillatory pressure gradient, is stable in the whole range of driving frequencies and amplitudes explored in our experiments [Hino 76]. Our experiments with silicone oil showed indeed that a relatively simple parallel shear flow was stablished, in which all the fluid moved in the same direction following the periodicity of the driving.

The behaviour of the wormlike micellar solution CPyCl/NaSal 100:60 mM was rather similar at low driving frequencies for all driving amplitudes. At higher driving frequencies, however, the laminar base flow turned to be unstable at increasing driving amplitudes. The Reynolds number was small in all the experiments, but the Weissenberg number reached high values for some of the Maxwell flows.

The structure of the laminar base flow was important to the development of the first instability. At the lowest driving amplitudes that made the flow unstable two symmetric vortices (actually a cut of a single toroidal vortex) appeared always where the shear rate was maximum in the laminar velocity profiles, in radial positions for which the velocity was relatively low. Indeed, vortices were only present at driving frequencies for which the laminar velocity profiles displayed alternating regions of upward/downward motion. This pointed to the large shear rates experienced by the fluid, at the quiescent points of the flow, as responsible for the first instability of the laminar base flow.

Since the driving amplitude z_0 in our experimental setup could not be modified in a continuous way, we cannot answer the question whether the instability observed presented hysteresis. This information is relevant to ascertain the critical or subcritical nature of this first bifurcation. A modification of the setup that will allow to modify z_0 (and thus the Weissenberg number) in a continuous way is nearly completed (Appendix B).

Since high shear rates were reached in most of our measurements, we cannot discard that shear-thinning played a role in making the base flow unstable. The instability in this case would not be purely viscoelastic. We believe however that the essential ingredient to render the laminar flow unstable was its complex structure of alternating, stationary regions of upward/downward motion, which was entirely due to the elasticity of the fluid. In particular, it is worth noting that the location of the

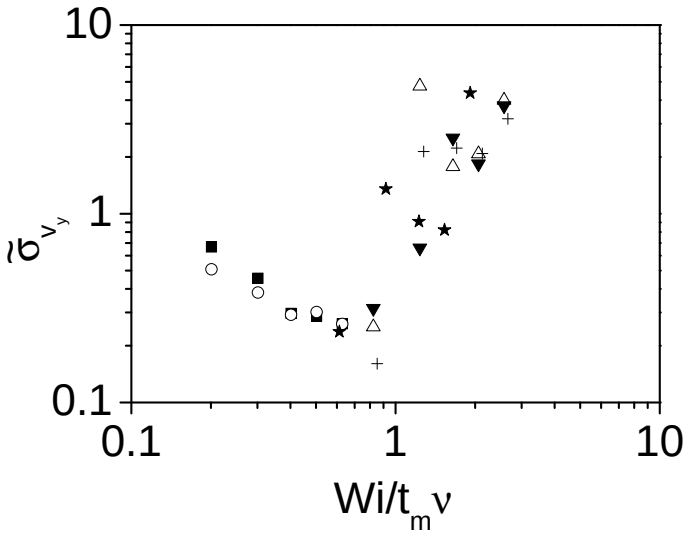

Figure 13.3: 100:60 CPyCl/NaSal solution: space– and time–averaged rms fluctuations of the y component of the velocity, as a function of the dimensionless control parameter $\chi \equiv \frac{\mathrm{Wi}}{t_m \nu}$, at the different driving frequencies (in Hz): 2.0 (■), 3.5 (○), 6.5 (⋆), 8.2 (△), 10.5 (▼), and 11.5 (+).

quiescent flow points was accurately predicted by a theory based on the constitutive equation of a purely viscoelastic fluid. More experimental work using complex fluids of different rheological behaviour is needed to elucidate the importance of shear–thinning.

Assuming that the instabilities observed in our system were essentially due to the viscoelastic nature of the fluid (and shear–thinning played only a secondary role), they represented a first experimental observation of an elastic instability in parallel shear flow at very low Reynolds number. This is quite relevant, since elastic instabilities of this kind have been reported only for flows with curved streamlines. In these flows elastic normal stresses destabilize the flow, ultimately leading to elastic turbulence (or turbulence without inertia) [Groisman 00; Groisman 98]. Pakdel and McKinley [Pakdel 96] showed that this linear instability disappears when the curvature of the streamlines goes to zero, so that shear flows with parallel streamlines would not undergo linear elastic instabilities. However, Morozov and Van Saarloos have shown theoretically that parallel shear flows of purely viscoelastic fluids might be nonlinearly unstable [Morozov 05]. In the framework of these predictions, we have presented an experimental scenario that allowed the generation of parallel shear flows with large shear rates (high Wi) at small Re. This has been achieved by the oscillatory driving, that made the elastic properties of the fluid very important even in the laminar regime.

The time-averaged rms fluctuations of the velocity can be integrated in space, to obtain a global magnitude $\widetilde{\sigma}_{v_y}$ that behaves as an 'order parameter' for the instability. The corresponding control parameter should be the Weissenberg number, given the elastic nature of the instability. However, since we are driving the flow at periods much shorter than t_m (the relaxation time of the fluid) the driving period $(1/\nu)$ is possibly a more relevant time–scale for the formation of the vortices than t_m. Considering this, we define a dimensionless control parameter

$$\chi \equiv \frac{\mathrm{Wi}}{t_m \nu} = \frac{2\pi z_0}{r_q}. \tag{13.1}$$

Figure 13.3 shows the behaviour of $\widetilde{\sigma}_{v_y}$ as a function of χ at the different driving frequencies. The onset of a secondary flow on top of the basic parallel–shear flow is made manifest by a noticeable increase in this magnitude as vortices develop. Interestingly, the onset of the instability occurs at a value $\chi \simeq 1$.

Chapter 14

Conclusions

- **Lateral instabilities in Saffman–Taylor fingers**

  We studied the stability of the flat sides of long normal Saffman–Taylor fingers to external perturbations. We perturbed the fingers by two different mechanisms: quenched disorder in the Hele–Shaw cell and periodic modulation of the finger tip velocity.

  For both perturbations we observed a low amplitude–long wavelength lateral instability at both sides of the finger. A selection process took place for both destabilization mechanisms, leading to a preferred frequency which was roughly a half of the characteristic finger frequency.

  The amplitude of the instability was characterized in a wide range of velocities for the quenched disorder experiments. We observed a decay in the amplitude of the instability as velocity (or capillary number) increased, following a power law $\delta_\lambda \propto Ca^{-1/3}$. At even higher velocities ($Ca > 0.05$), the amplitude of the instability increased.

  Periodic modulations of the finger tip velocity were studied at two velocities, in a wide range of forcing frequencies. The response of the finger was always symmetric and for most fingers reached a stationary state. At low frequencies the frequency of the lateral instability was strongly dependent on forcing frequency, whereas at high frequencies we observed the selection process mentioned above. In this process, the final state of the system selected a frequency much lower than the forcing frequency.

- **Oscillating flow of a Maxwell fluid in a tube**

  We used four different optical techniques (LDA, PIV, OD and birefringence) to characterize the oscillating flow of a viscoelastic fluid (a solution of CPyCl/NaSal

in water) contained in a vertical cylinder and subjected to an oscillating pressure gradient. Two Newtonian fluids (glycerol and silicone oil) were also studied for the sake of comparison.

Our LDA measurements in the tube axis showed that the linear model presented in Sec. 3.3.2 predicts accurately the position of the resonance peaks in terms of the rheological properties of the fluids.

PIV measurements of the velocity maps at the bulk showed structureless velocity profiles for a Newtonian fluid, while the velocity profiles observed for the Maxwell fluid presented regions of alternating velocity separated by quiescent flow boundaries. The number of quiescent flow points increased as driving frequency increased, and its location was accurately predicted by the linear model. Measurements at different distances of the free interface (including OD measurements at the free interface) showed that the radial location of these quiescent flow points was independent of the distance to the free interface.

We also carried out PIV measurements of the oscillatory flow at different driving amplitudes. The oscillatory flow of the Newtonian fluid was stable in the whole range of parameters explored. The oscillatory flow of the Maxwell fluid was unstable at large drivings, even though Re remained very small. The first instability observed gave rise to a stationary toroidal vortex with axial symmetry. At increasing driving amplitudes these simple vortices were unstable and more complex structures were found. These results are potentially relevant in the search for experimental observations of a subcritical instability in parallel viscoelastic shear flows.

Chapter 15

Future perspectives

- **Lateral instabilities in Saffman–Taylor fingers**

  For the quenched disorder experiments the characterization of the lateral instability was performed at different velocities and gap spacings. For the periodic perturbation we studied the curve $\nu_{out}(\nu_{in}, V_\infty, W, b)$ at fixed W and b, and we performed experiments for two different V_∞. It would be very interesting to explore a curve at fixed frequency varying the velocity (this would allow study the effect of the velocity in the selected frequency, for instance) and also to explore the effect of varying the gap spacing.

  It would be also interesting to perform measurements with new cell widths, both for quenched disorder experiments and for periodic perturbation experiments. This would allow to generate longer fingers and determine the stationary state of the fingers forced with frequencies close to the characteristic finger frequency.

  The combination of both perturbation mechanisms is another interesting point that was not explored in this thesis. We observed that the lateral instability had a preferred frequency, which was roughly the same than the one obtained in periodic perturbation experiments. The unanswered question is the effect of noise in the selection process for a periodically forced finger. It seems quite clear that the selected frequency would be the same, but the dynamic process of selection may be affected by the presence of the noise. Thus, the time needed for the system to reach the final stage could be significantly shorter thanks to the presence of the noise, which would help the system to select the final wavelength.

- **Oscillating flow of a Maxwell fluid in a tube**

  The characterization of the laminar velocity profiles was thoroughly performed

in several series of experiments. We explored a wide range of frequencies and we varied the fluid properties. It would be interesting to perform measurements in a tube with a different radius. This would allow to confirm the scaling with the geometry of the system predicted by [del Río 98]. Also, it would be interesting to perform measurements at low amplitudes and high frequencies in order to determine the maximum number of quiescent flow points which the velocity maps could support.

The study of the instability of the fluid has still some open questions that were not addressed in this thesis. First, it would be very important to determine if the shear–thinning behavior of the fluid plays an important role in the instability. This point could be solved by replacing our elastic shear–thinning fluid by a non–elastic shear–thinning fluid (for instance Xhanthane [Lindner 00c]) or by a purely elastic fluid (Boger fluid [Boger 96]).

As commented in Chapter 13, the onset of the instability could not be characterized accurately with our experimental setup. In order to determine (i) the minimum amplitude required to destabilize the flow at a fixed frequency, and (ii) the possibility of an hysteretic behavior at the bifurcation point we have designed a new experimental setup. This new setup is described in Appendix B. It allows the continuous change of driving amplitude at fixed frequency by ramping the driving amplitude back and forth, this setup will allow to elucidate the sub- or supercritical character of the bifurcation.

Our measurements were mostly directed to the characterization of the first instability observed in the system. The study of higher driving frequencies and amplitudes would be interesting to study secondary bifurcations of the oscillatory flow, already observed in some of our experiments, and eventually viscoelastic turbulence. The characterization of these new stages of the instability, for which we observed a loss of the axial symmetry, would require new techniques of characterization.

Bibliography

[Aarts 98] A.C.T. Aarts and G.J. Ooms. Net flow of compressible viscous liquids induced by travelling waves in porous media. *J. Eng. Math.* **34**, 435 (1998).

[Adrian 91] R.J. Adrian. Particle-imaging techniques for experimental fluid mechanics. *Annu. Rev. Fluid Mech.* **23**, 261 (1991).

[Alava 04] M. Alava, M. Dube and M. Rost. Imbibition in disordered media. *Adv. Phys.* **53**, 83 (2004).

[Ali 97] A. Aït Ali and R. Makhloufi. Linear and nonlinear rheology of an aqueous concentrated system of cethyltrimethlammonium chloride and sodium salicylate. *Phys. Rev. E* **56**, 4474 (1997).

[Arora 02] K. Arora, R. Sureshkumar and B. Khomami. Experimental investigation of purely elastic instabilities in periodic flows. *J. Non-Newtonian Fluid Mech.* **108**, 209 (2002).

[Avellaneda 91] M. Avellaneda and S. Torquato. Rigorous link between fluid permeability, electrical conductivity, and relaxation times for transport in porous media *Phys. Fluids A* **3**, 2529 (1991).

[Batchelor 90] G.K. Batchelor. *An introduction to fluid dynamics.* (Cambridge University Press, Cambridge, Great Britain, 1990).

[Ben Amar 99] M. Ben Amar and E. Corvera Poiré. Pushing a non-Newtonian fluid in a Hele-Shaw cell: from fingers to needles. *Phys. Fluids* **11**, 1757 (1999).

[Bensimon 86] D. Bensimon Stability of viscous fingering. *Phys. Rev. A* **33**, 1302 (1986).

[Bensimon 86-b] D. Bensimon, L.P. Kadanoff, S. Liang, B. Shraiman and C. Tang. Viscous flows in two dimensions. *Rev. Mod. Phys.* **58**, 977 (1986).

[Berret 93] J.F. Berret, J. Apell, and G. Porte. Linear rheology of entangled wormlike micelles. *Langmuir* **9**, 2851 (1993).

[Berret 97] J.F. Berret. Transient rheology of wormlike micelles. *Langmuir* **13**, 2227 (1997).

[Bird 87] R.B. Bird, R.C. Armstrong and O. Hassager *Dynamics of polymeric liquids, Volume 1.* (Wiley, New York, United States of America, 1987).

[Boger 96] D.V. Boger. Viscoelastic fluid mechanics: Interaction between prediction and experiment. *Exp. Therm. Fluid Sci.* **12**, 234 (1996).

[Bonn 95] D. Bonn, H. Kellay, M. Ben Amar and J. Meunier. Viscous finger widening with surfactants and polymers. *Phys. Rev. Lett.* **75**, 2132 (1995).

[Bonn 97] D. Bonn and J. Meunier. Viscoelastic free–boundary problems: Non–Newtonian viscosity vs normal stress effects. *Phys. Rev. Lett.* **79**, 2662 (1997).

[Britton 99] M.M. Britton and P.T. Callaghan. Shear banding instability in wormlike micellar solutions. *Eur. Phys. J. B* **7**, 237 (1999).

[Carreau 97] P.J. Carreau, D. De Kee and R.P. Chhabra *Rheology of Polymeric Systems.* (Hanser, Cincinnaty, United States of America, 1997).

[Castrejón-Pita 03a] J.R. Castrejon. Estudio Teórico-Experimental de la dinámica de fluidos viscoelásticos en tubos. Tesis de Maestría, Universidad Nacional Autónoma de México (2003).

[Castrejón-Pita 03b] J.R. Castrejón-Pita, J.A. del Río, A.A. Castrejón-Pita, G. Huelsz. Experimental Observation of Differences in the Dynamic Response of Newtonian and Maxwellian Fluids. *Phys. Rev. E* **68**, 046301 (2003).

[Cates 87] M.E. Cates. Reptation of living polymers: dynamics of entangled polymers in the presence of reversible chain-scission reactions. *Macromolecules* **20**, 2289 (1987).

[Cates 90] M.E. Cates and S.J. Candau. Statics and dynamics of worm–like surfactant micelles. *J. Phys.: Condens. Matter* **2**, 6869 (1990).

[Cáthebras 98] N. Cáthebras, A. Collet, M. Viguier and J.F. Berret. Synthesis and linear viscoelasticity of fluorinated hydrophobically modified ethoxylated urethanes (F-HEUR). *Macromolecules* **31**, 1305 (1998).

[Chandrasekar 81] S. Chandrasekar. *Hyrodynamic and hydromagnetic instability.* (Dover Publications, New York, United States of America, 1981).

[Clausen 92] T.M. Clausen, P.K. Vinson, J.R. Minter, H.T. Davis, Y. Talmon and W.G. Miller. Viscoelastic micellar solutions: microscopy and rheology. *J. Phys. Chem.* **96**, 474 (1992).

[Combescot 86] R. Combescot, T. Dombre, V. Hakim and Y. Pomeau. Shape selection of Saffman–Taylor fingers. *Phys. Rev. Lett.* **56**, 2036 (1986).

[Corvera–Poiré 98] E. Corvera–Porié and M. Ben–Amar. Finger behavior of a shear–thinning fluid in a Hele–Shaw cell. *Phys. Rev. Lett.* **81**, 2048 (1998).

[Corvera–Poiré 04] E. Corvera–Porié and J.A. del Río. Viscoelastic fingering with a pulsed pressure signal. *J. Phys.: Cond. Matt.* **16**, S2055 (2004).

[Couder 86] Y. Couder, N. Gérard and M. Rabaud. Narrow fingers in the Saffman-Taylor instability. *Phys. Rev. A* **34**, 5175 (1986).

[Couder 00] Y. Couder, in *Perspectives in Fluid Dynamics*, edited by G. K. Batchelor, H. K. Moffat, and M. G. Worster (Cambridge University Press, Cambridge, Great Britain, 2000).

[de Gennes 79] P.G. de Gennes. Reptation of a polymer chain in the presence of fixed obstacles. *J. Phys. Chem.* **55**, 572 (1979).

[Darcy 1856] H. Darcy. *Les fontaines publiques de la ville de Dijon.* Paris (1856).

[de Gennes 04] P.G. de Gennes, F. Brochard-Wyart and D. Quéré. *Capillarity and Wetting Phenomena* (Springer, New York, United States of America, 2004).

[Decker 99] E.L. Decker, J. Ignés-Mullol, A. Baratt and J.V. Maher. Effect of lattice defects on Hele-Shaw flow over an etched lattice. *Phys. Rev. E* **60**, 1767 (1999).

[del Río 98] J.A. del Río, M. López de Haro, and S. Whitaker. Enhancement in the dynamic response of a viscoelastic fluid flowing in a tube. *Phys. Rev. E* **58**, 6323 (1998), **64**, 039901(E) (2001).

[Dorsey 87] A.T. Dorsey and O. Martin. Saffman–Taylor fingers with anisotropic surface tension. *Phys. Rev. A* **35**, 3989 (1987).

[Dougherty 87] A. Dougherty, P.D. Kaplan and J. P. Gollub. Development of side branching in dendritic crystal growth. *Phys. Rev. Lett.* **58**, 1652 (1987).

[Drazin 02] P.G. Drazin. *Introduction to hydrodinamic instability.* (Cambridge Univerisity Press, Cambridge, Great Britain, 2002).

[Eckmann 91] D.M. Eckmann and J.B. Grotberg. Experiments on transition to turbulence in oscillatory pipe flow. *J. Fluid Mech.* **222**, 329 (1991).

[Fermigier 92] M. Fermigier, L. Limat, J.E. Wesfreid, P. Boudinet and C. Quilliet. 2-dimensional patterns in Rayleigh-Taylor instability of a thin-layer. *J. Fluid Mech.* **236**, 349 (1992).

[Fernandez 02] J. Fernandez, P. Kuroswki, P. Petitjeans and E. Meiburg. Density-driven unstable flows of miscible fluids in a Hele-Shaw cell. *J. Fluid Mech.* **451**, 239 (2002).

[Fischer 97] P. Fischer and H. Rehage. Rheological master curves of viscoelastic surfactant solutions by varying the solvent viscosity and temperature. *Langmuir* **13**, 7012 (1997).

[Folch 01] R. Folch, T. Tóth-Katona, Á. Buka, J. Casademunt and A. Hernández–Machado. Periodic forcing in viscous fingering of a nematic liquid crystal. *Phys. Rev. E* **64**, 056225 (2001).

[Gelbart 96] W.M. Gelbart and A. Ben–Shaul. The "new" science of "complex fluids". *J. Phys. Chem.* **100**, 13169 (1996).

[Gland 03] N. Gland and D. Pisarenko. Pressure oscillations on the Saffman-Taylor instability. *Pure Appl. Geophys.* **160**, 977 (2003).

[Gondret 97] P. Gondret and M. Rabaud. Shear instability of two-fluid parallel flow in a Hele-Shaw cell. *Phys. Fluids* **9**, 3267 (1997).

[Groisman 97] A. Groisman and V. Steinberg. Solitary vortex pairs in viscoelastic Couette flow. *Phys. Rev. Lett.* **78**, 1460 (1997).

[Groisman 98] A. Groisman and V. Steinberg. Elastic *vs.* inertial instability in a polymer solution flow. *Europhys. Lett.* **43**, 165 (1998).

[Groisman 00] A. Groisman and V. Steinberg. Elastic turbulence in a polymer solution flow. *Nature* **405**, 53 (2000).

[Groisman 04] A. Groisman and V. Steinberg. Elastic turbulence in curvilinear flows of polymer solutions. *New J. Phys.* **6**, 1 (2004).

[Guyon 94] E. Guyon, J.P. Hulin and L. Petit. *Hydrodynamique physique*(Inter Editions/ Editions du CNRS, Paris, France, 1994).

[Hele–Shaw 1898] H.S.J. Hele Shaw. The flow of water. *Nature* **58**, 34 (1898).

[Hino 76] M. Hino, M. Sawamoto and S. Takasu. Experiments on transition to turbulence in an oscillatory pipe flow. *J. Fluid Mech.* **75**, 193 (1976).

[Kopf–Sill 87] A.R. Kopf–Sill and G.M. Homsy. Narrow fingers in a Hele–Shaw cell. *Phys. Fluids* **30**, 2607 (1987).

[Kopf–Sill 88] A.R. Kopf–Sill and G.M. Homsy. Nonlinear unstable viscous fingers in Hele–Shaw flows. I. Experiments. *Phys. Fluids* **31**, 242 (1988).

[Kopf–Sill 88-b] A.R. Kopf–Sill and G.M. Homsy. Bubble motion in a Hele-Shaw cell. *Phys. Fluids* **31**, 18 (1988).

[Lajeunesse 00] E. Lajeunesse, Y. Couder. On the tip-splitting instability of viscous fingers. *J. Fluid Mech.* **419**, 125 (2000).

[Lambert 04] A.A. Lambert, G. Ibáñez, S. Cuevas and J.A. del Río. Optimal behavior of viscoelastic flow at resonant frequencies. *Phys. Rev. E* **70**, 056302 (2004).

[Larson 99] R. Larson. *The Structure and Rheology of Complex Fluids.* (Oxford University Press, New York, United States of America, 1999).

[Ledesma-Aguilar 05] R. Ledesma–Aguilar, M. Quevedo–Reyes, E. Corvera Poiré and A. Hernández–Machado. Lateral instability in normal viscous fingers. *Phys. Rev. E* **71**, 016312 (2005).

[Lerouge 00] S. Lerouge, J.P. Decruppe and J.F. Berret. Correlations between rheological and optical properties of a micellar solution under shear banding flow. *Langmuir* **16**, 6464 (2000).

[Li 86] G. Li, D. Kessler and L. Sander. Side branching of the Saffman–Taylor finger. *Phys. Rev. A* **34**, 3535 (1986).

[Lindner 00] A. Lindner, D. Bonn and J. Meunier. Viscous fingering in complex fluids. *J. Phys. Cond. Matt.* **12**, A477 (2000).

[Lindner 00b] A. Lindner, D. Bonn and J. Meunier. Viscous fingering in a shear–thinning fluid. *Phys. Fluids.* **12**, 256 (2000).

[Lindner 00c] A. Lindner. *L'instabilité de Saffman–Taylor dans les fluides complexes: relation entre les propietés rhéologiques et la formation de motifs.* PhD Thesis, Université Paris IV (2000).

[López de Haro 96] M. López de Haro, J.A. del Río and S. Whitaker. Flow of Maxwell fluids in porous media. *Transp. Porous Media* **25**, 167 (1996).

[McCloud 95] K.V. McCloud and J.V. Maher. Experimental perturbations to Saffman-Taylor flow. *Phys. Reports* **260**, 139 (1995).

[McLean 81] J.W. McLean and P.J. Saffman. The effect of surface tension on the shape of fingers in a Hele-Shaw cell. *J. Fluid Mech.* **102**, 455 (1981).

[Méndez-Sánchez 03a] A.F. Méndez–Sánchez, M.R. López–González, V.H. Rolón–Garrido, J. Pérez–González and L. de Vargas. Instabilities of micellar systems under homogeneous and non-homogeneous flow conditions. *Rheol. Acta.* **42**, 56 (2003).

[Méndez-Sánchez-03b] A.F. Méndez–Sánchez, J. Pérez–González, L. de Vargas, J.R. Castrejón-Pita, A.A. Castrejón-Pita and G. Huelsz. Particle image velocimetry of the unstable capillary flow of a micellar solution. *J. Rheol.* **47**, 1455 (2003).

[Meulenbroek 04] B. Meulenbroek, C. Storm, A.N. Morozov and W. van Saarloos. Weakly nonlinear subcritical instability of visco-elastic Poiseuille flow. *J. Non-Newtonian fluid Mech.* **116**, 235 (2004).

[Moore 02] M.G. Moore, A. Juel, J.M. Burguess, W.D. McCormick and H.L. Swinney. Fluctuations in viscous fingering. *Phys. Rev. E* **65**, 030601 (2002).

[Morozov 05] A.N. Morozov and W. van Saarloos. Subcritical finite-amplitude solutions for plane Couette flow of viscoelastic fluids. *Phys. Rev. Lett.* **95**, 024501 (2005).

[Mu 01] J.H. Mu and G.Z. Li. The formation of wormlike micelles in anionic surfactant aqueous solutions in the presence of bivalent counterion. *Chem. Phys. Lett.* **345**, 100 (2001).

[Pakdel 96] P. Pakdel and G.H. McKinley. Elastic instability and curved streamlines. *Phys. Rev. Lett.* **77**, 2459 (1996).

[Park 85] C.W. Park and G.M. Homsy. The instability of long fingers in Hele–Shaw flows. *Phys. Fluids* **28**, 1583 (1985).

[Pelcé 88] P. Pelcé. *Dynamics of curved fronts.* (Academic Press, San Diego, United States of America, 1988).

[Pieters86] R. Pieters and J. S. Langer. Noise-driven sidebranching in the boundary-layer model of dendritic solidification. *Phys. Rev. Lett.* **56**, 1948 (1986).

[Pitts 80] E. Pitts. Penetration of fluid into a Hele-Shaw cell: the Saffman–Taylor experiment. *J. Fluid Mech.* **97**, 53 (1980).

[Quevedo–Reyes 06] M. Quevedo–Reyes, A. Hernández–Machado and E. Corvera–Poiré. Phase field approach to spatial perturbations in normal Saffman–Taylor fingers. *Phys. Rev. E* **73**, 066308 (2006).

[Rabaud 88] M. Rabaud, Y. Couder and N. Gerard. Dynamics and stability of anomalous Saffman–Taylor fingers. *Phys. Rev. A* **37**, 935 (1988).

[Rehage 88] H. Rehage and H. Hoffman. Rheological properties of viscoelastic surfactant systems. *J. Phys. Chem.* **92**, 4712 (1988).

[Saffman 58] P.G. Saffman and G. Taylor. The penetration of a fluid into a porous medium or Hele-Shaw cell containing a more viscous liquid. *Proc. R. Soc. London A* **245** , 312,(1958).

[Salmon 03] J.B. Salmon, A. Colin and S. Manneville. Velocity profiles in shear–banding wormlike micelles. *Phys. Rev. Lett.* **90**, 228303 (2003).

[Séréro 98] Y. Séréro, R. Aznar, G. Porte, J.F. Berret, D. Calvet, A. Collet and M. Viguier. Associating polymers: from "flowers" to transient networks. *Phys. Rev. Lett.* **81**, 5584 (1998).

[Soriano 03] J. Soriano. *Roughness experiments of viscous fluid interfaces in disordered Hele–Shaw cells.* PhD Thesis, Universitat de Barcelona (2003).

[Soriano 05] J. Soriano, A. Mercier, R. Planet, A. Hernández–Machado, M.A. Rodríguez and J. Ortín. Anomalous roughening of viscous fluid fronts in spontaneous imbibition. *Phys. Rev. Lett.* **95**, 104501 (2005).

[Tabeling 86] P. Tabeling and A. Libchaber. Film draining and the Saffman–Taylor problem. *Phys. Rev. A* **33**, 794 (2005).

[Tabeling 87] P. Tabeling, G. Zocchi and A. Libchaber. An experimental study of the Saffman–Taylor instability. *J. Fluid Mech.* **177**, 67 (1987).

[Tanveer 87] P. Tanveer and P.G. Saffman. Stability of bubbles in a Hele-Shaw cell. *Phys. Fluids* **30**, 2624 (1987).

[Thomé 89] H. Thomé, M. Rabaud, V. Hakim and Y. Couder. The Saffman–Taylor instability: From the linear to the circular geometry *Phys. Fluids A* **1**, 224 (1989).

[Tsiklauri 01] D. Tsiklauri and I. Beresnev. Enhancement in the dynamic response of a viscoelastic fluid flowing through a longitudinally vibrating tube. *Phys. Rev. E* **63**, 046304 (2001).

[Vlad 99] D.H. Vlad, J. Ignés–Mullol and J.V. Maher. Velocity–jump instabilities in Hele–Shaw flow of associating polymer solutions. *Phys. Rev. E.* **60**, 4423 (1999).

[Weissenberg 47] K. Weissenberg. A continum theory of rheological phenomena. *Nature* **159**, 310 (1947).

[Zhao 92] H. Zhao, J. Casademunt, C. Yeung and J.V. Maher. Perturbing Hele-Shaw flow with a small gap gradient. *Phys. Rev. A* **45**, 2455 (1992).

[Zocchi 87] G. Zocchi, B.E. Shaw, A. Libchaber and L.P. Kadanoff. Finger narrowing under local perturbations in the Saffman-Taylor problem. *Phys. Rev. A* **36**, 1894 (1987).

Author's publications

- M. Torralba, J.R. Castrejón–Pita, A.A. Castrejón–Pita, G. Huelsz, J.A. del Río and J. Ortín, *Measurements of the bulk and interfacial velocity profiles in oscillating Newtonian and Maxwellian fluids*, Phys. Rev. E **72**, 016308 (2005).

- M. Torralba, J. Ortín, A. Hernández–Machado and E. Corvera–Poiré, *Fluctuations in Saffman-Taylor fingers with quenched disorder*, Phys. Rev. E **73**, 046302 (2006).

- M. Torralba, J. Ortín, A. Hernández–Machado and E. Corvera–Poiré, *Experiments of periodic forcing of Saffman Taylor fingers*, submitted to Phys. Rev. E.

- M. Torralba, A.A. Castrejón–Pita, G. Hernández, G. Huelsz, J.A. del Río and J. Ortín, *Instabilities in the oscillatory flow of a complex fluid*, submitted to Phys. Rev. E.

Part III

Appendices

Appendix A

Rheological characterization of a cetylpiridinium chloride sodium salicylate aqueous solution: linear and non linear response

A.1 Introduction

The rheological behavior of a cetylpyridinium chloride (CPyCl) sodium salicylate (NaSal) aqueous solution [100/60] mM has been studied by several groups [Rehage 88; Méndez-Sánchez 03a; Berret 93]. This surfactant solution behaves as a Maxwell fluid at small shear rates, but exhibits shear thinning at higher shear rates. It is also known that the fluid can present shear banding [Salmon 03; Berret 97; Méndez-Sánchez-03b].

Other micellar solutions [Fischer 97; Ali 97; Clausen 92] also behave as a Maxwell fluid at small shear rates. This is also true for some polymer solutions [Cáthebras 98; Séréro 98]. The advantage of CPyCl/NaSal is that is very easy to prepare, and also that the elasticity of the material is very high for a relatively low viscosity.

A.1.1 Maxwell Model

When a stress[1] τ is applied to a purely elastic material, the response of the material (a strain γ) is in-phase with the applied stress. The shear modulus G_0 characterizes

[1] Although the stress and the strain are tensors we will consider flows for which the stress and the strain can be treated as scalars.

the elasticity of the material:

$$\tau = G_0 \gamma. \tag{A.1}$$

On the contrary, when a stress τ is a applied to a purely viscous material the response is in quadrature with the applied stress. The stress creates a flow (with a characteristic shear rate $\dot{\gamma}$). The viscosity η_0 characterizes the dissipative properties of the material:

$$\tau = \eta_0 \dot{\gamma}. \tag{A.2}$$

But there are many materials that do not correspond to any of these two limits. When a stress is applied to the material the response is out of phase to the stress but neither the viscous nor the elastic effects can be discarded. These are the so called viscoelastic materials: they exhibit both a dissipative and an elastic behavior (silly putty, blood, plastics).

The simplest mechanical model that includes elasticity and viscosity of a material is called Maxwell model (see Sec. 3.2.2). Maxwell relaxation time t_m is related with the shear modulus and the viscosity by:

$$t_m = \frac{\eta_0}{G_0}. \tag{A.3}$$

There are several methods to measure the rheological properties of a fluid. Periodic experiments are the most usual choice to measure the linear viscoelasticity of fluids. In periodic measurements, a sinusoidal stress is applied to the fluid. The response of the sample will be out of phase with the stress. From the phase angle between stress and strain, we can calculate the storage modulus G' (which describes the elastic properties of the fluid) and the loss modulus G'' (which corresponds to the viscous or dissipative properties of the fluid). For a Maxwell fluid, in particular, the response of the material to harmonic oscillations of angular frequency w is described by [Rehage 88]:

$$G'(w) = \frac{G_0 w^2 t_m^2}{1 + w^2 t_m^2}, \tag{A.4}$$

$$G''(w) = \frac{G_0 w t_m}{1 + w^2 t_m^2}. \tag{A.5}$$

From Eqs. (A.4) and (A.5), a relation between the storage modulus and the loss modulus can be derived:

$$\left(G'(w) - \frac{G_0}{2}\right)^2 + \left(G''(w)\right)^2 = \left(\frac{G_0}{2}\right)^2, \tag{A.6}$$

which is the equation of a circle of radius $G_0/2$ centered at $(0, G_0/2)$. The plot of G'' as a function of G' is called the Cole-Cole plot and is useful to determine if the

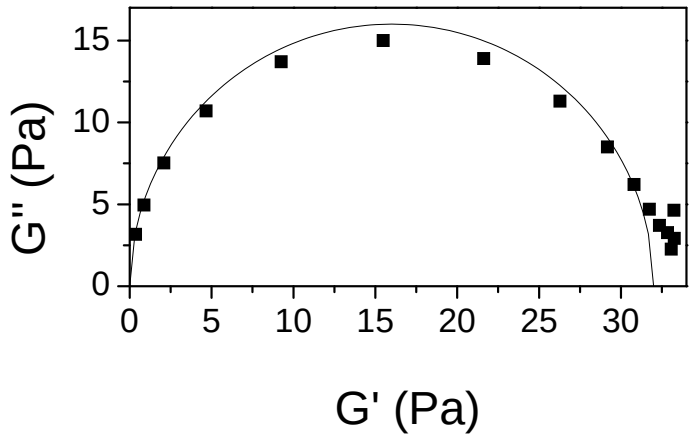

Figure A.1: Cole-Cole plot for the solution of CPyCl/NaSal 100/60 mM at $T = 25°$C. The range of frequencies explored is $\omega = (0, 90)$ rad/s.

fluid we are studying behaves as a Maxwell fluid. The Cole-Cole plot for our fluid (see figure A.1) shows that our CPyCl/NaSal solution behaves as a Mawxell fluid in the whole range of frequencies we are reporting.

A.2 Experimental

The surfactant solution is prepared by solving commercial cetylpyridinium chloride and sodium salycylate (both from Sigma) in distilled water. The solution is let in a dark chamber at a constant temperature of 20°C for three or four days. Measurements of the fluid properties at different days show that aging effects are not important in the first two weeks after the fluid has been prepared.

The CPyCl/NaSal solution has been used as a "standard" Maxwell fluid for several reasons. First, it is very easy to prepare. The properties of the solution remain constant for long times. The viscosity of the material is much smaller than the viscosity of other viscoelastic solutions [Fischer 97; Ali 97; Clausen 92; Mu 01]. The relaxation time is also very long compared with other solutions. Lastly, in the linear regime the solution is very well described by a Maxwell linear model, as can be verified with the Cole-Cole plot (Fig. A.1).

The rheological measurements are carried out by means of a Haake RheoStress 1 rheometer with the cone and plate geometry (60 mm in diameter and 1°). This geometry is one of the most frequently used to determine the rheological characterization of viscoelastic flows. It has the advantage of presenting a simple flow with uniform shear rate and uniform shear stress throughout the gap. The use of this

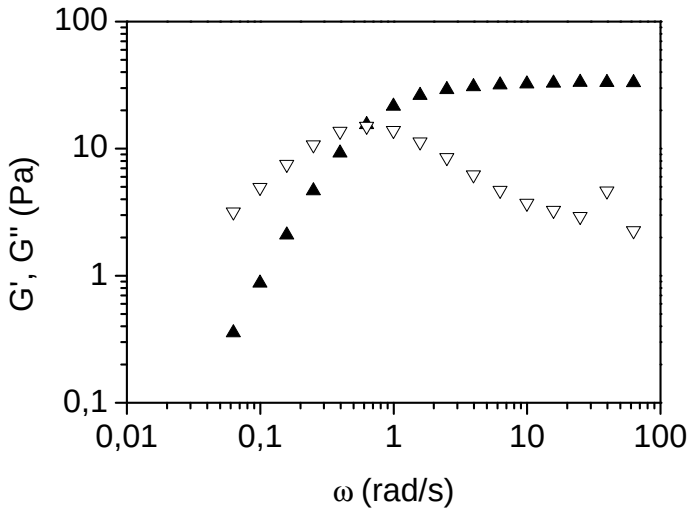

Figure A.2: (▲) Storage modulus G', and (△) loss modulus G'', as a function of the angular frequency ω, for the solution of CPyCl/NaSal 100/60 mM at $T = 25°$C.

experimental arrangement is limited to moderate shear rates, since for high shear rates a stationary flow cannot be developed and the viscoelastic sample may present fractures or degradation.

We undertook both oscillatory and rotating tests. For the rotating tests we performed:

(i) Controlled stress experiments. We increased the stress from 1 Pa to 25 Pa with logarithmic ramps of durations from 600 s to 2400 s.

(ii) Controlled rate experiments. We increased the rate from 0.2 s^{-1} to 20 s^{-1} with a logarithmic ramp of 2400 s.

A.3 Results

A.3.1 Linear regime

The linear viscoelastic behavior is consistent with the behavior reported by other authors [Rehage 88; Méndez-Sánchez 03a]. The measured shear modulus is $G_0 = 32$ Pa and the longest relaxation time (or Maxwell time) is $t_m = 1.8$ s (Fig. A.2). From rotating experiments, zero shear viscosity is $\eta_0 = 60$ Pa·s, in fair agreement with the relation $\eta_0 \simeq G_0 t_m$.

A.3.2 Nonlinear regime

The results summarized in the previous section are true if the fluid is subjected to small shear rates (linear regime). At increasing stresses and shear rates, our surfactant solution presents a different behavior [Méndez-Sánchez 03a]. At high shear rates the fluid is shear thinning. This means that the viscosity of the fluid decreases as shear rate increases.

For this reason, we also performed rotating experiments in order to determine the range where the fluid behaves as a pure Maxwell fluid. The results for the controlled stress measurements are shown in Figs. A.3 and A.4. From these figures we can observe that the viscosity of the fluid is constant for shear rates up to 0.1 s^{-1}. As the shear rate increases above this value, the fluid presents strong shear thinning. As usual in shear thinning fluids, the behavior of η in the shear thinning region can be fitted with a relation of the kind $\eta = K\dot{\gamma}^{-n}$. We obtain:

$$\eta \simeq 20\dot{\gamma}^{-1}. \tag{A.7}$$

It is interesting to mention that the curves for the different ramps (Fig. A.4) and for the controlled shear rate tests (Fig. A.5) are equivalent at the linear and early nonlinear stages. For shear rates up to 0.6 s^{-1} ($\tau \simeq 23$ Pa) the results are the same for all the ramps. At shear stresses higher than 23 Pa the resulting $\dot{\gamma}$ depends on the ramp. We compare these results to the one obtained for the controlled shear rate tests.

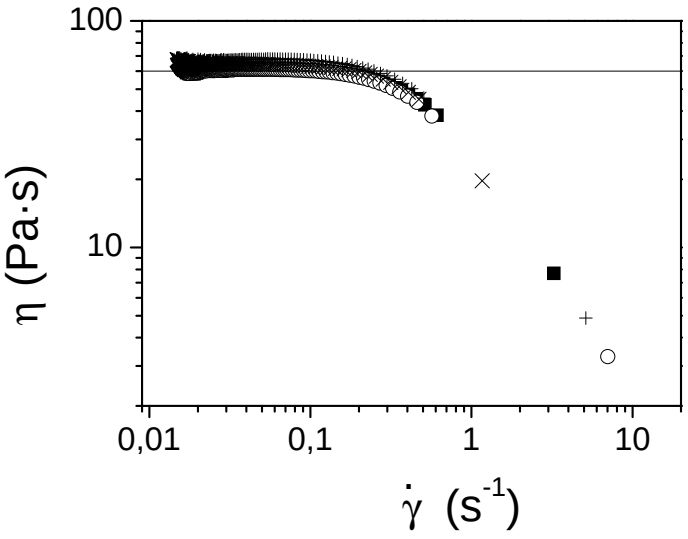

Figure A.3: Shear viscosity of a sample of CPyCl/NaSal 100/60 mM as a function of the applied shear rate for controlled stress ramps at $T = 25°$C. Different symbols correspond to ramps of duration: (■) $t = 600$ s, (○) $t = 1200$ s, (+) $t = 1800$ s, (×) $t = 2400$ s.

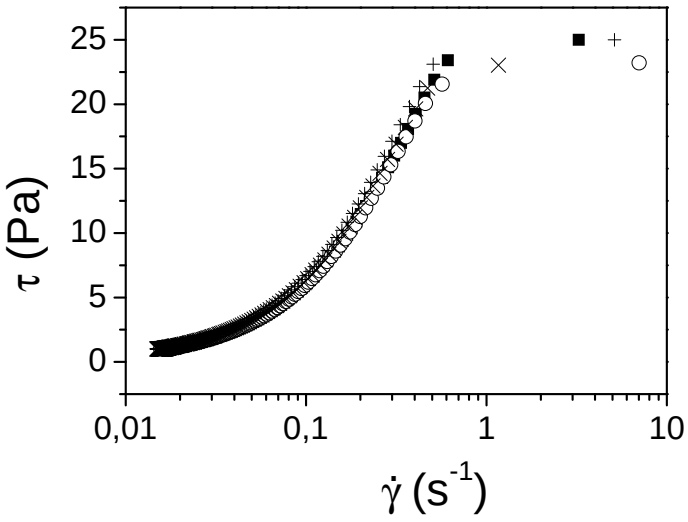

Figure A.4: Shear stress *vs.* shear strain rate, in controlled stress measurements of a sample of CPyCl/NaSal 100/60 mM at $T = 25°$C. The symbols correspond to ramps of duration: (■) $t = 600$ s, (○) $t = 1200$ s, (+) $t = 1800$ s, (×) $t = 2400$ s.

At small $\dot{\gamma}$ the relation is linear; for $\dot{\gamma}$ of approximately 0.6 s^{-1} the stress reaches a maximum of 20 Pa, and then decreases to a plateau value around 18 Pa. We conclude that the results for the linear regime are equivalent for all the tests performed and the results in the nonlinear regime depend strongly on the test performed.

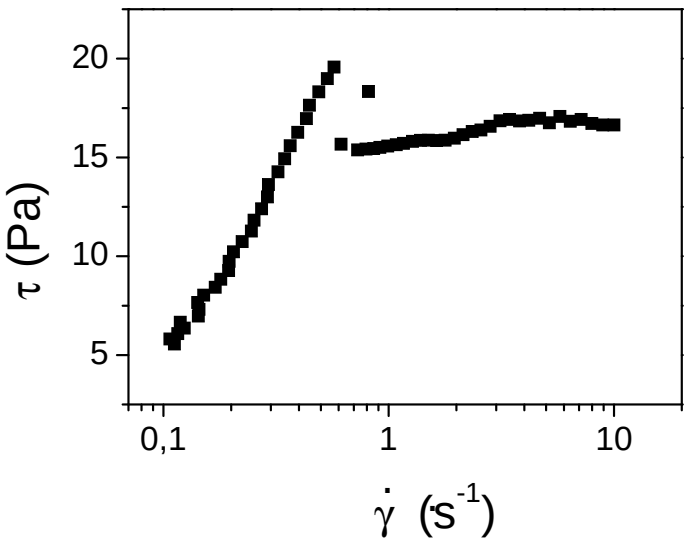

Figure A.5: Shear stres *vs.* shear strain rate in controlled shear rate measurements of CPyCl/NaSal 100/60 mM at $T = 25°$C.

Appendix B

Setup for the characterization of the onset of instability for an oscillating flow in a tube

The experimental device used in the study of the flow of a complex fluid in a tube was initially designed for the study of the dynamic permeability of a Maxwell fluid in a tube [Castrejón-Pita 03b]. As commented in Ch. 10, we performed slight modifications in this experimental setup in order to study the destabilization of the flow. We observed that the flow became unstable at moderately high driving amplitudes, but we could not determine the minimum driving amplitude for which the flow became unstable because of the design of the experimental device.

Thus, important questions such as the minimum value of the control parameter $\mathrm{Wi}/(t_m\nu)$ needed for the destabilization of the flow, or the presence of hysteresis in the system, could not be answered. In order to fully characterize the onset of instability for an oscillating viscoelastic flow in a tube, we have designed a new experimental device (Fig. B.1).

This new experimental device is essentially the same than the one described in Ch. 10. The main difference between both systems is the mechanism to produce the vertical oscillations of the piston (Fig. B.2). In the original device, the displacement is originated by a crankshaft mechanism and the amplitude of the driving is determined by the eccentric wheel. Thus, each new amplitude of driving requires a new eccentric wheel.

In the new experimental device a long bar is used to produce the vertical displacement (Fig. B.2). One of the ends of the bar is firmly subjected, and the other end rests on top of an eccentric wheel connected to a motor of variable frequency.

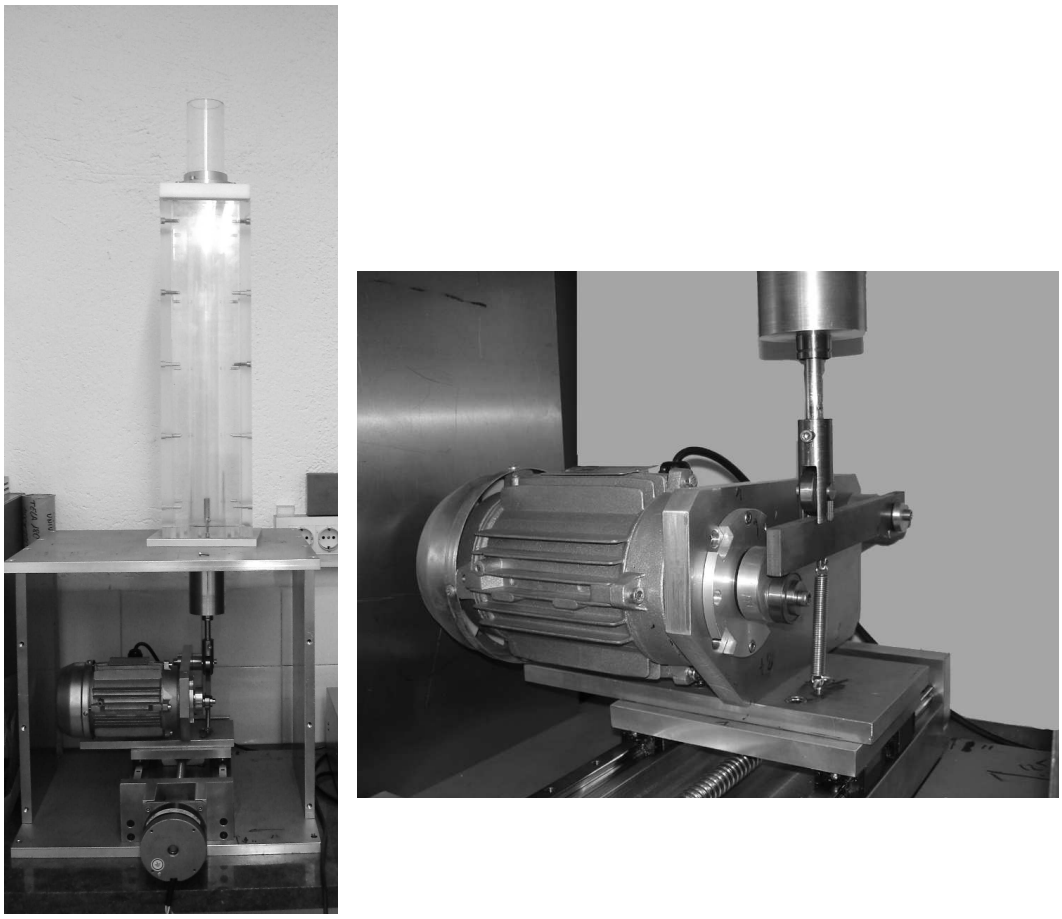

Figure B.1: Image of the experimental device designed for the characterization of the onset of the instability for an oscillating viscoelastic flow in a tube.

The system is carefully aligned to provide the horizontal position of the bar at the neutral position of the eccentric wheel. The amplitude (z_0) of the vertical oscillations provided by the driving wheel in the new device is different at different distances (d) from the fixed end of the bar. By simple trigonometric relations this amplitude can be related with the maximum amplitude of the oscillation (Z_{max}):

$$z_0 = Z_{max}\frac{d}{L}. \tag{B.1}$$

The piston is connected to the horizontal bar by a rod which has a ball–bearing at the end. This allows the relative displacement of the motor–eccentric wheel–bar system from the tube, even at high oscillation frequencies. As a consequence, the setup is able to work at continuously varying vertical oscillation amplitudes. We control the relative displacement by mounting the motor–eccentric wheel–bar system on a mobile platform. The platform is controlled by means of a stepper motor and thus, different displacement velocities can be fixed.

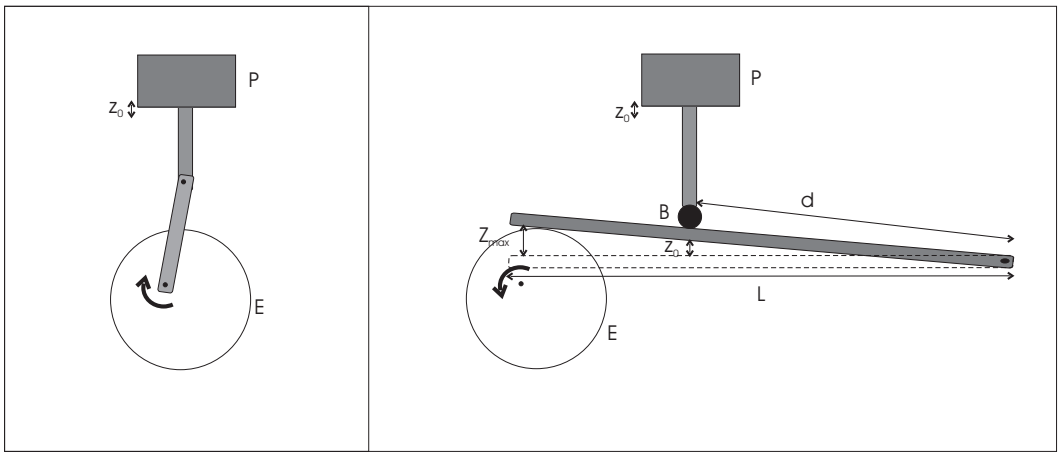

Figure B.2: Left: Scheme of the crankshaft mechanism of the original experimental setup. **Right:** Scheme of the new experimental device. (P) Piston, (E) eccentric wheel, (B) ball–bearing, (z_0) driving amplitude, (Z_{max}) maximum driving amplitude, (L) bar length, (d) distance to the fixed end of the bar.

Summarizing, the new experimental setup produces driving amplitudes in the range 0 to 5 mm. The driving amplitude can be ramped in a continuous way at different time rates. The onset of instability can be determined as a function of driving frequency and amplitude. Given that the instability may present hysteresis, our experimental setup its ready for its characterization, as it allows both increasing and decreasing driving amplitudes.